PHILOSOPHICAL MAGAZINE

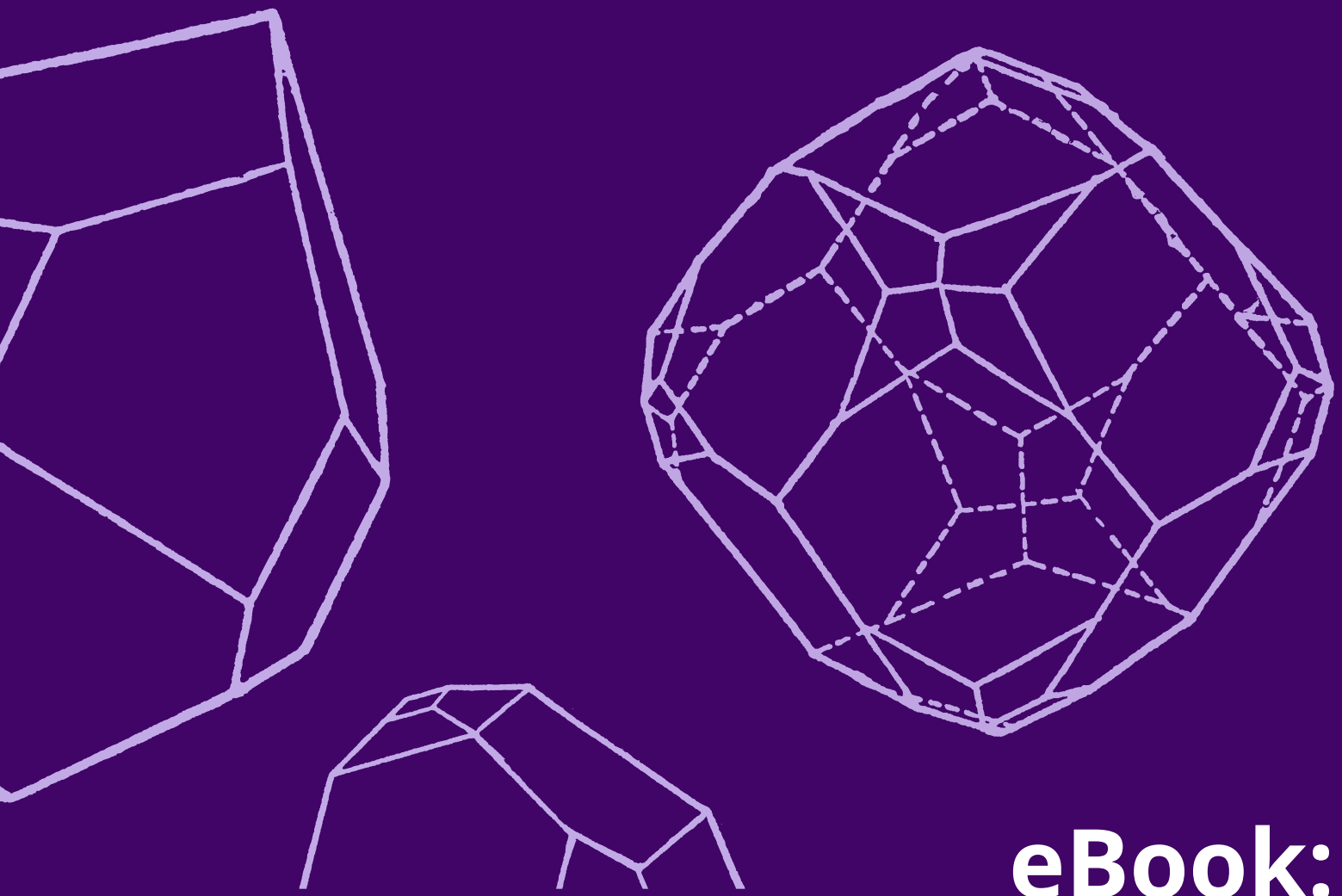

eBook: Methods and models in crystallography

Taylor & Francis
by informa

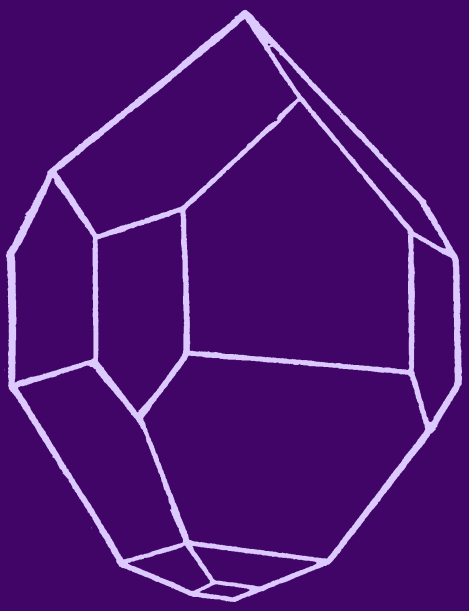

eBook

Methods and models in crystallography

Contents:

- Crystal plasticity modelling of time-dependent strain accumulation of stainless steel at room temperature
- Electron density mapping analysis using XRD and tailoring of the optical and magnetic properties in Ni doped SnO2
- Study of the boundary migration of recrystallized grains under inhomogeneous deformation field by crystal plasticity – phase field simulation
- Investigating particle-particle interaction during the initial crystal growth: insights from phase field model approach
- On the mechanism of shear-coupled grain boundary migration in FCC crystals

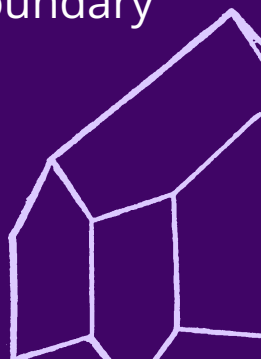

Taylor & Francis
by informa

Philosophical Magazine

ISSN: 1478-6435 (Print) 1478-6443 (Online) Journal homepage: www.tandfonline.com/journals/tphm20

Crystal plasticity modelling of time-dependent strain accumulation of stainless steel at room temperature

Sadik Sefa Acar & Tuncay Yalçinkaya

To cite this article: Sadik Sefa Acar & Tuncay Yalçinkaya (2026) Crystal plasticity modelling of time-dependent strain accumulation of stainless steel at room temperature, Philosophical Magazine, 106:1, 1-21, DOI: 10.1080/14786435.2025.2536601

To link to this article: https://doi.org/10.1080/14786435.2025.2536601

Published online: 31 Jul 2025.

PHILOSOPHICAL MAGAZINE
2026, VOL. 106, NO. 1, 1–21
https://doi.org/10.1080/14786435.2025.2536601

Taylor & Francis
Taylor & Francis Group

Crystal plasticity modelling of time-dependent strain accumulation of stainless steel at room temperature

Sadik Sefa Acar and Tuncay Yalçinkaya

Department of Aerospace Engineering, Middle East Technical University, Ankara, Turkiye

ABSTRACT

The mechanical integrity of structural materials under cyclic loading conditions is vital for various industries. 304L stainless steel parts often undergo cyclic loading and stress hold periods resulting in time-dependent strain accumulation. In this work, effects of mean stress and stress hold periods on strain ratcheting are examined using crystal plasticity modelling. A representative volume element (RVE) consisting of 200 grains is subjected to various loadings in the DAMASK framework, employing an isotropic-kinematic hardening model. Simulations are performed under three types of stress-controlled loading conditions: low-cycle fatigue (LCF), creep-fatigue interaction (CFI) with cyclic stress holds, and fatigue after long hold (FLH). Cyclic loadings ranged from symmetric to non-symmetric loading with high mean stress. The model is validated through comparison with experimental ratcheting data. For LCF loading, high mean stresses lead to pronounced ratcheting, while symmetric loading results in significant hardening in the early stages of cyclic loading. Cyclic hold periods in CFI loading amplify strain accumulation by enabling sustained slip activity during hold phases. Long hold periods of FLH loading induce significant strain accumulation which continues to increase with extended hold duration but saturates during following cyclic loading. Quantitative and qualitative comparisons with relevant experimental data demonstrate that the simulations effectively capture ratcheting trends under various loading conditions.

ARTICLE HISTORY
Received 26 January 2025
Accepted 3 July 2025

KEYWORDS
Strain ratcheting; RVE; crystal plasticity; microstructure; mean stress; isotropic-kinematic hardening model

1. Introduction

Structural materials used in many industrial fields are subjected to cyclic loadings. Throughout their service life, the cyclic loading leads to the accumulation of the plastic strain. The increase in plastic strain under stress-controlled cyclic loading is termed as strain ratcheting, and it is an important area of research due to the significance it possesses for the design and reliability of engineering applications [1]. In addition to the cyclic loading, materials in critical applications such as nuclear power plants and gas-turbine engines usually undergo hold periods occuring at the peak of each cycle. For a nuclear power plant, the structure can be assumed to be under hold condition

CONTACT Tuncay Yalçinkaya yalcinka@metu.edu.tr Department of Aerospace Engineering, Middle East Technical University, Ankara 06800, Turkiye

between periodic shutdown-startups for scheduled maintenance. For a typical gas turbine engine working at a constant operating revolution per minute (RPM), most of the stationary and rotating parts are subjected to constant stress loading during operation. Hold periods account for a great portion of the service life for examples like these. Therefore, the mechanical behaviour of materials used in these areas has been studied in the literature for stress-hold condition along with cyclic loading [2,3]. On the other hand, hold periods cover comparable or less time than loading and unloading phases for some other applications where either loading and unloading occur slowly or the material experiences a very short hold time at each cycle. Assessing the strain ratcheting of materials is especially important for the evaluation of the fatigue life of components. The contributions of cyclic loading and hold periods to the accumulated plastic strain have to be studied in detail. The influence of stress hold periods depends on many parameters including the material type and microstructure, operating temperature, multiaxiality and proportionality of loading, and the hold duration [4–6]. An accurate prediction of stress hold effects is needed to avoid failures earlier than expected [7]. For instance, a single operational cycle of a structural part of an aero gas turbine engine may be considered as a major cycle combined with numerous minor cycles. An alternative approach is to treat minor cycles as a long uninterrupted hold duration. During the design phase of an engine, these approaches may result in different plastic deformation and fatigue life predictions. Consequently, understanding the enhancive and reductive physical mechanisms for strain ratcheting is inevitably necessary.

Stainless steels are widely used in various industries including construction, automotive, nuclear energy, and aerospace. Ratcheting of stainless steels under cyclic loading without hold times has been studied extensively [8–12]. Depending on the engineering application, structural parts made of stainless steel alloys may undergo cyclic loading with hold time. It was experimentally shown that, even at low temperatures, adding stress hold periods to cyclic loading modifies the fatigue life of the stainless steel [13–15]. Even though there have been many attempts in the literature, previous work could not build consensus on the effect of hold times during cyclic loading on the fatigue life of stainless steels [4,14,16,17]. A case-specific evaluation has to be made for hold effects considering the material state and loading conditions. In contrast to inconsistent findings on fatigue life, previous work had similar conclusions about the influence of hold periods on the strain ratcheting of stainless steels. It was experimentally demonstrated that adding hold periods to stress-controlled loading leads to an increase in the strain ratcheting of 304 stainless steel at room temperature, while hold periods result in a decrease in effective stress amplitude during strain-controlled loading due to the relaxation phenomena [18].

Many experimental studies have been conducted on the ratcheting of stainless steel. Chen et al. [14] investigated the ratcheting behaviour of 316L Stainless Steel at room temperature under mixed stress- and strain-controlled cyclic loading where stress and strain hold periods followed each other. They concluded that the cyclic hardening of the material is mainly due to the kinematic hardening instead of the isotropic hardening, and that the strain holds suppress the creep strain in subsequent stress hold. Taleb and Caillateud [19] have shown for 304L that long stress hold at peak stress leads to considerable creep strain even at room temperature, yet it significantly reduces the strain ratcheting in following cyclic loading. Taleb and Keller [20] experimented with various

loading conditions including stress cycling with different amplitudes about low mean stresses (0 and 25 MPa) after a long stress hold. They found that the strain obtained during the creep phase is preserved during cycling loading and no ratcheting was recorded until cyclic softening emerges at a higher number of cycles. For some of these loading conditions, the axial strain was shown to be slightly decreasing during cycling loading until the softening started. Similar behaviour was also reported by Yoshida [21] for cyclic loading about zero mean stress without prior creep loading, the strain achieved during the first cycle was shown to decrease in subsequent cycles until it saturates due to plastic shakedown. Ratcheting was achieved when the mean stress was increased to 25 MPa. Yet, the same study also found that the cyclic decrease in strain under zero mean stress disappears when 60 s of stress holding was added to each cycle. Higher axial ratchetings were recorded for cyclic loadings with hold periods. Also, the accumulated strain obtained by loading with high mean stress and low strain amplitude is shown to be very similar to the creep strain obtained by static creep loading under peak stress. Kang et al. [18] also investigated the time-dependent ratcheting of SS304. They demonstrated that adding 5 s of hold time to cyclic stress loading at room temperature results in a substantial increase in strain ratcheting while increasing the hold time to 10 s leads to a minor modification in ratcheting behaviour. However, when the experiments were conducted at 700 °C with lower stress amplitude and mean stress, the increase in hold time had a much more pronounced effect compared to room temperature experiments. There are many studies in the literature on the strain ratcheting behaviour of steels under cyclic stress loading with various stress amplitudes and mean stresses, yet the number of studies investigating the strain ratcheting under cyclic loading with cyclic stress holds is very limited. Similarly, room temperature creep of stainless steels was studied in the literature [21–24], but there are not many studies that have investigated the material behaviour under cyclic loading with or without hold periods after creep loading.

Experimental investigations into time-dependent ratcheting behaviour have inherent challenges. While indispensable for validating theoretical findings, these studies are generally costly and require extensive laboratory equipment. Additionally, their primary focus is the macroscopic material responses, offering limited information regarding the microstructural mechanisms underlying observed deformation behaviours. Numerical simulations have emerged as valuable tools to complement experimental studies, providing a means to predict strain accumulation. The literature contains numerous numerical approaches to modelling strain ratcheting in stainless steels under stress-controlled cyclic loading without hold durations [10,25–34]. There are also numerical studies that investigated the effect of hold durations on the cyclic deformation of stainless steels [14,35–38]. These models often incorporate modifications to isotropic and kinematic hardening rules. However, a significant number of these studies have focussed on macroscopic behaviour, overlooking the contributions of microstructural properties and local material responses to strain accumulation. Overcoming these limitations requires models that not only account for the material behaviour under cyclic and time-dependent loading conditions but also integrate both macroscopic and microstructural perspectives.

Crystal plasticity (CP) can be used to model deformation mechanisms at the grain scale, enabling a more direct representation of microstructural properties and their effects [39–44]. In the literature, CP models are employed to assess the ratcheting

behaviour of stainless steels [45–50] and other metallic alloys [51–56] under various mean stresses and stress amplitudes. In addition to simulations modelling ratcheting under cyclic deformation, there are also other CP studies focussed on time-dependent strain accumulation under stress-controlled cyclic loading with hold durations. Zhang et al. [57] investigated the ratcheting behaviour of a nickel-based single crystal superalloy DD6 under thermomechanical fatigue (TMF) loading, which includes cyclic thermal and symmetric stress loads with hold periods. In their study, a modified slip-based Walker constitutive model, incorporating microstructure evolution and damage effects, is used to simulate the ratcheting strain and hysteresis loops, revealing that the mechanical response is influenced by both stress amplitude and the evolution of microstructural damage, including rafting. Agius et al. [58] developed a CP model by modifying an isotropic CP model to include Armstrong-Frederick (AF) type back-stress evolution and temperature-dependent recovery term in the hardening equation for 316H stainless steel. They predicted stress relaxation and creep under single and multiple dwell loading conditions, including load-control and strain-control dwells. Zhou et al. [59] modified an AF back-stress model to include a third term covering steady-state deformation to better describe time-dependent strain accumulation during hold periods. In that work, P92 steel polycrystal is subjected to hybrid creep-fatigue interaction (HCFI) loading composed of a strain-controlled loading followed by a stress-controlled hold duration. Bulut et al. [6] simulated dwell fatigue fracture in HCP titanium alloys under both static and cyclic loading with hold durations by coupling a rate-dependent CP model with a phase field fracture framework. It was demonstrated that the damage accumulation occurs primarily during the hold periods, and crack initiation and propagation are influenced by grain misorientation under cyclic loading with hold durations.

This study aims to advance the understanding of strain ratcheting behaviour in stainless steels by investigating the combined effects of mean stress and stress hold durations on macroscopic and microstructural responses using a rate-dependent crystal plasticity model. Model parameters are identified using experimental data and subsequently validated against additional independent experiments. Beyond macroscopic strain evolution, the model enables detailed microstructural analysis at the grain scale, capturing internal stress redistribution, plastic slip accumulation, and critical resolved shear stress (CRSS) evolution under different loading histories. Although much experimental work has focussed on measuring macroscopic strain responses under cyclic loading, there has been limited investigation into the variation of stress and accumulation of strain at the micro-scale, especially under varied mean stresses and stress holds. In contrast to existing CP studies which predominantly address either creep or cyclic loading separately, the current work integrates both aspects within a unified simulation framework. This enables a more comprehensive understanding of how time-dependent loading influences deformation at both macro and micro scales, particularly for service conditions where creep and cyclic effects coexist.

2. Theory

In this study, the combined isotropic-kinematic hardening model is employed for crystal plasticity simulations.The model is a rate-dependent local viscoplastic crystal plasticity

formulation allowing to capture the time-dependent response of the material at grain-scale. The model was developed by Wollmershauser et al. [60] and later implemented in the DAMASK with finite strain framework [61]. In the employed framework, the deformation gradient **F** maps points from the reference configuration to the current configuration. **F** is multiplicatively decomposed into elastic deformation gradient $\mathbf{F}_e$ and plastic deformation gradient $\mathbf{F}_p$.

$$\mathbf{F} = \mathbf{F}_e \cdot \mathbf{F}_p \tag{1}$$

$\mathbf{F}_p$ is an inelastic deformation gradient mapping the points in the reference configuration to the intermediate configuration without distorting the crystal lattice. $\mathbf{F}_e$ maps points from the intermediate configuration to the current configuration, stretching and rotating the crystal lattice. The second Piola–Kirchhoff stress tensor denoted by **S** for a given **F** is obtained by substituting the $\mathbf{F}_e$ in the following relation

$$\mathbf{S} = \mathbb{C} : \frac{1}{2}\left(\mathbf{F}_e^T\mathbf{F}_e - \mathbf{I}\right) \tag{2}$$

where $\mathbb{C}$ and **I** refer to elastic stiffness tensor and identity tensor, respectively. To calculate the stress state utilising the above relation, firstly, the $\mathbf{F}_p$ has to be determined and substituted in $\mathbf{F}_e = \mathbf{F} \cdot \mathbf{F}_p^{-1}$. Plastic deformation gradient $\mathbf{F}_p$ can be obtained by integrating the below relation numerically in an implicit manner

$$\dot{\mathrm{F}}_p = \mathrm{L}_p \cdot \mathrm{F}_p \tag{3}$$

$\mathbf{L}_p$ denotes the plastic velocity gradient and it is formulated as

$$\mathbf{L}_p = \sum_{\alpha=1}^{k} \dot{\gamma}^{\alpha}(\mathbf{m}^{\alpha} \otimes \mathbf{n}^{\alpha}) \tag{4}$$

In the above formulation the slip rate ($\dot{\gamma}^{\alpha}$) contributions of all slip systems are summed to obtain plastic velocity gradient tensor. Slip direction and slip plane normal of slip system α are denoted by $\mathbf{m}^{\alpha}$ and $\mathbf{n}^{\alpha}$, respectively. The total number of slip systems is denoted by k and it equals to 12 since all slip systems of FCC material are included in the model. Slip rate is calculated according to the below rule

$$\dot{\gamma}^{\alpha} = \dot{\gamma}_0^{\alpha}\left(\frac{\tau^{\alpha} - \tau_{\mathrm{bs}}^{\alpha}}{\tau_{\mathrm{for}}^{\alpha}}\right)^{n} \tag{5}$$

where $\dot{\gamma}_0^{\alpha}$ denotes the reference slip rate. The effective shear stress is obtained by subtracting the back-stress ($\tau_{\mathrm{bs}}^{\alpha}$) from the resolved shear stress (τ^{α}). $\tau_{\mathrm{for}}^{\alpha}$ denote the forest stress. It is assumed that all slip systems of face-centered cubic (FCC) material can be active at any time depending on current effective stress and forest stress on that system. Even though the plastic velocity gradient at any time is obtained by the summation of slip rates on all slip systems, the flow rule may or may not produce slip rate on a given slip system during that time increment. The rate sensitivity exponent is represented by n. Back-stress and

forest stress evolve according to

$$\dot{\tau}^{\alpha}_{\text{for}} = \sum_{\beta} q^{\alpha\beta} h^{\alpha\alpha}_{\text{for}} \dot{\gamma}^{\beta} \tag{6}$$

$$\dot{\tau}^{\alpha}_{\text{bs}} = \sum_{\beta} q^{\alpha\beta} h^{\alpha\alpha}_{\text{bs}} \dot{\gamma}^{\beta} \tag{7}$$

The ratio of latent hardening to self-hardening ($q^{\alpha\beta}$) equals 1 for all slip system interactions. Self-hardening moduli for isotropic hardening ($h^{\alpha\alpha}_{\text{for}}$) and kinematic hardening ($h^{\alpha\alpha}_{\text{bs}}$) are given as

$$h^{\alpha\alpha}_{\text{for}} = h_{\text{s,for}} + \left(h_{0,\text{for}} - h_{\text{s,for}} + \Gamma \left(\frac{h_{0,\text{for}} h_{\text{s,for}}}{\tau_{\text{s,for}}} \right) \right) e^{-\Gamma \frac{h_{0,\text{for}}}{\tau_{\text{s,for}}}} \tag{8}$$

$$h^{\alpha\alpha}_{\text{bs}} = h_{\text{s,bs}} + \left(h_{0,\text{bs}} - h_{\text{s,bs}} + (\gamma^{\alpha} - \gamma^{\alpha}_{0}) \left(\frac{h_{0,\text{bs}} h_{\text{s,bs}}}{\tau_{\text{s,bs}} + \chi^{\alpha}_{0}} \right) \right) e^{-(\gamma^{\alpha} - \gamma^{\alpha}_{0}) \frac{h_{0,\text{bs}}}{\tau_{\text{s,bs}} + \chi^{\alpha}_{0}}} \tag{9}$$

In the isotropic hardening formulation, $\tau_{\text{s,for}}$ refers to the saturation forest slip resistance. $h_{0,\text{for}}$ and $h_{\text{s,for}}$ denote the initial and saturation forest hardening moduli, respectively. The forest stress is equated to the initial forest slip resistance ($\tau_{0,\text{for}}$) in the first time increment. Γ denotes the total accumulated slip on all slip systems. The kinematic hardening modulus is obtained by replacing the forest stress terms in the isotropic hardening equation with back-stress terms. $h_{0,\text{bs}}$ and $h_{\text{s,bs}}$ refer to initial and saturation back-stress saturation hardening moduli, respectively. $\tau_{\text{s,bs}}$ denotes the saturation back-stress resistance. There are two main differences between isotropic and kinematic hardening formulations. The first difference is that isotropic hardening accounts for the total accumulated slip (Γ) over all slip systems, while for kinematic hardening, Γ is replaced by the difference between the amount of slip on a slip system (γ^{α}) and the strain memory term in that slip system (γ^{α}_{0}). The strain memory term is equal to the accumulated slip in a slip system reached before the direction of the glide is reversed. The other difference is that when replacing the saturation forest slip resistance, the saturation back-stress slip resistance is increased by the amount of stress memory term χ^{α}_{0}. Stress memory term is the maximum back-stress experienced before the direction of glide is reversed.

3. Numerical model

The DAMASK framework with spectral solver is utilised throughout this work [61,62]. Analyses are conducted on a polycrystal RVE containing 200 grains. The polycrystal model is presented in Figure 1. Crystal orientation distribution is set to be completely random. The model is meshed with a grid-type regular mesh consisting of 8000 points. A convergence study on grid resolution and grain number is also conducted. Crystal plasticity model parameters are obtained by fitting the simulation results to experiments for hysteresis loops under strain-controlled cyclic loading. For ratcheting simulations, a combination of stress and strain boundary conditions is utilised by manipulating the average deformation gradient (**F**) and First Piola–Kirchhoff stress (**P**). The deformation gradients in normal directions and the shear term F_{12} are set to be unconstrained. The rest of the shear terms in the deformation gradient tensor are set to be 0

Figure 1. The polycrystal representative volume element containing 200 grains.

throughout the simulation. For the First Piola-Kirchoff stress, the axial normal stress term is controlled such that the uniaxial stress cycling with a triangular waveform is imposed. The rest of the normal stress terms in addition to the P_{12} are set to be 0 throughout the simulation. For the analyses with mean stress, the axial normal stress is increased to the mean stress value in the first cycle, and stress cycling occurs about that mean value in the following cycles. For all simulations in the results part, the stress rate is kept at 26 MPa/s during both the loading and unloading phases.

Cubic elastic constants for 304L stainless steel are taken from Wang et al. [63] and used as $C_{11} = 262.2$ GPa, $C_{12} = 112$ GPa, and $C_{44} = 74.6$ GPa. The strain rate sensitivity exponent n is set to 20 in this study. Charles et al. [64] demonstrated that a rate sensitivity exponent of 21 accurately captures the low strain rate behaviour of 304L stainless steel at room temperature. Additionally, several other studies have reported values of n in the range of 15–20 for various stainless steels under similar conditions [65–69]. A series of simulations are conducted to determine model parameters. Many CP parameter combinations are analysed, and the parameter set producing the closest homogenised stress response to the experimental response is utilised in the rest of the work. Cyclic uniaxial strain-controlled experiments conducted by Mehani and Roy [70] are used to calibrate the model parameters. The hysteresis loops at the 2nd and 10th cycles for cyclic loadings with 0.6% and 0.8% strain amplitudes are used for parameter identification. During simulations, the strain rate is kept constant at 10^{-3} s^{-1}. The comparisons of experiments and simulations conducted with fitted model parameters are illustrated in Figure 2. Fitted model parameters are shown in Table 1.

To minimise statistical scatter and reduce RVE-induced error, it is essential to employ a sufficiently large number of grains in simulations. An adequately sized RVE is expected to produce consistent macroscopic mechanical responses across different random

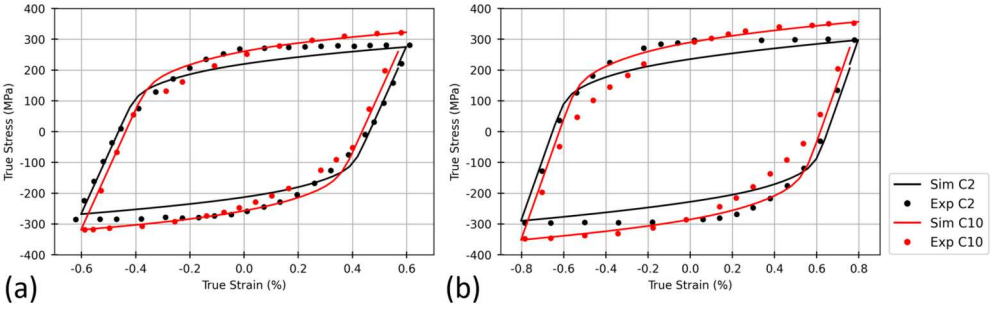

Figure 2. Macroscopic true stress and strain results for 2nd and 10th cycles under uniaxial strain-controlled symmetric cyclic loading with (a) 0.6% and (b) 0.8% strain amplitudes obtained by simulations compared to experiments taken from Mehani and Roy [70].

Table 1. Combined Isotropic-Kinematic Hardening Model parameters calibrated for 304L stainless steel.

$\tau_{0,\text{for}}$	$\tau_{s,\text{for}}$	$h_{0,\text{for}}$	$h_{s,\text{for}}$	$\tau_{s,\text{bs}}$	$h_{0,\text{bs}}$	$h_{s,\text{bs}}$	$\dot{\gamma}_0$	n
80 MPa	15 MPa	130 MPa	35 MPa	23 MPa	5000 MPa	1300 MPa	0.001	20

orientation sets. When the grain count is insufficient, local heterogeneities such as crystal orientations can influence not only the local behaviour but also the overall macroscopic response, thereby compromising the representativeness of the RVE for an FCC polycrystal. To address this, the number of grains in the RVE is progressively increased. Figure 3 presents the results of uniaxial tension simulations for three random orientation sets with RVEs containing 10, 60, and 120 grains, where notable scatter is observed in the macroscopic response due to statistical scattering. Upon increasing the number of grains to 200 and trials with two grid resolutions, the flow curves for the RVE with 200 grains and 8000 points demonstrate near-identical behaviour as shown in Figure 4. Based on this convergence, an RVE with 200 grains and 8000 points is adopted for the rest of the study.

Ratcheting simulations are categorised into three groups. The first group is called LCF (low cycle fatigue) loading consisting of cyclic stress-controlled loading without hold periods. The second group is called CFI (creep-fatigue interaction) loading which is the cyclic stress-controlled loading with hold periods applied at the peak (maximum)

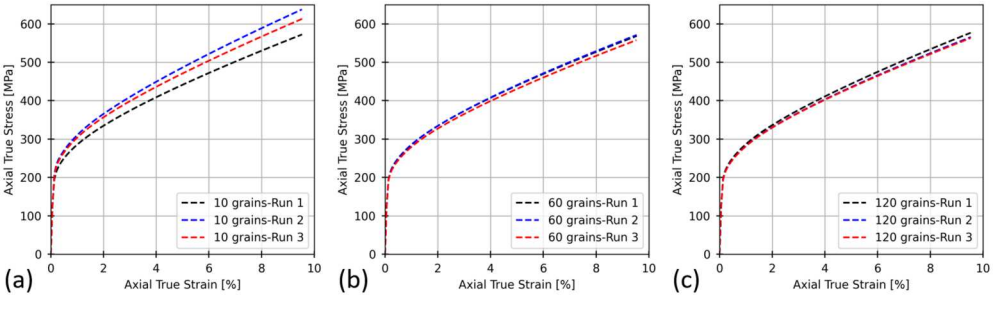

Figure 3. True stress and strain results for uniaxial tension simulations employing three random orientation sets for RVEs having (a) 10, (b) 60, and (c) 120 grains.

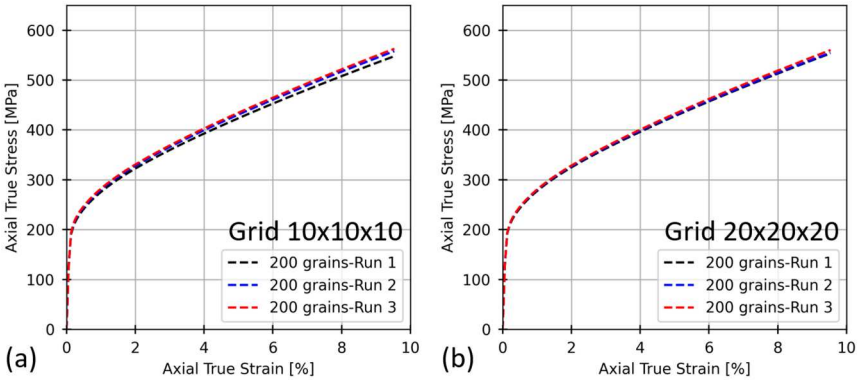

Figure 4. True stress and strain results for uniaxial tension simulations employing three random orientation sets for RVEs having 200 grains and grid resolutions of (a) 10 and (b) 20.

stress of each cycle. The stress ratio, R, is defined as the ratio of the minimum stress to the maximum stress within a cycle. It is used throughout this study to distinguish between analyses conducted under different mean stresses. LCF and CFI loadings are applied with five different mean stresses ranging from 0 MPa ($R = -1$) to 225 MPa ($R = 0.8$). The last group of simulations is called FLH (fatigue after long hold) loadings for which a long stress hold is followed by a cyclic stress-controlled loading. FLH loadings combine three long hold periods; 10 min, 60 min, and 100 min, and two mean stresses; 0 MPa ($R = -1$) and 125 MPa ($R = 0$). The loading conditions are illustrated in Figure 5 and details regarding the loading parameters are presented in Table 2.

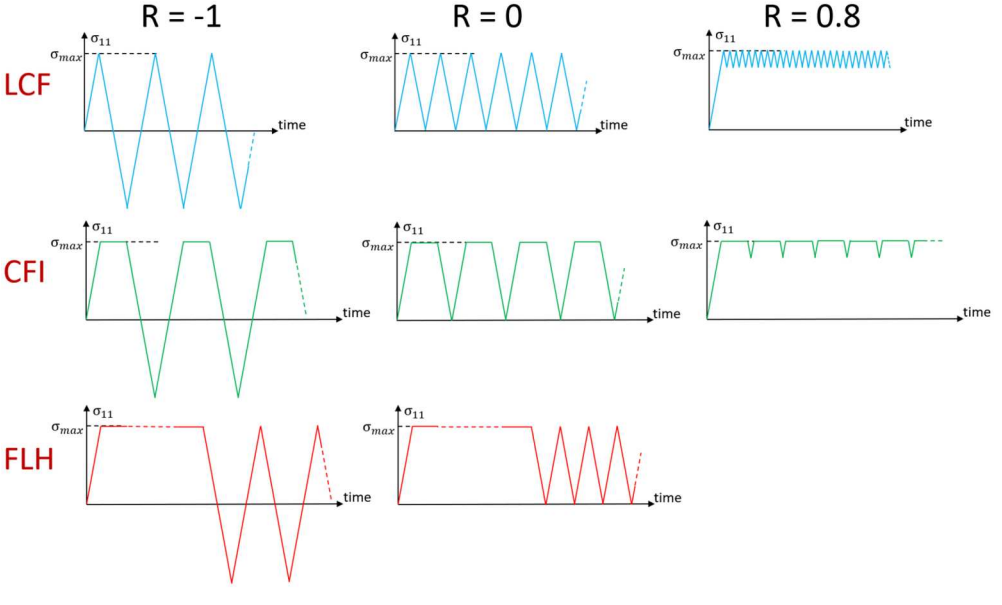

Figure 5. Illustrations of stress histories for LCF (low-cycle fatigue), CFI (creep-fatigue interaction), and FLH (fatigue after long hold) loading under different mean stresses corresponding to symmetric ($R = -1$) and non-symmetric ($R = 0$ and $R = 0.8$) loadings.

Table 2. Loading parameters for LCF, CFI, and FLH loadings where $t_{\text{initial hold}}$ represents the duration of long hold applied at the first cycle and $t_{\text{cyclic hold}}$ denotes duration of hold periods applied at each cycle.

	$\sigma_{\max}$ [MPa]	σ_{mean} [MPa]	$\sigma_{\min}$ [MPa]	σ_{amp} [MPa]	R	$t_{\text{initial hold}}$	$t_{\text{cyclic hold}}$
LCF1	250	0	−250	250	−1	–	–
LCF2	250	25	−200	225	−0.8	–	–
LCF3	250	75	−100	175	−0.4	–	–
LCF4	250	125	0	125	0	–	–
LCF5	250	225	200	25	0.8	–	–
CFI1	250	0	−250	250	−1	–	60 s
CFI2	250	25	−200	225	−0.8	–	60 s
CFI3	250	75	−100	175	−0.4	–	60 s
CFI4	250	125	0	125	0	–	60 s
CFI5	250	225	200	25	0.8	–	60 s
Creep	250	–	–	–	–	100 min	–
FLH1	250	0	−250	250	−1	10 min	–
FLH2	250	0	−250	250	−1	60 min	–
FLH3	250	0	−250	250	−1	100 min	–
FLH4	250	125	0	125	0	10 min	–
FLH5	250	125	0	125	0	60 min	–
FLH6	250	125	0	125	0	100 min	–

4. Results and discussion

The strain ratcheting behaviour of 304L stainless steel under uniaxial stress-controlled cyclic loading is investigated using the numerical model. Calibrated model parameters are employed in two ratcheting simulations, each run for 100 cycles with a stress amplitude of 150 MPa. The first simulation used a mean stress of 100 MPa while the second simulation utilised 125 MPa mean stress. Axial strain peaks are presented in Figure 6 and compared with experimental data from Taleb and Cailletaud [19]. For 100 MPa mean stress case, results are significantly close to the experimental data throughout the entire loading history. Results for the simulation employing 125 MPa mean stress shows a slight deviation at high number of cycles. Nevertheless, the numerical model

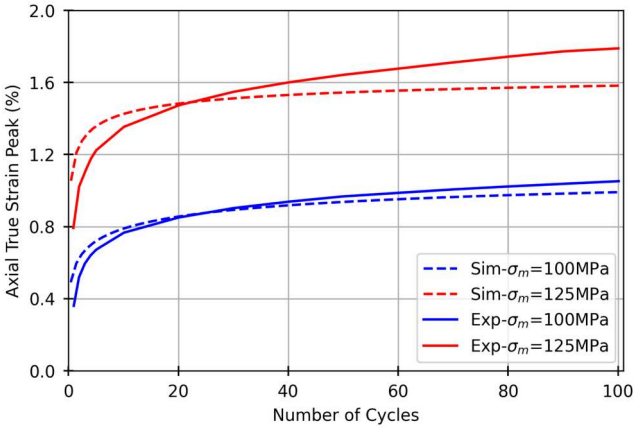

Figure 6. Simulation results for axial true strain peaks of cyclic response under uniaxial stress-controlled loadings with 150 MPa stress amplitude, and mean stresses (σ_m) of 100 MPa and 125 MPa, compared to experimental ratcheting data taken from Taleb and Cailletaud [19].

accurately reproduces the experimentally observed ratcheting behaviour for both simulations, including the rapid accumulation of strain during the initial cycles and the slower, steady increase in strain in the subsequent cycles. The ability of model to simulate strain ratcheting behaviour is due to its inclusion of back-stress evolution, which accounts for the directional hardening effects during cyclic loading. By incorporating history terms into the back-stress evolution equation, the model retains information about the state of deformation prior to the last load reversal, enabling it to account for path-dependent material responses. The alignment between simulation and experimental data confirms the capability of model to predict the strain accumulation behaviour.

Further simulations are conducted to investigate the effects of varying mean stress and introducing stress-hold conditions. These simulations demonstrate the sensitivity of strain accumulation to changes in stress cycle asymmetry and time-dependent deformation mechanisms. The maximum stress is fixed at 250 MPa across all simulations, while mean stress is varied by adjusting the minimum stress resulting in different stress amplitudes. Figure 7(a) shows the ratcheting response under low-cycle fatigue (LCF) loading, while Figure 7(b) presents results for creep-fatigue interaction (CFI) loading, where 60 s stress holds are introduced at the peak stress of each cycle. In addition to ratcheting curves, hysteresis loops are extracted for 1st, 5th, 40th, and 100 cycles for FCI and CFI loadings as shown in Figures 8 and 10, respectively. The strain reached in the first cycle is consistent across all mean stress levels due to the identical maximum stress, while subsequent cycles reveal distinct ratcheting trends influenced by mean stress and time-dependent deformation mechanisms.

Under LCF loading, ratcheting strain accumulation increases with mean stress due to the asymmetric stress cycles induced by higher mean stresses as illustrated in Figure 7(a). The absence of compressive plasticity in simulations with high mean stress ($R = 0.8$ and $R = 0$) eliminates the strain hardening effects associated with compressive loading, leading to sustained strain accumulation through cycles. Hysteresis loops obtained for high mean stress simulations are presented in Figure 8(a,b). They show that as the number of cycles increases, the hysteresis loop is translated in the tensile direction while it becomes narrower and gradually reduces to an almost straight line. This is an interesting observation considering the plastic part of the flow curve at the last cycle is nearly unnoticeable, however, the strain accumulation is not saturated even at the last cycle. For intermediate mean stresses ($R = -0.4$ and $R = -0.8$), the presence of

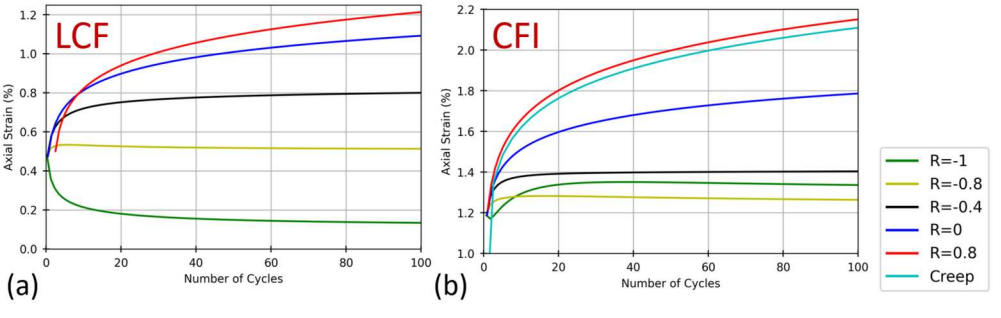

Figure 7. Simulation results for axial true strain peaks of cyclic response under (a) LCF and (b) CFI loadings with various mean stresses.

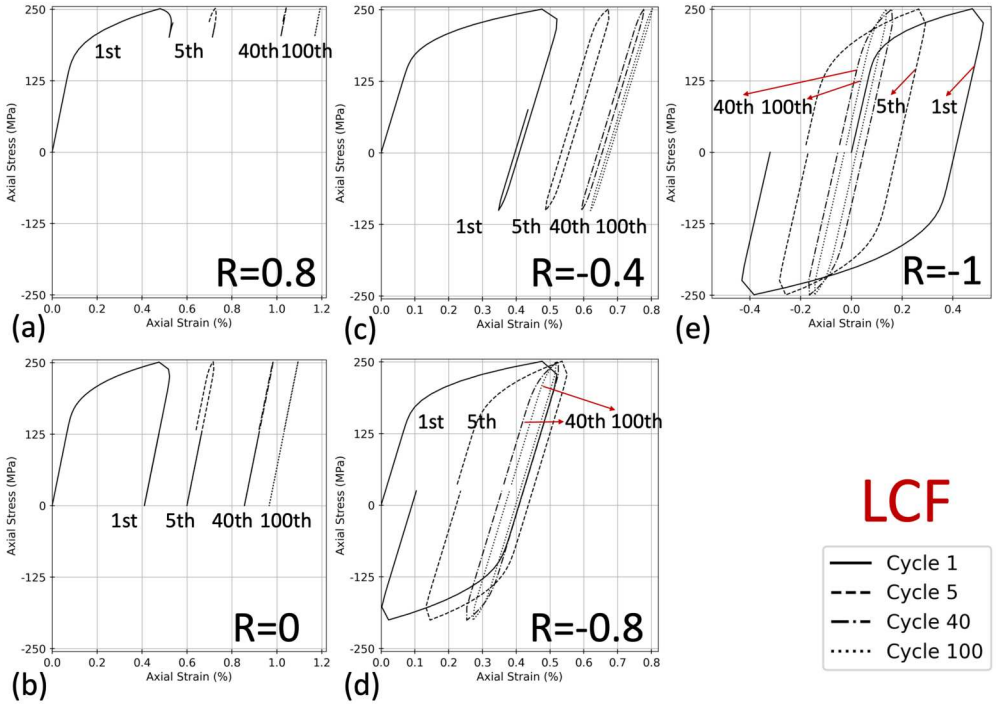

Figure 8. Hysteresis loops for 1st, 5th, 40th, and 100th cycles in LCF simulations under different mean stresses corresponding to stress ratios (a) R = 0.8, (b) R = 0, (c) R = −0.4, (d) R = −0.8, and (e) R = −1.

compressive plastic deformation amplifies strain hardening. This amplification moderates strain accumulation and leads to stabilisation of ratcheting strain after a certain number of cycles. The existence of compressive plastic deformation is also noticeable in Figure 8(c,d). Another observation for the hysteresis loops is that, in contrast to simulations with higher mean stress, the hysteresis loops for the R = −0.8 case are not reduced to an almost straight line with the increasing number of cycles but the loading and unloading phases are still distinguishable even at the last cycle. For symmetric loading (R = −1), the significant compressive plastic deformation occurring in early stages results in increased hardening and reduction in peak axial strain which is also evident in Figure 8(e).

These observations are consistent with the experimental study conducted by Yoshida [21] using 304L stainless steel, where symmetric and near-symmetric LCF loadings exhibit substantial cyclic hardening, reducing strain accumulation in subsequent cycles. Similar to our simulations, experiments with symmetric cyclic loading resulted in the plastic shakedown and no ratcheting strain accumulation.

Figure 9 illustrates the axial strain and stress distributions at the peak of the last cycle under LCF loading. While the peak macroscopic stress level remains consistent at 250 MPa across all LCF simulations, simulations differ in the variation of stress values within RVE. For the highest mean stress case (R = 0.8), the difference between maximum and minimum local stress values is notably higher compared to other cases. This indicates that the higher macroscopic strain observed after cyclic loading (ratcheting

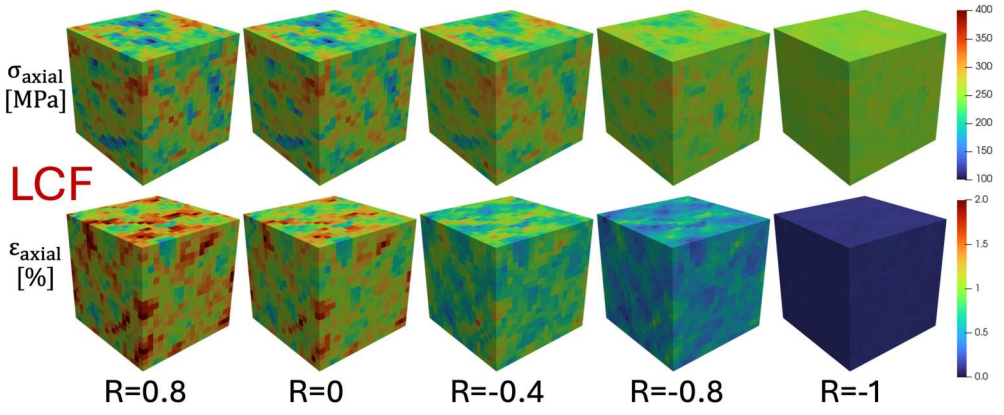

Figure 9. Axial stress and strain contours at the peak of the last cycle of LCF loading for various stress ratios and corresponding mean stresses.

strain) in the high mean stress case likely originates from localised regions with disproportionately higher strain contributions. This relation shows that heterogeneous deformation within the microstructure is due to not only the crystal orientations of grains but also the loading condition. Simulation with lower mean stress exhibits a more uniform stress distribution, resulting in reduced strain accumulation.

For CFI simulations, the introduction of a 60 s stress hold at the peak stress significantly amplifies ratcheting strain compared to LCF loading for all mean stress levels. This amplification arises primarily from the time-dependent viscoplastic deformation enabled by the numerical model, where the flow rule governing crystal slip evolution allows continued slip activity under constant stress during the hold phase. Examining the hysteresis loops for all mean stresses in Figure 10, most of the strain increase occurs during the hold phase. For symmetric loading ($R = -1$), the hold time delays plastic shakedown, enabling time-dependent mechanisms to dominate the response and produce a pronounced difference in ratcheting strain compared to LCF loading. At intermediate mean stresses ($R = -0.4$ and $R = 0$), the contribution of the stress hold varies with the degree of stress asymmetry but remains a significant factor in driving strain accumulation. The greatest quantitative increase in ratcheting strain following the addition of hold time is observed in the highest mean stress case ($R = 0.8$), primarily due to higher strain accumulation in the hold phase The static creep curve in Figure 7(b) uses time as its horizontal axis; creep loading is applied for 100 min, corresponding to the total duration of stress hold periods for 100 cycles in the cyclic simulations. Strain accumulation under static creep closely matches the ratcheting strains observed in CFI loading with high mean stress ($R = 0.8$). This indicates that the strain observed under high mean stress in cyclic loading is largely driven by the time-dependent deformation mechanisms.

The experimental study conducted by Yoshida [21] under CFI loading showed similar mechanical behaviour as the stress holds increased the total strain accumulation. Similar to our simulations, the CFI loading with high mean stress yields a strain accumulation closer to the static creep loading. For symmetric loading, the delay in plastic shakedown caused by hold periods is also observed in experiments.

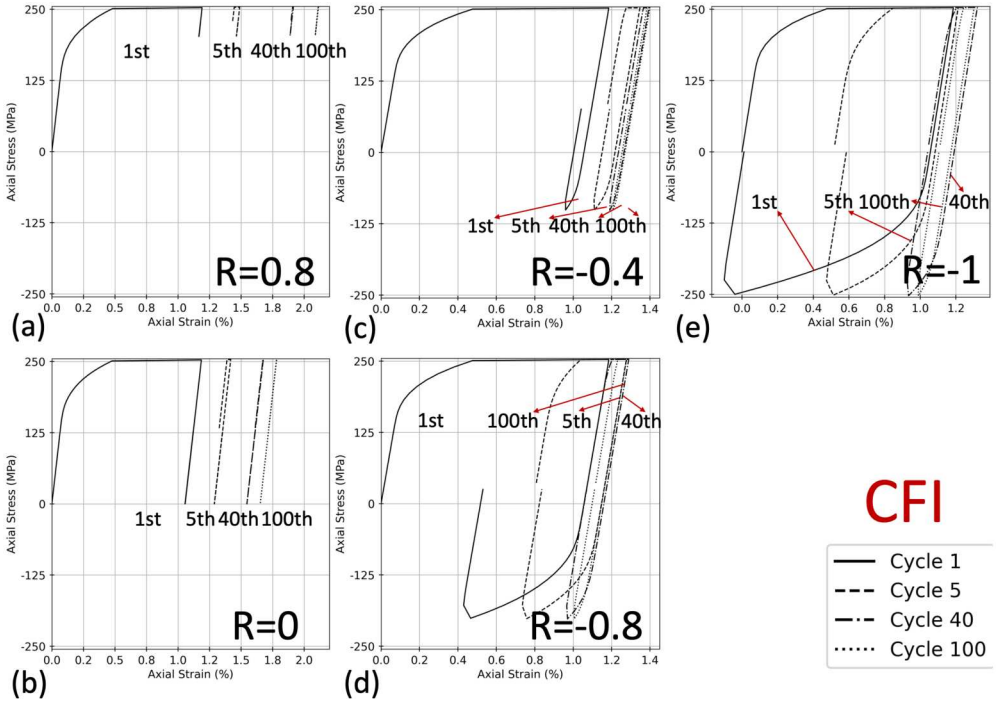

Figure 10. Hysteresis loops for 1st, 5th, 40th, and 100th cycles in CFI simulations under different mean stresses corresponding to stress ratios (a) R = 0.8, (b) R = 0, (c) R = −0.4, (d) R = −0.8, and (e) R = −1.

Axial strain and stress distributions at the peak of the last cycle under CFI loading are presented in Figure 11. Similar to stress contours obtained for LCF loading, the high mean stress case exhibits less uniform stress distribution within the RVE compared to lower mean stress cases. Yet, the difference in the level of uniformity between simulations is much lower for CFI loading compared to LCF loading shown in Figure 9. Particularly, the symmetric loading case (R = −1) under CFI loading showed considerably lower uniformity in stress variation compared to the same case under LCF loading. Parallel to the observations for accumulated strain, this relation is also a consequence of cyclic stress holds which prevent the decrease in axial strain peak after the first cycle and delay the plastic shakedown for the symmetric loading case.

Hysteresis loops obtained for FLH loading are presented in Figure 12. This type of loading condition consists of a long hold period at the peak stress followed by uniaxial cyclic stress-controlled loading without additional cyclic hold periods. FLH simulations included three initial long hold periods (10 min, 60 min, and 100 min), and two mean stress values: 125 MPa (R = 0) and 0 MPa (R = −1). For non-symmetric cyclic loading (R = 0), most of the strain accumulation occurs during the initial long hold period, with subsequent cyclic loading having minimal impact on the hysteresis loop. Compared to LCF loading with R = 0 (Figure 8(b)), the initial long hold period of FLH loading not only results in a higher peak strain than that observed after 100 cycles of LCF loading but also leads to the saturation of cyclic strain accumulation. The saturation in ratcheting after a long hold period is also experimentally shown in

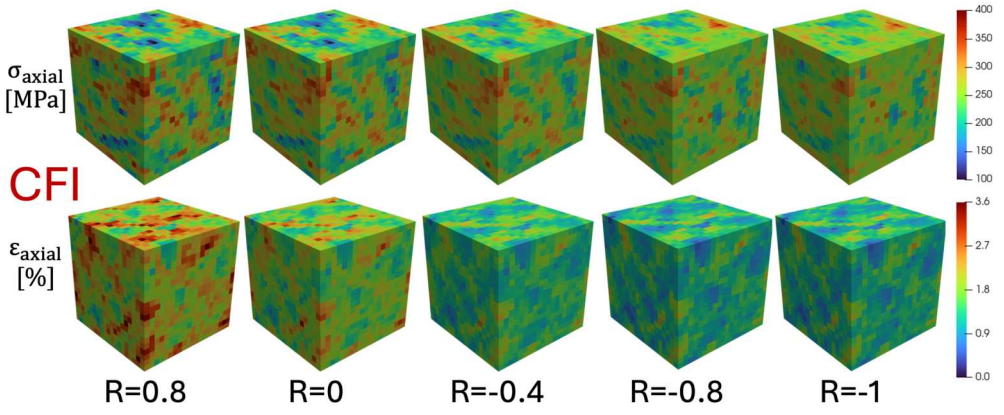

Figure 11. Axial stress and strain contours at the peak of the last cycle of CFI loading for various stress ratios and corresponding mean stresses.

Taleb and Cailletaud [19] for 304L stainless steel under non-symmetric stress cycling following a long hold at room temperature. Interestingly, strain accumulation during hold does not saturate after a 10-minute hold period but continues to increase with longer hold durations. Comparing Figure 12(a), 12(c), and 12(e), the saturation in strain accumulation observed in cyclic loading after an initial long hold does not occur if the

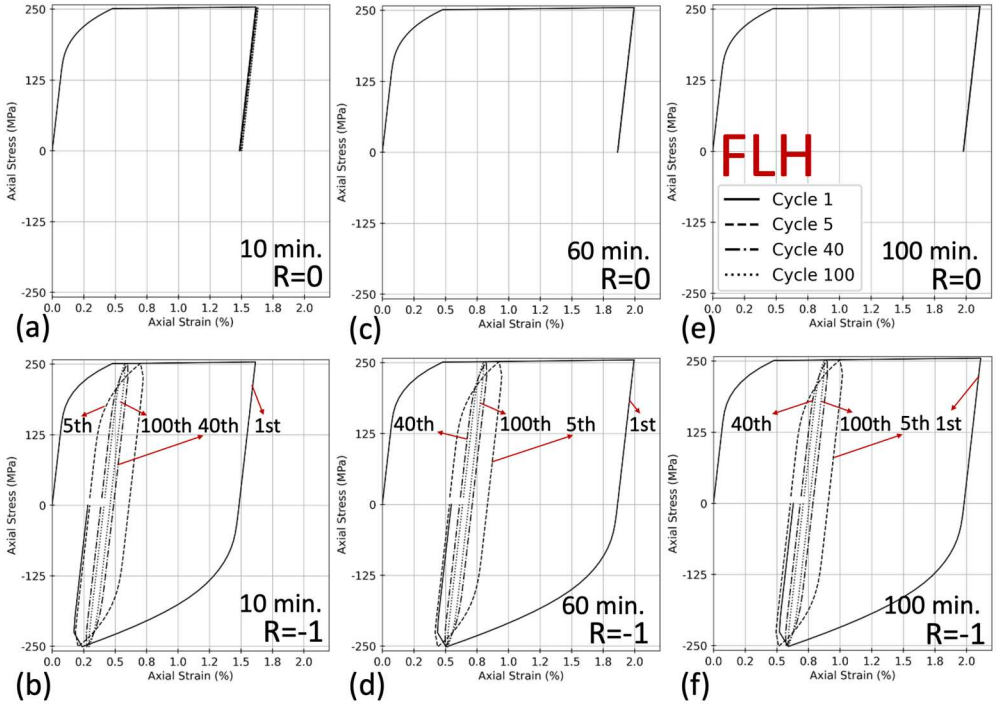

Figure 12. Hysteresis loops for the 1st, 5th, 40th, and 100th cycles in FLH simulations with mean stresses of 0 MPa ($R = -1$) and 125 MPa ($R = 0$), and long hold durations of (a,b) 10, (c,d) 60, and (e,f) 100 min.

long hold itself is further extended instead of transitioning to cyclic loading. This is due to the viscoplastic flow rule, which permits ongoing slip activity under constant stress. As a result, strain accumulation reaches values that exceed those achieved under LCF loading with the same mean stress, where saturation occurs earlier. However, as the long hold duration increases, the rate of strain accumulation decreases. For symmetric loading ($R = -1$), the long hold period does not delay plastic shakedown, unlike cyclic holds in CFI loading. Comparing Figure 12(b), 12(d), and 12(f), axial strain peaks decrease monotonically before reaching saturation. The stark contrast between FLH simulations with symmetric and non-symmetric stress cyclings is due to the same reason as LCF simulations: the compressive plastic deformation in symmetric cycling leads to a decrease in the axial strain peaks through hardening. Also, comparing CFI simulations (Figure 10(b,e)) with FLH simulations (Figure 12(e,f)) reveals that distributing the total hold duration (100 min) across 100 cycles produces different results than applying it as a single long hold period. This relation is particularly apparent for symmetric stress cycling.

Distributions of critical resolved shear stress (CRSS), named the forest stress (τ_{for}) in the current model, at the peak of the last cycle are illustrated in Figure 13 for LCF and CFI loadings with various stress ratios. Figure 14 presents distribution of total amount of slip over all slip systems (Γ). As it was discussed previously, material under symmetric cyclic loading undergoes an additional hardening during compressive phase of the loading compared to cyclic loading with high mean stress where plasticity occurs only during tension. CRSS and Γ distributions support these findings as the total slip accumulated after 100 cycles is much higher for low mean stress case. The initial value of CRSS ($\tau_{0,for}$) was 80 MPa at the beginning of the simulation for all cases. Loading with low mean stress leads to the promotion of CRSS due to higher slip accumulation while CRSS value is merely modified even after 100 cycles for high mean stress case. Effect of hold durations can also be observed from CRSS and total slip distributions as the plastic slip continues to accumulate during constant stress periods and promotes the CRSS values. Comparing Figures 9, 11, 13, and 14, microstructural regions carrying higher stress than the rest of the RVE appear to have lower slip accumulation and CRSS.

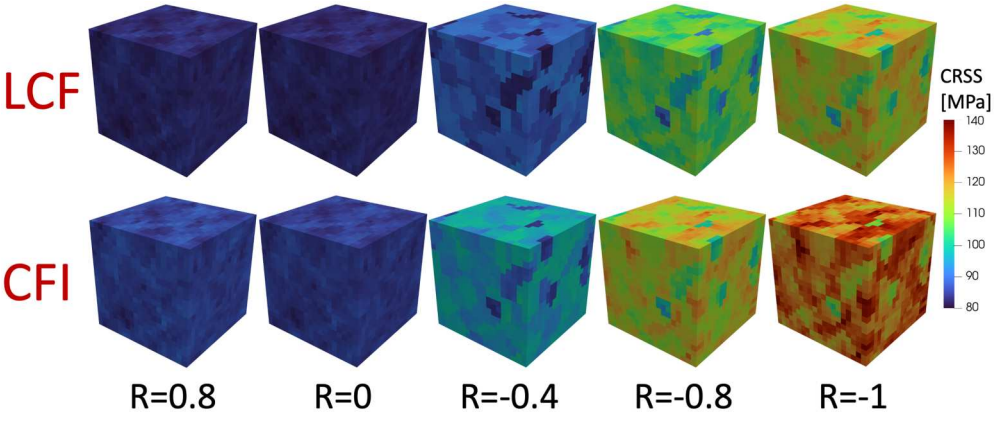

Figure 13. Critical resolved shear stress (CRSS) contours at the peak of the last cycle of LCF and CFI loadings for various stress ratios and corresponding mean stresses.

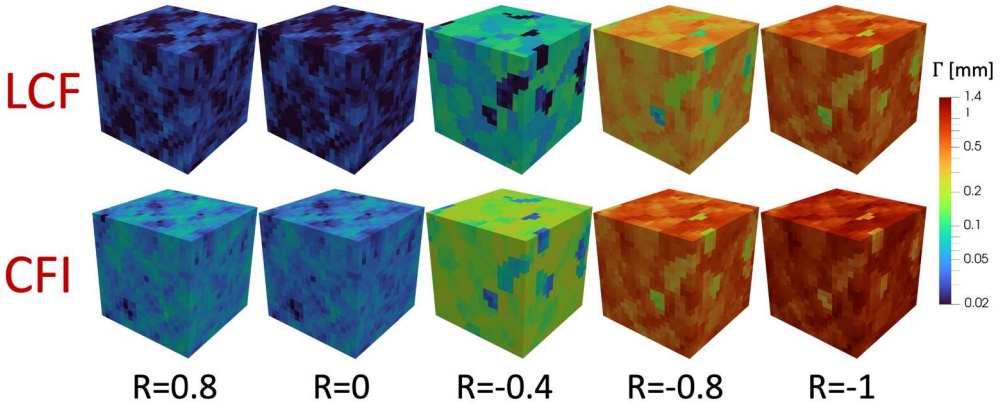

Figure 14. Total slip (Γ) distribution at the peak of the last cycle of LCF and CFI loadings for various stress ratios and corresponding mean stresses.

5. Conclusions

In this study, a crystal plasticity model with combined isotropic–kinematic hardening is used to simulate strain accumulation in 304L stainless steel under stress-controlled cyclic loading and various stress hold conditions at room temperature. The model with calibrated parameters is validated against experimental ratcheting data. Key findings are:

- Under low-cycle fatigue (LCF) loading, high mean stresses lead to continuous strain accumulation, while intermediate and symmetric loading conditions result in strain stabilisation due to compressive loading. High mean stress loading leads to a highly heterogeneous stress response in the microstructure.
- Creep-fatigue interaction (CFI) loading with cyclic stress holds significantly amplify strain accumulation due to time-dependent viscoplastic deformation. CFI loading with high mean stress lead to similar strain accumulation as the static creep loading.
- Fatigue after long hold (FLH) loading produces most of the strain during the initial long hold, and switching to cyclic loading lead to elastic and plastic shakedown under non-symmetric cycling, while symmetric FLH loading shows substantial decrease in accumulated strain due to hardening introduced during long hold.
- The study establishes a numerical framework capable of capturing strain ratcheting response of polycrystal model under a wide range of cyclic loading and stress hold conditions, contributing to improved predictive modelling for aerospace and energy applications.

Disclosure statement

No potential conflict of interest was reported by the author(s).

ORCID

Sadik Sefa Acar http://orcid.org/0009-0003-1854-4823
Tuncay Yalçinkaya http://orcid.org/0000-0002-7982-1105

References

[1] S.K. Paul, *A critical review of experimental aspects in ratcheting fatigue: microstructure to specimen to component*, J. Mater. Res. Technol. 8 (2019), pp. 4894–4914.

[2] B.V. Kalyan, A.H.V. Pavan, B.S. Rao, and N. Narasaiah, *Effect of stress-hold and strain-hold during creep-fatigue interaction of alloy 617 M*, Mater. Today Commun. 39 (2024), p. 108731.

[3] Y. Xu, S. Joseph, P. Karamched, K. Fox, D. Rugg, F.P. Dunne, and D. Dye, *Predicting dwell fatigue life in titanium alloys using modelling and experiment*, Nat. Commun. 11 (2020), p. 5868.

[4] J. Solin, S. Reese, H.E. Karabaki, and W. Mayinger, Research on hold time effects in fatigue of stainless steel: simulation of normal operation between fatigue transients, in Pressure Vessels and Piping Conference, Vol. 56925, Boston, MA, USA, 19–23 July 2015. American Society of Mechanical Engineers, p. V01AT01A030.

[5] R. You, M. Zhang, J. Qiu, C. Fang, C. Zhao, B. Lu, and R. Yang, *Influence of hold time on dwell fatigue behaviour in IMI834 disc forging*, Jom 74 (2022), pp. 3733–3744.

[6] O. Bulut, C. Erdogan, and T. Yalçinkaya, *Dwell fatigue fracture in Ti microstructures through crystal plasticity and phase field fracture frameworks*, Procedia Struct. Integrity 61 (2024), pp. 3–11.

[7] T. Fang, Q.H. Kan, G.Z. Kang, and W.Y. Yan, *Uniaxial ratcheting and low-cycle fatigue failure of U75V rail steel*, Appl. Mech. Mater. 853 (2017), pp. 246–250.

[8] G. Kang, Q. Gao, L. Cai, and Y. Sun, *Experimental study on uniaxial and nonproportionally multiaxial ratcheting of SS304 stainless steel at room and high temperatures*, Nucl. Eng. Des. 216 (2002), pp. 13–26.

[9] G. Kang, Q. Gao, and X. Yang, *Uniaxial and non-proportionally multiaxial ratcheting of SS304 stainless steel at room temperature: experiments and simulations*, Int. J. Non-Linear Mech. 39 (2004), pp. 843–857.

[10] T. Hassan, L. Taleb, and S. Krishna, *Influence of non-proportional loading on ratcheting responses and simulations by two recent cyclic plasticity models*, Int. J. Plast. 24 (2008), pp. 1863–1889.

[11] L. Taleb, *About the cyclic accumulation of the inelastic strain observed in metals subjected to cyclic stress control*, Int. J. Plast. 43 (2013), pp. 1–19.

[12] Y. Dong, Z. Zhang, and X. He, *Microscopic substructures of stainless steel 304 undergoing a uniaxial ratcheting deformation*, Acta Mech. 231 (2020), pp. 4919–4931.

[13] J. Zhao, T. Mo, W. Chen, and F.G. Wang, *Room temperature creep and its influence on fatigue crack growth in a 304 stainless steel*, Key Eng. Mater. 297–300 (2005), pp. 1083–1088.

[14] W. Chen, T. Kitamura, and M. Feng, *Creep and fatigue behavior of 316L stainless steel at room temperature: experiments and a revisit of a unified viscoplasticity model*, Int. J. Fatigue 112 (2018), pp. 70–77.

[15] M. Herbst, A. Roth, and J. Rudolph, Study on hold-time effects in environmental fatigue lifetime of low-alloy steel and austenitic stainless steel in air and under simulated PWR primary water conditions, in Proceedings of the 18th International Conference on Environmental Degradation of Materials in Nuclear Power Systems–Water Reactors, Portland, OR, USA, 13–17 August 2017; 2019. Springer International Publishing, pp. 987–1006.

[16] Y.C. Yoon and S.W. Nam, *A correlation between creep-fatigue life and tensile hold time for austenitic stainless steels*, J. Mater. Sci. Lett. 13 (1994), pp. 1270–1271.

[17] J. Solin, S. Reese, H.E. Karabaki, and W. Mayinger, Fatigue performance of stabilized austenitic stainless steels: experimental investigations respecting operational relevant conditions like temperature and hold time effects, in Proceedings of the ASME 2013 Pressure Vessels and Piping Conference, Volume 1A: Codes and Standards, Paris, France, 14–18 July 2013; 2013, p. V01AT01A022.

[18] G. Kang, Q. Kan, J. Zhang, and Y. Sun, *Time-dependent ratchetting experiments of SS304 stainless steel*, Int. J. Plast. 22 (2006), pp. 858–894.

[19] L. Taleb and G. Cailletaud, *Cyclic accumulation of the inelastic strain in the 304L SS under stress control at room temperature: ratcheting or creep?* Int. J. Plast. 27 (2011), pp. 1936–1958.

[20] L. Taleb and C. Keller, *Experimental contribution for better understanding of ratcheting in 304L SS*, Int. J. Mech. Sci. 146-147 (2018), pp. 527–535.
[21] F. Yoshida, *Uniaxial and biaxial creep-ratcheting behavior of SUS304 stainless steel at room temperature*, Int. J. Press. Ves. Pip. 44 (1990), pp. 207–223.
[22] J. Zhao, T. Mo, and D. Nie, *The occurrence of room-temperature creep in cracked 304 stainless steel specimens and its effect on crack growth behavior*, Mater. Sci. Eng.: A 483-484 (2008), pp. 572–575.
[23] M.E. Kassner, P. Geantil, and R.S. Rosen, *Ambient temperature creep of type 304 stainless steel*, J. Eng. Mater. Technol. 133 (2011), p. 021012.
[24] H. Wang, B. Clausen, C. Tomé, and P. Wu, *Studying the effect of stress relaxation and creep on lattice strain evolution of stainless steel under tension*, Acta Mater. 61 (2013), pp. 1179–1188.
[25] X. Chen and R. Jiao, *Modified kinematic hardening rule for multiaxial ratcheting prediction*, Int. J. Plast. 20 (2004), pp. 871–898.
[26] K. Saï, L. Taleb, F. Guesmi, and G. Cailletaud, *Multi-mechanism modeling of proportional and non-proportional ratchetting of stainless steel 304*, Acta Mech. 225 (2014), pp. 3265–3283.
[27] M.D. Palma, *Modelling of cyclic plasticity for austenitic stainless steels 304L, 316L, 316L (N)-IG*, Fusion Eng. Des. 109 (2016), pp. 20–25.
[28] S.M. Hamidinejad, M.R. Noban, and A. Varvani-Farahani, *Ratcheting of 304 stainless steel alloys subjected to stress-controlled and mixed stress- and strain-controlled conditions evaluated by kinematic hardening rules*, Fatigue Fract. Eng. Mater. Struct. 39 (2016), pp. 238–250.
[29] R. Xing, D. Yu, S. Shi, and X. Chen, *Cyclic deformation of 316L stainless steel and constitutive modeling under non-proportional variable loading path*, Int. J. Plast. 120 (2019), pp. 127–146.
[30] X. Sun, R. Xing, W. Yu, and X. Chen, *Uniaxial ratcheting deformation of 316LN stainless steel with dynamic strain aging: experiments and simulation*, Int. J. Solids Struct. 207 (2020), pp. 196–205.
[31] A. Belattar and L. Taleb, *Experimental and numerical analyses of the cyclic behavior of austenitic stainless steels after prior inelastic histories*, Int. J. Press. Ves. Pip. 189 (2021), p. 104256.
[32] F. Boussalih, K. Fedaoui, and T. Zarza, *Chaboche model for fatigue by ratcheting phenomena of austenitic stainless steel under biaxial sinusoidal loading*, Civ. Eng. J. 8 (2022), pp. 505–518.
[33] K. Hashiguchi, M. Ueno, and T. Anjiki, *Subloading-overstress model: unified constitutive equation for elasto-plastic and elasto-viscoplastic deformations under monotonic and cyclic loadings: research with systematic review*, Arch. Comput. Methods Eng. 30 (2023), pp. 2627–2649.
[34] V. Pandey, P. Arora, S.K. Gupta, N. Khutia, and P.P. Dey, *Validating cyclic plasticity material model for three materials subjected to asynchronous axial-torsion conditions*, Int. J. Fatigue 181 (2024), p. 108124.
[35] G. Kang and Q. Kan, *Constitutive modeling for uniaxial time-dependent ratcheting of SS304 stainless steel*, Mech. Mater. 39 (2007), pp. 488–499.
[36] T. Zhang, X. Wang, D. Zhou, R. Wang, Y. Jiang, X. Zhang, J. Gong, and S. Tu, *A universal constitutive model for hybrid stress-strain controlled creep-fatigue deformation*, Int. J. Mech. Sci. 225 (2022), p. 107369.
[37] R. Du, H. Song, F. Gao, Y. Mo, Z. Yan, Z. Zhuang, and Y. Wei, *Machine learning informed visco-plastic model for the cyclic relaxation of 316H stainless steel at* 550 °C, Int. J. Plast. 170 (2023), p. 103743.
[38] F. Liang, W. Zhang, F. Chen, P. Yin, Q. Yang, L. Chang, and C. Zhou, *Experimental and constitutive modelling studies of type 316L stainless steel based on internal stress under low cycle fatigue and creep-fatigue interaction*, Int. J. Fatigue 175 (2023), p. 107835.
[39] T. Yalcinkaya, W.A.M. Brekelmans, and M.G.D. Geers, *BCC single crystal plasticity modeling and its experimental identification*, Modell. Simul. Mater. Sci. Eng. 16 (2008), p. 85007.
[40] T. Yalçinkaya, W.A.M. Brekelmans, and M.G.D. Geers, *Non-convex rate dependent strain gradient crystal plasticity and deformation patterning*, Int. J. Solids Struct. 49 (2012), pp. 2625–2636.

[41] T. Yalcinkaya, I. Ozdemir, and I.T. Tandogan, *Misorientation and grain boundary orientation dependent grain boundary response in polycrystalline plasticity*, Comput. Mech. 67 (2021), pp. 937–954.
[42] S.S. Acar, O. Bulut, and T. Yalçinkaya, *Crystal plasticity modeling of additively manufactured metallic microstructures*, Procedia Struct. Integrity 35 (2022), pp. 219–227.
[43] T. Yalçinkaya, S.O. Çakmak, and C. Tekoğlu, *A crystal plasticity based finite element framework for RVE calculations of two-phase materials: void nucleation in dual-phase steels*, Finite. Elem. Anal. Des. 187 (2021), p. 103510.
[44] I.U. Aydiner, B. Tatli, and T. Yalçinkaya, *Investigation of failure mechanisms in dual-phase steels through cohesive zone modeling and crystal plasticity frameworks*, Int. J. Plast. 174 (2024), p. 103898.
[45] Y. Dong, G. Kang, and C. Yu, *A dislocation-based cyclic polycrystalline visco-plastic constitutive model for ratchetting of metals with face-centered cubic crystal structure*, Comput. Mater. Sci. 91 (2014), pp. 75–82.
[46] X. Ren, S. Yang, G. Wen, and W. Zhao, *A crystal-plasticity cyclic constitutive model for the ratchetting of polycrystalline material considering dislocation substructures*, Acta Mech. Solida Sin. 33 (2020), pp. 268–280.
[47] X. Ren, S. Yang, W. Zhao, and G. Wen, *A crystal plasticity-based constitutive model for ratchetting of cyclic hardening polycrystalline metals*, Int. J. Dyn. Control 8 (2020), pp. 1161–1168.
[48] T. Zirkle, T. Zhu, and D.L. McDowell, *Micromechanical crystal plasticity back stress evolution within FCC dislocation substructure*, Int. J. Plast. 146 (2021), p. 103082.
[49] Y. Dong, Y. Zhu, F. Wu, and C. Yu, *A dual-scale elasto-viscoplastic constitutive model of metallic materials to describe thermo-mechanically coupled monotonic and cyclic deformations*, Int. J. Mech. Sci. 224 (2022), p. 107332.
[50] S.S. Acar and T. Yalçinkaya, *Modeling of the stress path-dependent strain ratcheting behaviour of 304L stainless steel through crystal plasticity frameworks*, Met. Mater. Int. (2025). https://link.springer.com/article/10.1007/s12540-025-01907-w.
[51] S. Sinha and S. Ghosh, *Modeling cyclic ratcheting based fatigue life of HSLA steels using crystal plasticity FEM simulations and experiments*, Int. J. Fatigue 28 (2006), pp. 1690–1704.
[52] Y. Dong, X. He, and Z. Zhang, *A new crystal plasticity modeling of uniaxial ratcheting behavior for face-centered cubic 6061 aluminum alloy*, Mater. Res. Express 7 (2020), p. 106515.
[53] J. Wang, H. Lu, Z. Wen, Y. Lian, Y. Wang, and Z. Yue, *Crystal plasticity theory coupled with meso-damage to predict the ratchetting behavior of nickel-based single crystal superalloy*, Int. J. Fatigue 165 (2022), p. 107220.
[54] H. Li, C. Yu, and G. Kang, *Crystal plasticity modeling of the multiaxial ratchetting of extruded AZ31 Mg alloy*, Int. J. Plast. 152 (2022), p. 103242.
[55] Y. Lei, C. Yu, Z. Wang, X. Xu, H. Li, and G. Kang, *Multi-mechanism constitutive model for uniaxial ratchetting of extruded AZ31 magnesium alloy at room temperature*, Mech. Mater. 179 (2023), p. 104607.
[56] B. Wu, X. Xu, X. Zhang, C. Yu, Z. Wen, P. Wang, and Q. Kan, *A crystal plasticity model for multiaxial cyclic deformation of U75V rail steel*, Int. J. Fatigue 183 (2024), p. 108232.
[57] B. Zhang, R. Wang, D. Hu, K. Jiang, X. Hao, J. Mao, and F. Jing, *Constitutive modelling of ratcheting behaviour for nickel-based single crystal superalloy under thermomechanical fatigue loading considering microstructure evolution*, Int. J. Fatigue 139 (2020), p. 105786.
[58] D. Agius, A.A. Mamun, C.A. Simpson, C. Truman, Y. Wang, M. Mostafavi, and D. Knowles, *Microstructure-informed, predictive crystal plasticity finite element model of fatigue-dwells*, Comput. Mater. Sci. 183 (2020), p. 109823.
[59] D. Zhou, X. Wang, R. Wang, T. Zhang, X. Yang, Y. Jiang, X. Zhang, J. Gong, and S. Tu, *An extended crystal plasticity model to simulate the deformation behaviors of hybrid stress–strain controlled creep-fatigue interaction loading*, Int. J. Fatigue 156 (2022), p. 106680.
[60] J.A. Wollmershauser, B. Clausen, and S.R. Agnew, *A slip system-based kinematic hardening model application to in situ neutron diffraction of cyclic deformation of austenitic stainless steel*, Int. J. Fatigue 36 (2012), pp. 181–193.

[61] F. Roters, M. Diehl, P. Shanthraj, P. Eisenlohr, C. Reuber, S.L. Wong, and D. Raabe, *DAMASK–The Düsseldorf Advanced Material Simulation Kit for modeling multi-physics crystal plasticity, thermal, and damage phenomena from the single crystal up to the component scale*, Comput. Mater. Sci. 158 (2019), pp. 420–478.
[62] P. Shanthraj, P. Eisenlohr, M. Diehl, and F. Roters, *Numerically robust spectral methods for crystal plasticity simulations of heterogeneous materials*, Int. J. Plast. 66 (2015), pp. 31–45.
[63] Y. Wang, D.D. Sun, Y.P. Bai, and Z.X. Pang, *Study on grain size control technology of 304L austenitic stainless steel*, in *Journal of Physics: Conference Series*, Vol. 2045, IOP Publishing, 2021, p. 12023
[64] Y. Charles, C. Zhang, M. Gaspérini, and B. Bacroix, *Identification methodology of a rate-sensitive constitutive law with mean field and full field modeling approaches for polycrystalline materials*, C.R. Méc. 348 (2021), pp. 807–826.
[65] F. Harewood and P. McHugh, *Comparison of the implicit and explicit finite element methods using crystal plasticity*, Comput. Mater. Sci. 39 (2007), pp. 481–494.
[66] S.E. Shawish and L. Cizelj, *Combining single- and poly-crystalline measurements for identification of crystal plasticity parameters: application to austenitic stainless steel*, Crystals 7 (2017), pp. 181.
[67] Y. Jeong and T. Manninen, *Formability predictions and measurement of 316L stainless steel using self-consistent crystal plasticity*, J. Phys. Conf. Ser. 1063 (2018), p. 012020.
[68] K. Frydrych, *Simulations of grain refinement in various steels using the three-scale crystal plasticity model*, Metall. Mater. Trans. A 50 (2019), pp. 4913–4919.
[69] M. Lindroos, M. Isakov, and A. Laukkanen, *Crystal plasticity modeling of transformation plasticity and adiabatic heating effects of metastable austenitic stainless steels*, Int. J. Solids Struct. 236–237 (2022), p. 111322.
[70] N. Mehani and S.C. Roy, *Modified isotropic and kinematic hardening equations for 304L SS under low cycle fatigue*, Comput. Mater. Sci. 240 (2024), p. 112999.

Philosophical Magazine

ISSN: 1478-6435 (Print) 1478-6443 (Online) Journal homepage: www.tandfonline.com/journals/tphm20

Electron density mapping analysis using XRD and tailoring of the optical and magnetic properties in Ni doped SnO_2

K. KaviyaPandimeena, M. Charles Robert, N. Pavithra, Y.B. Kannan & P. Christuraj

To cite this article: K. KaviyaPandimeena, M. Charles Robert, N. Pavithra, Y.B. Kannan & P. Christuraj (2025) Electron density mapping analysis using XRD and tailoring of the optical and magnetic properties in Ni doped SnO_2, Philosophical Magazine, 105:18, 1087-1113, DOI: 10.1080/14786435.2025.2469816

To link to this article: https://doi.org/10.1080/14786435.2025.2469816

PHILOSOPHICAL MAGAZINE
2025, VOL. 105, NO. 18, 1087–1113
https://doi.org/10.1080/14786435.2025.2469816

Taylor & Francis
Taylor & Francis Group

Electron density mapping analysis using XRD and tailoring of the optical and magnetic properties in Ni doped SnO_2

K. KaviyaPandimeena [a], M. Charles Robert [a], N. Pavithra[a], Y.B. Kannan[b] and P. Christuraj[c]

[a]PG and Research Department of Physics, (Affiliated to Madurai Kamaraj University, Madurai), HKRH College, Theni, India; [b]Department of Physics, Arumugam Pillai Seethai Ammal College, Tiruppattur, India; [c]Department of Physics, St. Joseph's College, Tiruchirappalli, India

ABSTRACT

Single-phase Ni-doped SnO_2 with concentrations of 2.5%, 5%, and 7.5% was prepared by the simple co-precipitation method and studied to tailor the optical energy gap and magnetism useful for diluted magnetic semiconductor (DMS) applications. In all compositions, XRD analysis shows Ni doping with no peak shift. Ni doping in SnO_2 increases the energy band gap from 3.51 eV to 4.09 eV, reducing optical absorbance. Room-temperature PL emission with excitation at 320 nm produces strong red emissions. Room-temperature magnetic investigations show that 2.5% Ni doping in pure SnO_2 changes diamagnetism to soft ferromagnetism with 0.5 emu/g magnetisation and 149 Oe coercivity. More Ni doping reduces magnetisation and leads to paramagnetism, which is attributed to interstitial charge accumulation. The Rietveld analysis of the XRD data reveals a cation deficiency, while the maximum entropy method (MEM) analysis of the electronic structure and bonding behaviour reveals the maximum dilution of Ni^{2+} ions in the Sn^{4+} host site at 2.5% doping. Further doping increases interstitial charge accumulation, defects, and magnetisation reduction. MEM also shows a new empirical conclusion: for magnetism to be fully developed, the Ni^{2+} needs to be diluted correctly in the Sn^{4+} host lattice so that there is no charge buildup between the atoms (interstitial) and the Sn/Ni-O covalency needs to be maximum in both apical and equatorial directions. In conclusion, a dilute Ni-doped SnO_2 system allowed to achieve a soft ferromagnetic transition and optical band tuning.

ARTICLE HISTORY
Received 6 June 2023
Accepted 15 February 2025

KEYWORDS
Crystallography; XRD; bonding; electronic structure; ferromagnetism; magnetic materials

1. Introduction

In the most recent few years, the focus of the scientific community has shifted toward dilute magnetic semiconductors (DMS) because of the vast number of

CONTACT M. Charles Robert jothycharles@gmail.com PG and Research Department of Physics, (Affiliated to Madurai Kamaraj University, Madurai), HKRH College, Uthamapalayam, Theni, Tamil Nadu, India
Supplemental data for this article can be accessed online at https://doi.org/10.1080/14786435.2025.2469816.

uses that they have in the nanoworld. Researchers specifically investigated room-temperature ferromagnetism (RTFM) and photoluminescence on the DMS materials for spintronics and optical device applications. The electrons' spin and charge improve the performance of semiconductor devices and magnetic storage devices, respectively. Doping with transition metals like iron, nickel, manganese, cobalt, chromium, and others caused the spin and charge to be tailored for the creation of ferromagnetic dilute magnetic semiconductors that are optically transparent [1–3]. Ferromagnetism at room temperature is one of the pre-requisite characteristics that is a prerequisite in materials for spintronic applications. Ming Hao reported that Mn-doped zinc oxide (ZnO) has the property of RTFM [4]. Transition metal dopants can tune the ferromagnetism of semiconductors [5]. In order to induce performance in different application fields, doping non-magnetic semiconductors with magnetic particles resulted in improved semiconductor performance. Some authors have observed that transition metal-doped oxide semiconductors may exhibit ferromagnetism at ambient temperature [5]. Mousa Aliahmad [6] has reported the superparamagnetism of Ni-doped SnO_2. In contrast to reports about other oxide-based DM semiconductors, less information is available concerning SnO_2-based DMS materials [7].

Tin oxide (SnO_2) is an n-type semiconductor with a large band gap of 3.6 eV, like TiO_2 and ZnO [8,9]. It can be used in optical and spintronic applications. When doped with transition metals and possessing a significant magnetic moment, SnO_2 emerges as one of the most sought-after RTFM semiconductors [10]. Various applications, including LEDs with a wide emission range, have optimised the optical properties of TM-doped SnO_2 [11,12]. Researchers have described numerous experimental investigations on the PL spectrum of SnO_2 doped with various transition metals [13,14]. The Ni and Cu dopants increase the optical, magnetic, and electrical characteristics of SnO_2, which offer a wide range of applications, particularly in sensors and optoelectronics [15,16]. Airinei et al. [11] found that the system's band gap increases as the Ni concentration rises. Low concentrations of Ni, according to Sharma et al., have greater saturation magnetisation [11]. SnO_2 doped with transition metals is a good material for developing multifunctional magneto-optoelectronic devices [17]. SnO_2 doped with the transition elements (Fe, Ni, Co, Cr, and Mn) is well known as a magnetic semiconductor used in the field of spintronics [8]. Punnoose et al. reported the paramagnetic behaviour of Ni^{2+} ions on the Sn host lattice [18]. Fitzgerals et al. reported ferromagnetism with a magnetic moment of 0.98 μB in iron-doped SnO_2. [3] Several authors have reported on the structural properties of Ni-doped SnO_2 [11,15,19]. Furthermore, Coey et al. [20] proposed the defect-induced model of ferromagnetism, which can enhance magnetism in TM-co-doped DMS.

The electron density, mobility, and spin determine the magnetisation and semiconducting characteristics of DMS materials. Therefore, knowledge of the

local structure and electronic structure is of the utmost importance for DMS-based device applications. The magnetic properties of the dilute transition metal-doped SnO_2 system are completely dependent on the magnitude and spin orientation of the lattice, as well as the interstitial site occupation of magnetic ions. Therefore, we must address the electronic charge characterisation, which includes the electron density distribution inside the unit cell, the type and strength of bonding, and the occupation of charges at both interstitial and lattice points. The majority of articles in this field focus on preparation, optical, and magnetic characterisation. There is a research gap in this field, as no article reveals the analysis of electron density, its visual mapping, or its local structure. Further, none of the studies reveals the correlation between electronic structure and magnetism. We dedicate this study to the synthesis, optical, photoluminescence, and magnetic characterisation of dilute Ni doping in SnO_2, along with the comprehensive observation and bonding of electron density using XRD data through the maximum entropy method (MEM). Furthermore, the atomic pair distribution study, which uses XRD data, quantifies atomic-level interactions with the closest neighbours. This work's highlight is an electron-level empirical correlation between magnetism and electronic structure.

2. Materials and methods

The chemical precipitation method was used to produce Ni-doped SnO_2 ($Ni_xSn_{1-x}O_2$) with three distinct Ni concentrations ($x = 0.025$, 0.05, and 0.075), as the chemical precipitation process is cost-effective and practical, which provides error-free stoichiometry, low temperature, and homogeneity control [21]. As precursors, stannous chloride ($SnCl_2$), nickel chloride ($NiCl_2$ $6H_2O$), and ammonia solution (NH_4OH) were used. Stochiometric amounts of stannous chloride and nickel chloride were dissolved in 100 ml of distilled water and agitated for 20 min with a magnetic stirrer. Following the addition of ammonia solution, the precursor solution was stirred until full precipitation. The precipitated sample was dried at 80°C for 24 h and calcinated at 500°C for 2 h. For a typical example of the synthesis of $Ni_{0.05}Sn_{0.95}O_2$, 1.8012 grams of stannous chloride (0.095 M), 0.18 grams of nickel chloride (0.005 M), and 35 ml of ammonia solution were used in 100 ml of deionised water. The calcinated sample is ground to a fine powder using a mortar and pestle and filtered using a 400-micrometer nylon mesh for further characterisation.

2.1. Experimental analysis

Powder XRD data were collected using a BRUKER advance D8 EVO diffractometer with a scan step size of 0.02° and a Bragg angle (2θ) range of 10° to 100° using Cu target with Kα radiation (λ = 1.5405 Å). The surface morphological investigation for microstructural information was recorded using

transmission electron microscopy (TEM) equipment type FEI Tecnai G^2 20-S-TWIN TEM working under 200 kV field emission gun with super twin lens of point and lattice resolution 0.24 and 0.1 nm respectively. The optical absorption spectra of the material was measured across the wavelength range of 220–1400 nm with a step size of 1 nm using a UV-visible-NIR spectrometer, model SHIMADZU/UV 2600 having 0.1 nm wavelength accuracy and resolution. The instrument model SHIMADZU/RF 6000 with 1 nm resolution recorded the photoluminescence spectra across the wavelength range of 300–800 nm, with an excitation wavelength of 320 nm, to detect photoemission and chromaticity in the visible light area. At room temperature, magnetic measurements were performed using a vibrating sample magnetometer (VSM) with the instrument model Lakeshore 7410S and a maximum applied magnetic field of 15 kOe. ESR spectrometer JEOL model JES FA200 was used to look at the oxidation states of Ni ions in the X-band frequency range of 8.75–9.65 GHz. It has a resolution of 2.35 μT and a sensitivity of 7×10^9 spins/0.1 mT.

2.2. Computational analysis

The Rietveld profile fitting technique was used to analyse average structural information based on initial structural parameters such as tetragonal structure (space group P42/mnm) and reported lattice parameters of SnO_2, a = b = 4.737 Å and c = 3.186 Å [22,23]. The JANA2006 programme [24] was utilised to refine lattice parameters, peak shape parameters, asymmetry and background parameters, as well as atomic location and occupancy. The generated profile contains computed and observed intensities, Bragg positions, and error information. The MEM entropy maximisation approach [25] was used to determine the electron density in each pixel ($128 \times 128 \times 108$) of the unit cell using the observed structure and structural factors. The programme Dysnomia was used to rebuild electron density using XRD-based structural factors [26]. We created a comprehensive map of electron density using the graphical programme VESTA [27]. Using the pair distribution function (PDF) and the programme PDFgetX [28], correlations of the atomic and ionic closest neighbour bond lengths were determined. The PDF generated from experimental XRD data was matched with an appropriate crystallographic model using PDFgui [29], yielding precise lattice parameters, bond length of closest neighbour atoms or ions, and number of nearest neighbours.

3. Results and discussion

3.1. Experimental analysis

3.1.1. Experimental XRD data analysis

Figure 1 displays the experimental XRD intensity data for Ni-doped SnO_2 material. The scanning angle 2θ is plotted from 20° to 100° because there

were no peaks in the 10° to 20° region for any of the Ni compositions that were made. The well-defined and intense XRD Bragg peaks are evidence that the samples had a high degree of crystallinity. Each sample's peak location reveals the rutile type tetragonal structure of SnO_2. This structure is in accordance with JCPDS 41–1445 and follows the space group P42/mnm [13]. Every doping composition displays three minuscule extra peaks. The first peak, located at 24° and designated by a black solid circle, belongs to the orthorhombic phase of SnO_2, while the other two peaks, located at 30.59° and 46.52° and signified by a black solid diamond, signify a very tiny contribution of the Sn post-transition metal peak. Carvolha et al. [30] had previously documented the existence of these extra peaks.

The peak shift in relation to doping concentration is not noticeable due to two possible reasons: the first is that there is a very small difference between the ionic radii of the dopant Ni^{2+} (ionic radii = 0.72 Å) and the ionic radius of the host cation Sn^{4+} (ionic radius = 0.71 Å), confirming the doping of Ni^{2+} ions in the host lattice, and the second is the dilute quantity of doping. Only a little shift (inset of Figure 1) towards the lower 2θ angle is observed due to the small ionic difference between the host and dopant ions. The inset of Figure 1 also shows the full width at half maximum value (FWHM) for the prominent plane (110) and their corresponding crystallite sizes, calculated using

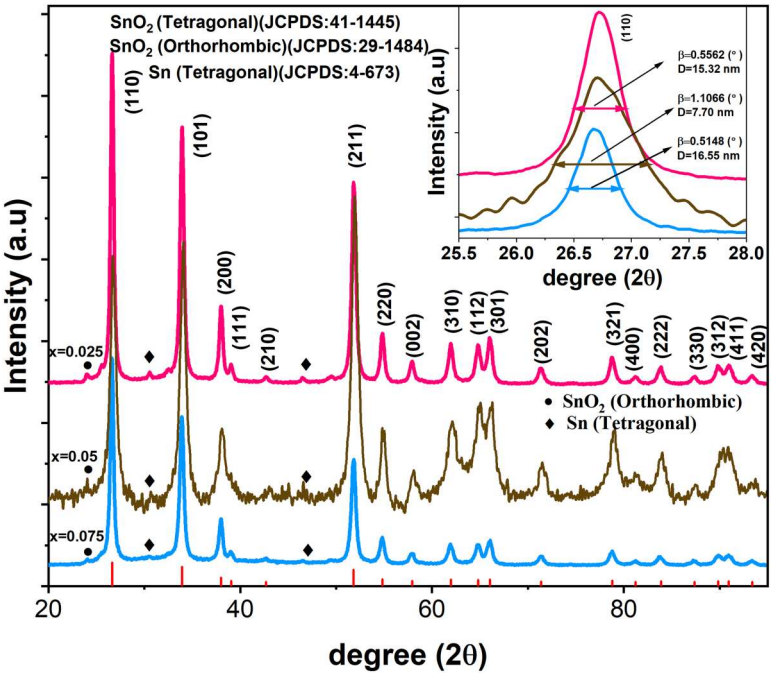

Figure 1. Experimental X-ray intensity plot of $Ni_xSn_{1-x}O_2$: $x = 0.025$, 0.05, 0.075, showing the perfect crystallinity, rutile structure, with very little SnO_2 orthorhombic and post transition Sn metal phases. The inset shows the expanded major peak (110) with the crystallite size.

the Scherrer equation using the formula ($D = 0.9\,\lambda/\beta\cos\theta$), where β, θ, and λ are the full width at half maximum, the diffracting angle, and the wavelength of the X-ray used, respectively [31]. This method considers the XRD peak broadening only due to crystallite size effects, without considering the microstructural strain due to point defects, stacking faults, and the size and ionic radii of dopants. The FWHM for the 5% Mn-doped sample has a maximum value of 1.1066°, leading to a minimum nanocrystal size of 7.7 nm. The Halder-Wagner method is used, which is based on the assumption that peak broadening is a Voigt function as it is a convolution of Lorentzian function and gaussian function, which considers both crystallite size and microstructural lattice strain. Figure 2 is a plot of $(\beta^*/d^*)^2$ vs. (β^*/d^{*2}), the Halder-Wagner plot, which estimates the crystallite size and lattice strain. In this plot, $\beta^* = \beta\cos\theta/\lambda$ and $d^* = 2d\sin\theta/\lambda$, with β, d, θ, and λ being the full width at half maximum, the distance between planes in the reciprocal lattice, the diffracting angle, and the wavelength of the X-ray used, respectively [32]. Section 3.4.3 discusses the crystallite size that we obtained from the pair distribution function. Table 1 presents the estimated crystallite size, porosity, and lattice parameters using various

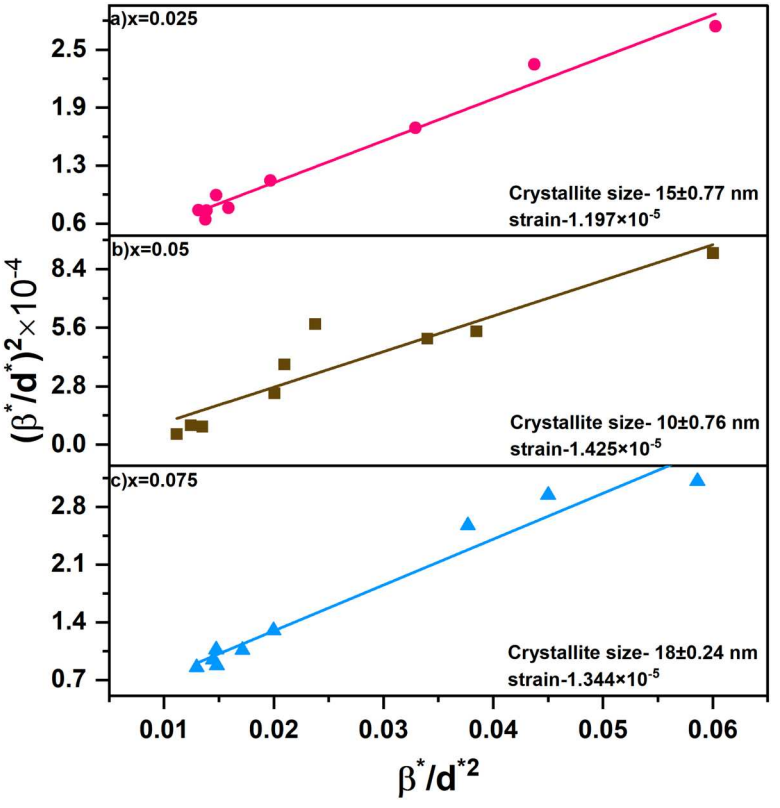

Figure 2. Halder – Wagner plot for precise crystallite size and lattice strain estimation. The perfect dilution of Ni^{2+} dopant in host Sn^{4+} lattice due to comparable ionic radii reduces lattice strain.

Table 1. Various structural parameters obtained from XRD data. Crystallite size and porosity are minimum for the 5% Ni doped composition.

Sample name	Crystallite size (nm)						Cell parameters using unit cell refinement (Å)	
$Ni_xSn_{1-x}O_2$	Scherrer method	Halder – Wagner method	PDF method	Bulk density (g/cm^3)	X-ray density (g/cm^3)	Porosity (%)	a = b	c
x = 0.025	15 ± 0.32	15 ± 0.77	15	6.775	6.887	1.626	4.746(2)	3.192(6)
x = 0.05	7 ± 0.71	10 ± 0.76	9	6.566	6.600	0.515	4.751(4)	3.193(5)
x = 0.075	16 ± 0.55	18 ± 0.24	17	6.535	6.588	0.799	4.747(1)	3.195(3)

methodologies. Table 1 reveals that doping has minimal effect on the lattice parameter. The least value of lattice strain for all compositions, of the order of 10^{-5}, supports this argument. Bulk and x-ray density methods calculate a porosity that is almost smaller, indicating a very low porosity.

3.1.2. Surface morphology

Transmission electron microscopy (TEM) was used to examine the surface morphology of Ni-doped SnO_2. Transmission electron microscopy (TEM) is widely regarded as the preferred method for assessing the surface morphology, namely the size and shape, of nanoparticles. The initial stage of the characterisation process necessitates a visual inspection of the objects under examination. Understanding the size distribution of particulate materials has significant importance due to many factors, particularly when these materials are anticipated to consist of minuscule particles, such as nanoparticles, which are particles measuring up to around 100 nm or less in size. Transmission electron microscopy (TEM), which is different from optical microscopes, uses visible light to magnify nanoscale structures by up to 50 million times. This makes it easier to look at tiny details at the atomic level. The rationale for this phenomenon is that electrons may exhibit a significantly reduced wavelength (about 100,000 times shorter) compared to visible light when exposed to a strong electromagnetic field. Consequently, the introduction of TEM in materials research leads to a substantial improvement in nanoscale research.

Figure 3(a–c) presents the surface morphological analysis images of $Ni_xSn_{1-x}O_2$ at $x = 0.025$, 0.05, and 0.075, with varying ranges of 50 and 20 nm. The prepared particles exhibit good dispersion and a moderately uniform particle size. These TEM photos suggest that the increased Ni doping concentration does not significantly alter the nanoparticle morphology. At 2.5% Ni concentration, a moderate hexagonal morphology is present, but diminishes as the doping concentration increases. No spherical-shaped morphology is seen in all samples. $Ni_xSn_{1-x}O_2$: $x = 0.025$, 0.05, and 0.075 nanoparticles had an average particle size of 59, 45, and 64 nm, respectively. The TEM determined the average particle size to be larger than the XRD anticipated

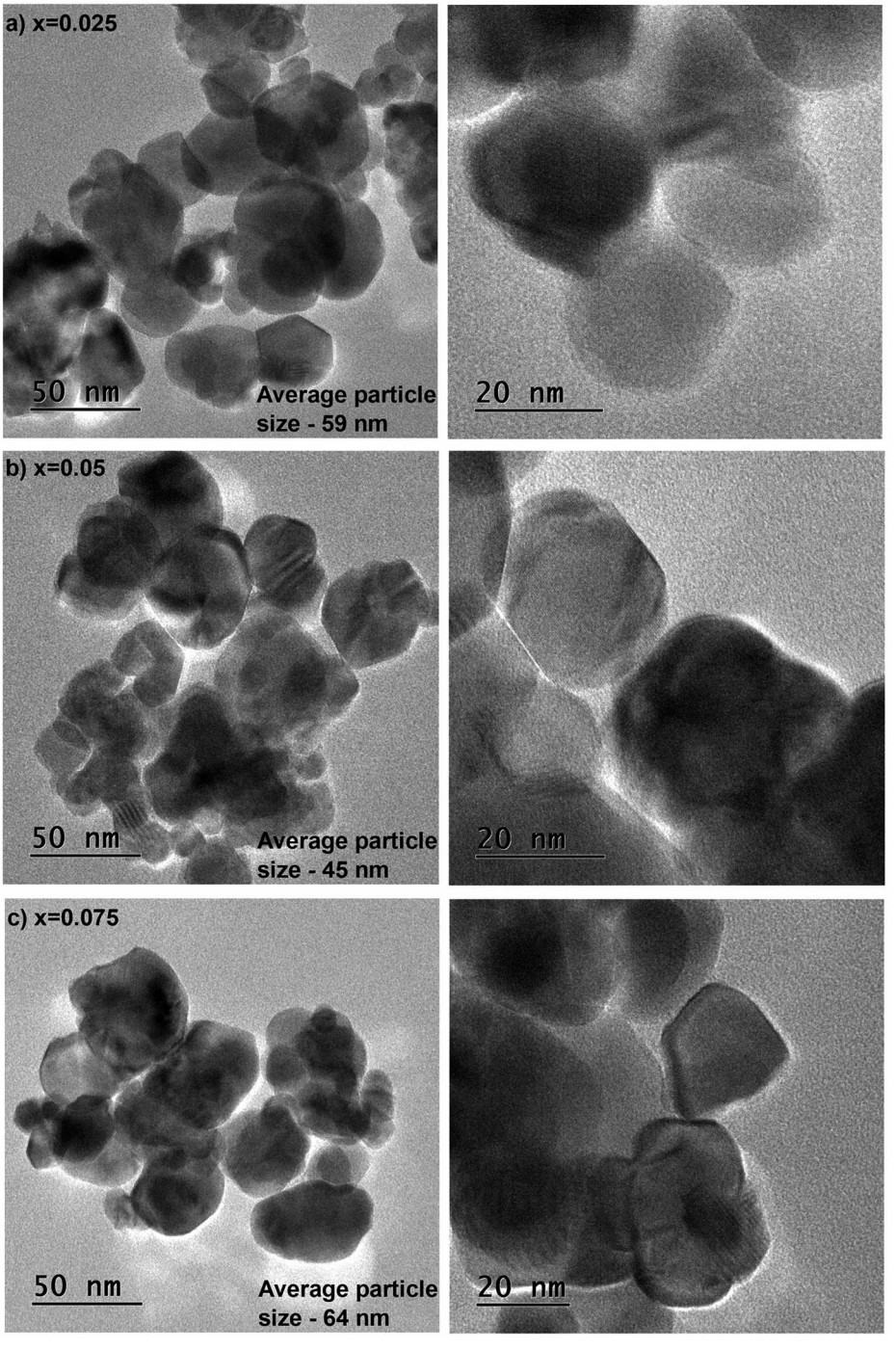

Figure 3. (a–c) TEM images of the prepared samples with insignificant morphological changes with Ni doping with different magnifications such as 50 and 20 nm.

crystallite size, indicating a large number of small agglomerated crystallites of different ranges in the particles. All compositions exhibit particle agglomeration, with the lowest degree occurring at $x = 0.025$ and increasing as the doping concentration reaches its maximum at $x = 0.075$. Previous reports have indicated that the presence of OH ions in co-precipitated samples is the reason for this particle agglomeration.

3.1.3. UV-Vis NIR analysis

The optical properties will provide a window into the electronic band-level properties, which will aid in the comprehension of electrical conduction in DMS materials. Absorption and fluorescence spectroscopies are efficient techniques for identifying the optical properties of semiconducting materials. Figure 4 illustrates the UV-visible optical absorption spectra of Ni-doped SnO_2 at different concentrations. The concentration of Ni dopant has little effect on the absorption edges. Absorbance spectra provide a variety of parameters, such as band gap, impurity centre, oxygen vacancy or deficiency, and surface roughness. According to Figure 4, the absorbance spectrum has a transition region between 270 and 300 nm that can be ascribed to the photoexcitation of electrons between the valence and conduction bands. The inset of Figure 4 depicts the energy gap resulting from Tauc's relation, as depicted by

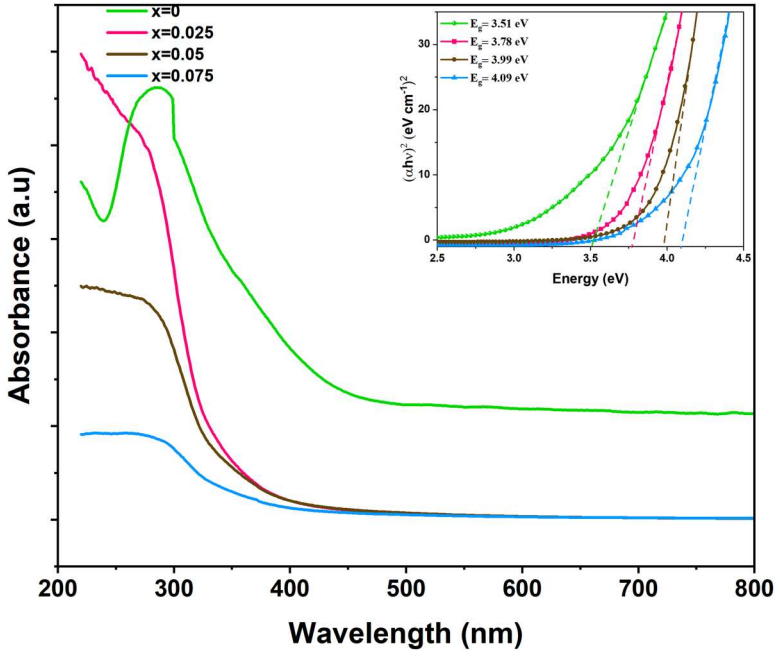

Figure 4. UV-Vis-NIR absorption spectrum of SnO_2 and (2.5%, 5% and 7.5%) Ni doped SnO_2. A gradual decrease in absorption intensity and a slight shift in absorption edge is seen. Inset is the Tauc plot, estimate the energy band gap, which increases with Ni doping.

the following equation [33]:

$$(\alpha h\nu)^{1/n} = A(h\nu - E_g) \quad (1)$$

where h, α, ν and E_g are plank's constant, absorption coefficient, and frequency of radiation, respectively. For a direct band transition, the value of n is 1/2. The band gap values are calculated by extrapolation of the linear region of the plot between $(\alpha h\nu)^2$ and hν. The inset of Figure 4 compares the band gaps of undoped SnO_2 and Ni-doped SnO_2 of various compositions. Pure SnO_2 has a band gap of 3.51 eV. In contrast to what was observed before [34], it is interesting to see that the energy gap values rise from 3.78 eV to 4.09 eV as the Ni doping concentration increases. This is because the Ni doping concentration increases in the near-ultraviolet region with wavelengths between 328 and 303 nm. Based on the exact Rietveld refinement results (section 3.4.1, Table 3), the cation deficiency is between 9% and 28.4%. This deficiency in cations is equivalent to an excess of anions. As the concentration of Ni dopant ions rises, so does the occupancy of Ni^{2+} in the interstitial sites, in addition to the occupied Sn^{4+} lattice sites. Due to the excess of electrons, the charge carrier increases, causing the fermi level to migrate to a higher energy level within the conduction band. The orbitals of the dopant atom in the valence and conduction bands result in hybridisation with the existing orbitals, thereby widening the forbidden band gap. The variation of band due to doping concentration causes the Moss-Burstein effect, where the net energy gap is the sum of the actual band gap and the negative Moss-Burstein shift. Since all states below the fermi levels are occupied, electrons can only be excited from the top of the valance band to the bottom of the conduction band. Increasing the band gap in semiconductors increases conductivity owing to the conduction electron obtained by ionisation of the donor level caused by dopant in the presence of temperature [35].

3.1.4. PL-spectrum

Figure 5 depicts the photo-induced fluorescence spectra of $Ni_xSn_{1-x}O_2$ (x = 0.025, 0.05, and 0.075) at an excitation wavelength of 320 nm. The PL curves exhibit two emission maxima, one in the UV region at 311 nm wavelength and the other in the visible region at 638 nm wavelength. The near-band edge emission (NBE) is responsible for the first peak at 311 nm, which is caused by the recombination of photogenerated charge carriers. Other than this peak, the next prominent peak observed at 638 nm is attributed to an oxygen defect known as an oxygen vacancy or an interstitial-related shallow and deep trap centre. Oxygen vacancy is the most prevalent defect in metal oxides, with three distinct charge states represented by v_o^0, v_o^+, and v_o^{2+} [36]. Due to the radiative recombination of electrons in deep-level states with the photoexcited hole in the valance band, the peak in the visible region is

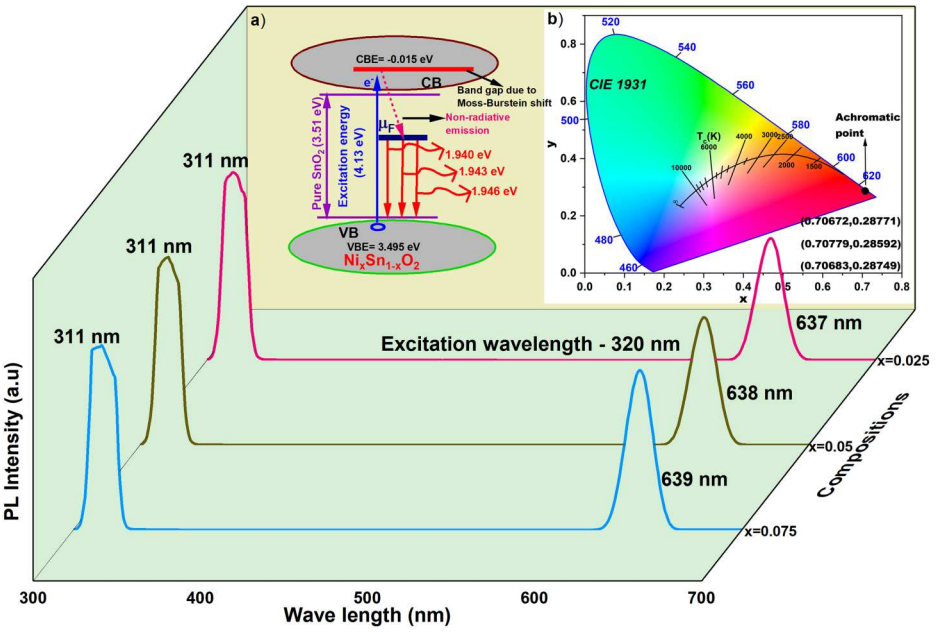

Figure 5. Photoluminescence emission spectra of (2.5%, 5% and 7.5%) Ni doped SnO_2 for the excitation wavelength of 320 nm. Inset (a) is the energy level diagram explaining the excitation and emission process and (b) the CIE diagram showing the achromatic point in the red region.

attributed to deep trap centres. With an increase in Ni dopant concentration from $x = 0.025$ to $x = 0.075$, the absorption peak shifts. With Ni doping, the wavelength and intensity of the robust band increase from 637 nm to 639 nm. Peak at 311 nm tend to blend together. As a result of the substitutional incorporation of Sn^{4+} ions by Ni^{2+} ions, the –2 charge of the substituted Sn^{4+} ion must be compensated from the lattice in the form of oxygen vacancies, which act as radiative luminescence centres and give rise to defect levels, thereby increasing the photoluminescence intensity of Ni-doped SnO_2 samples. $Ni_xSn_{1-x}O_2$ (x = 0.075) has the greatest intensity of photoluminescence.

The presence of a high absorbance results in a greater number of photogenerated charge carriers on the surface, thereby enhancing charge transfer and recombination between the carriers. In the present investigation, this high intensity (3,967107 a u) will govern the photocatalytic activity. All of the samples exhibit reasonable absorption and high-intensity PL emission, which enables their application to photocatalysis. Inset (a) of Figure 5 depicts the charge carrier relaxation process. Charge carriers are excited to the conduction band by the excitation energy of 4.13 eV (excitation wavelength = 320 nm). Initially, a nonradiative transition from the conduction band to the intermediate energy levels is produced by the accumulation of interstitial charge caused by Ni^{2+} doping. These electrons then recombine with the holes in the confined

acceptor levels, resulting in the high-intensity emission of wavelength in the red region. The visible emission spectrum of Ni-doped SnO_2 is converted into (x, y) coordinates using luminescence data according to the Comission Internationale de l'Eclairage standard. The CIE 1931 RGB colour space and CIE colour space were created by the International Commission on Illumination in 1931. The experimental results were combined into the specification of the CIE RGB (red, green, and blue) colour space, from which the CIE XYZ colour space was derived. The chromaticity of $Ni_xSn_{1-x}O_2$ ($x = 0.025$, 0.05, 0.075) depicted in inset (b) of Figure 5 concludes that its CIE coordinates are close to (0.707, 0.287), which corresponds to the visible red region. Due to the incorporation of Ni^{2+} ions in the SnO_2 host lattice, the chromaticity shifts from white to red, as demonstrated by the chromaticity diagram.

3.1.5. VSM hysteresis analysis

A non-destructive device, the Vibration Sample Magnetometer (VSM), measures the magnetism inside samples precisely and sensitively. This technique is applicable to magnetic materials of the ferromagnetic, paramagnetic, and diamagnetic nature. A vibration sample magnetometer (VSM) can ascertain the magnetic characteristics such as coercivity, saturation magnetisation, and retentivity, as well as the origin of magnetism. Figure 6 depicts the magnetic properties of Ni-doped SnO_2 nanoparticles. Table 2 provides the magnetic parameters. The important experimental results observed are also embedded within the figure itself. Due to the 4 + valence state of Sn and the lack of unpaired electrons in the $4d^{10}$ electronic configuration, nanocrystalline SnO_2 that has not been doped displays little d^0 magnetism. Due to the deposition of magnetic Ni^{2+} ions, the insertion of a dilute amount of Ni into the SnO_2 structure causes a transition from diamagnetism to ferromagnetism.

The expanded form of the M-H curve in Figure 6 inset (a) illustrates the magnetic coercivity and retentivity. Inset a of Figure 6 displays the asymmetric nature of hysteresis, and the formula $Hc = (Hc_+ - Hc_-)/2$ calculates the coercivity. This may be due to the coexistence of both ferro and anti-ferro magnetic domains. For the composition $x = 0.025$, we obtain a maximal magnetic saturation of 0.5 emu/g with mild ferromagnetism and coercivity of 149 Oe due to the increased number of unpaired electrons. Adding more dopants abruptly decreases the magnetisation at saturation. These results might be due to two things: the cancelling of magnetic moments between the non-collinear spin configuration of regular lattice site Ni^{2+} dopants and interstitial Ni2+ ions, and the Ni^{2+} and oxygen vacancies spinning in the opposite direction of each other. Inset (b) of Figure 6 shows the M^2 versus H/M plot (Arrott Plot) for studying where the spontaneous magnetisation comes from. This shows that $Ni_{0.025}Fe_{0.975}O_2$ is a soft ferromagnet (from the plateau region of the curve) with a low spontaneous magnetisation $M = 0.5616$ emu/g. Paramagnetism occurs when Ni is added beyond $x = 0.025$. The sample with

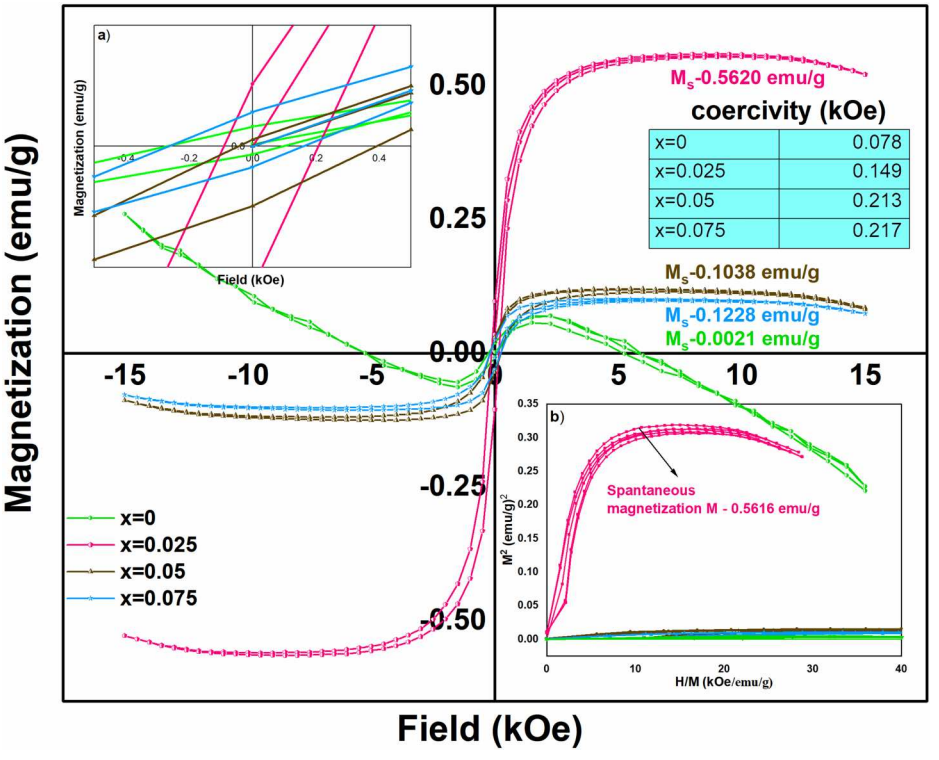

Figure 6. VSM hysteresis analysis of Ni doped SnO_2, showing a switching from d0 magnetism of SnO_2 to soft ferromagnetism of $Ni_{0.025}Sn_{0.975}O_2$. Further increase in Ni doping leads to paramagnetism. Inset (a) shows the expanded form of VSM plot for coercivity values and (b) Arrott plot, shows little spontaneous magnetisation for the 2.5% Ni doped sample.

Table 2. The magnetic parameters of Ni doped SnO_2 with various composition ($x = 0.025$, 0.05 and 0.075).

Parameters	$x = 0$	$x = 0.025$	$x = 0.05$	$x = 0.075$
Magnetisation at 1.5 T (emu/g)	0.0021	0.5620	0.1038	0.1228
Coercivity H_c (kOe)	0.078	0.149	0.213	0.217
Spontaneous magnetisation (emu/g)	–	0.1225	–	–

composition $x = 0.025$ has an abrupt ferromagnetic switching with a magnetisation of nearly 0.5 emu/g under a modest applied coercive field of nearly 149 Oe. This may result in a magnetic field-assisted conductivity phenomenon with sensor applications [37]. ESR analysis and peak search analysis from MEM confirm interstitial charges, as tabulated in Table 3. The peak search analysis at $x = 0.075$ reveals a maximum interstitial charge in the Ni^{2+} composition, confirming the presence of Ni^{2+} interstitial ions on the regular lattice from the ESR analysis. When more Ni^{2+} ions are added to the Sn^{4+} host lattice, the interstitial charges go up. This charge has a big effect on the magnetisation.

Table 3. Refined parameters of Rietveld refinement using Unit cell, JANA2006, MEM and peak search analysis.

Parameters		$x = 0.025$	$x = 0.05$	$x = 0.075$
JANA2006				
No. of electrons in unit cell (F_{000})		130.69	126.46	126
Cell constants (Rietveld) (Å)		a, b = 4.744(2) c = 3.190(1)	a, b = 4.749(5) c = 3.192(1)	a, b = 4.748(3) c = 3.194(7)
Volume (Å^3)		71.7926	71.9891	72.0039
X-ray Density (g/cm^3)		6.887	6.600	6.588
Atomic position (O)		x = y = 0.306	x = y = 0.299	x = y = 0.305
B_{iso}(Å^2) (Sn)		0.0316	0.0699	0.0984
B_{iso}(Å^2) (Ni)		0.8284	0.6096	0.5260
B_{iso}(Å^2) (O)		1.2621	1.3943	1.4376
Composition (Rietveld)	expected	$Sn_{0.975}Ni_{0.025}O_2$	$Sn_{0.95}Ni_{0.05}O_2$	$Sn_{0.925}Ni_{0.075}O_2$
	observed	$Sn_{0.966}Ni_{0.035}O_{2.012}$	$Sn_{0.906}Ni_{0.06}O_{2.011}$	$Sn_{0.884}Ni_{0.098}O_{2.008}$
Deficiency (cation)		2.23%	6.91%	7.07%
MEM				
No. of cycles		343	305	497
No. of voxels/Unit cell		1769472	1769472	1769472
Prior density (e/Å^3)	F_{000}/V	1.8202	1.7947	1.7437
Lagrange parameter	$\boldsymbol{\lambda}$	0.0046	0.0041	0.0025
Reliability index	R_{MEM} (%)	1.12	3.10	1.45
Weighted reliability index	wR_{MEM} (%)	1.45	2.72	1.65
MEM Peak Search analysis				
Total charges in unit cell		130.69	126.46	126
Integrated Charges at Sn/Ni site		91.199	85.919	75.838
Integrated Charges at O site		36.394	32.007	34.489
Total charges at regular lattice sites		127.593	117.926	110.327
Integrated charges at interstitial		3.0961	8.534	15.673
% of charges at regular lattice sites	%	97.63	93.25	87.56
% of charges at interstitial region	%	2.369	6.74	12.43

3.1.6. Electron spin resonance spectroscopy

The paramagnetic substance absorbs the frequency of the microwave region (0.04–25 centimetres) in electron spin resonance spectroscopy, causing a transition between magnetic energy levels with unpaired spin. Atoms, molecules, and ions containing an odd number of electrons manifest magnetic properties. An electron has a spin, which causes a magnetic moment. Figure 7 displays the ESR spectra of Ni-doped SnO_2 at room temperature for different compositions ($x = 0.025$, 0.05, and 0.075) along with the g factor values that go with them. The ESR spectral simulations reveal the presence of two different paramagnetic species, Ni^{2+} interstitial and Ni^{2+} substitutional. R. Nagata [38] studied the nickel ions in TiO_2, observing three types of ESR centres originating from the Ni ions: substitutional Ni^{2+} ions, interstitial Ni^{2+} ions, and interstitial Ni^{3+} ions.

The effective g factor values are used to determine the oxidation states of the ions. ESR spectra of Ni^{2+}-doped SnO_2 absorption at the g factor between 2.307 and 2.429 as the g perpendicular factor and the g parallel at 1.141 as an interstitial factor. Higher doping concentrations of Ni^{2+}, exceeding 2.5%, lead to an increase in substitutional magnetisation, which then cancels with the interstitial Ni^{2+} site, thereby destroying the ferromagnetic behaviour. [39]. Furthermore, the ESR spectra of the sample do not identify the presence of Ni^{3+}, as it falls within the g factor range of 4.78–6.12. This confirms the presence of only Ni^{2+} ions in the prepared samples, which is in accordance with XRD peak shift results.

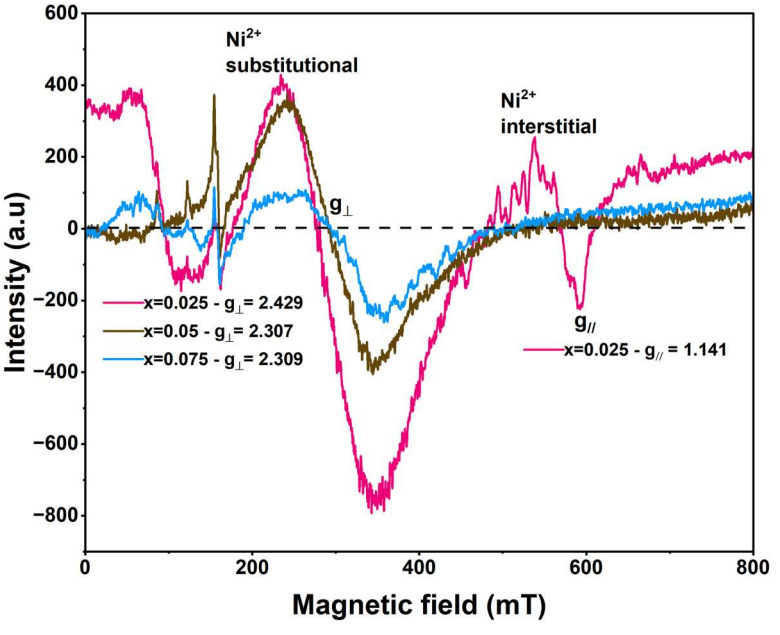

Figure 7. ESR spectra of (2.5%, 5% and 7.5%) Ni doped SnO_2 samples show the presence of both substitutional and interstitial Ni^{2+} ions.

3.4. Computational techniques

3.4.1. Structural refinement

The Rietveld refinement procedure for profile fitting using JANA2006 software refined the powder XRD data of $Ni_xSn_{1-x}O_2$ ($x = 0.025$, 0.05, 0.075) samples [24]. Figure 8 depicts the observed and fitted profile of Ni-doped SnO_2 with 2θ and intensity in arbitrary units. It shows a perfect match between the measured and calculated X-ray intensities. It also shows three more impurity peaks, one of which is for orthorhombic SnO_2 (Pbcn [60]) and the other two are for metal Sn (I41/amd [141]). Some authors have already reported these impurity peaks [30]. Higher calcination temperatures above 500°C and transition metal modification are the primary causes of the extra peaks. The model selection and refinement performed flawlessly, as evidenced by the very small reliability indices, wR_p and R_{obs}, close to 7% and the goodness-of-fit value close to one. Supplementary table S1 presents the observed structure factor (F_{obs}) and the calculated structure factor (F_{cal}), as well as the standard error of the observed structure factor (F_{obs}). Table S1 demonstrates that the difference between the observed and calculated structure factor and the standard deviation is negligible, corroborating the refinement procedure's perfection and the crystallographic model's choice. The refinement parameters and refined structural parameters are shown in Table 3. F_{000} is the number of electrons in the unit cell, $B_{iso}(Sn)$ (Å^2) and $B_{iso}(O)$ (Å^2) are the Debye–Waller factors for Sn and O, and these values are close to what has been reported. The total prior density of electrons in the unit cell drops from 130.68 to 125.56 when Ni is added. This means that the low-electrons of Ni ($Z = 28$) moved into the high-electrons of Sn ($Z = 50$). The crystal density decreases as the Ni doping concentration increases, whereas the cell parameters and cell volume do not follow the same behaviour. This is due to the fact that there is a lack of incorporation of Ni^{2+} ions in the regular lattice Sn^{4+} host site; rather, they will be occupying non-regular interstitial sites. Despite the interstitial charge occupancy in all compositions, the composition $x = 0.05$ exhibits a noticeable intensity variation compared to the other two, likely due to the maximum residual charges at the non-regular interstitial sites. The MEM analysis, also discussed in Section 3.2.2, confirms the same result. Table 3 reports a small discrepancy between the expected and observed composition, which leads to the cation deficiency.

The cation deficiency is 2.23% for 2.5% Ni doping, and it significantly increases to 6.91% and 7.07% for 5% and 7.5% Ni doping, respectively. As explained in Section 3.1.3, this cation deficiency directly correlates with the UV-visible absorption intensity, where the SnO_2 and 2.5% Ni-doped systems have the maximum absorption intensity and further Ni-doping decreases. Thermal vibration factors and isotropic Debye–Waller factor obtained by refinement are in accordance with the earlier reports [40].

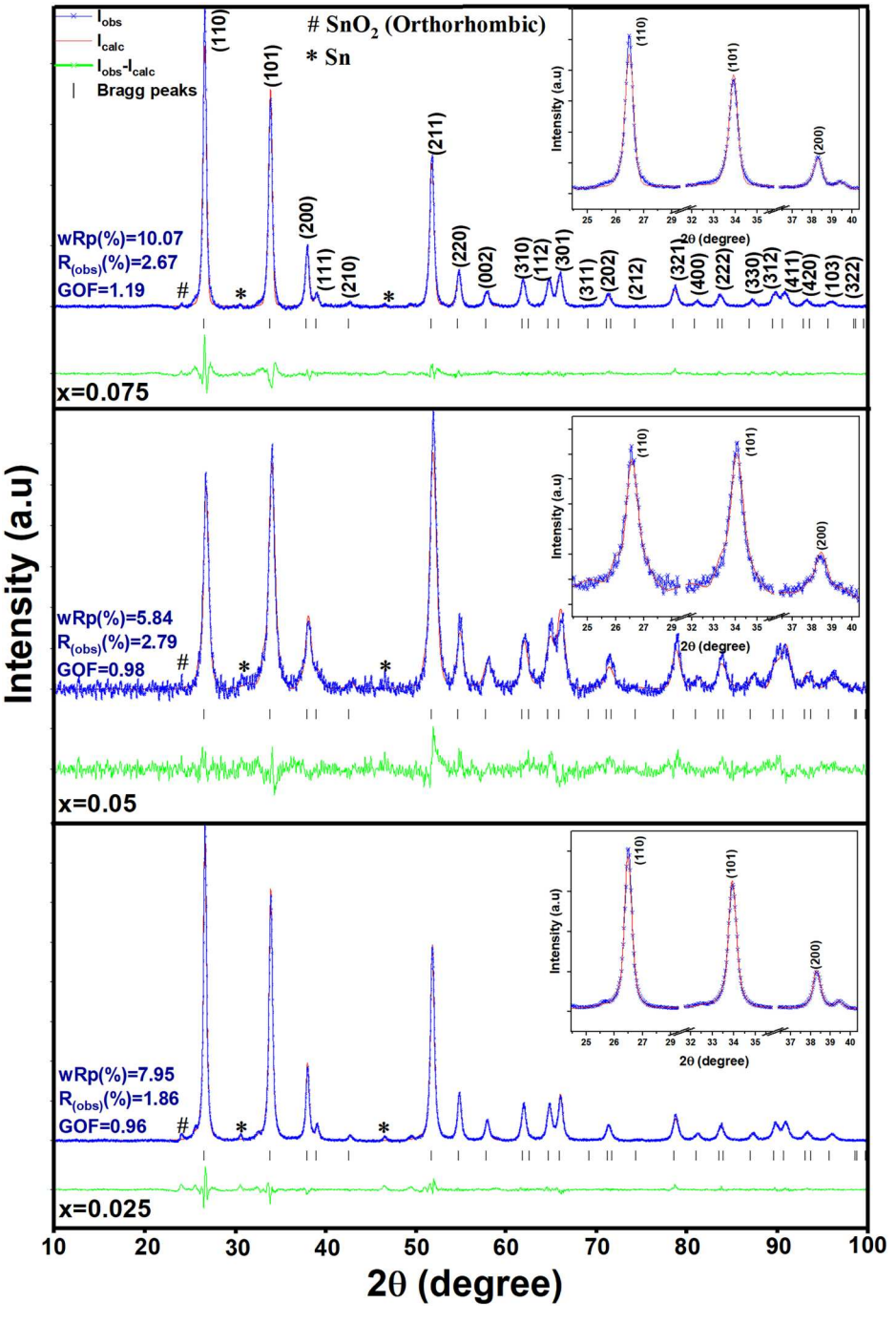

Figure 8. Rietveld refined observed and calculated X-ray intensity profile, showing the perfectness of refinement and the intensity variation seen for the composition $x = 0.05$ due to interstitial charge accumulation. Also, a little impurity phase of orthorhombic SnO2 and transition metal Sn phase is reported.

3.4.2. Charge density in Ni doped SnO_2 using MEM

The meticulous electron density distribution of the structure was obtained using the mathematical tool maximum entropy method (MEM), which maximises the entropy due to the motion of electrons inside the unit cell [41]. MEM can yield highly reliable, accurate, and high-resolution electron density distribution even with a limited number of neutron/X-ray structure factors, as reported by various researchers [42–44]. The key factor for MEM calculations is the zeroth-order single-pixel approximation method with a suitable Lagrangian parameter (λ) for a minimum number of iterations. The software Dysnomia is utilised for MEM calculations [45]. The software VESTA [27] clearly visualises the 3D and 2D distribution of electrons and the bonding nature between ions and atoms. For MEM calculations, the refined structure factor for the Bragg peaks and the structural parameters from the JANA-based Rietveld refinement are used as inputs. The unit cell is divided into $(128 \times 128 \times 108)$ voxels for refinement, and all voxels are filled with uniform prior electron densities of 1.8202, 1.7947, and 1.7437 e/Å^3, respectively, for 2.5%, 5%, and 7.5% Ni doping. The MEM values of weighted reliability indices (wR_{MEM}) for 2.5%, 5%, and 7.5% Ni doping are very low, 1.45%, 2.66%, and 1.63%, respectively, which indicate the perfectness of MEM refinement.

In Figure 9, 3D MEM electron density mapping with an iso surface level of 1.05 e/Å^3 is shown. Six oxygen ions surround the body-centered Ni-doped Sn ion inside the unit cell, with two in the apical position and four in the equatorial position. 3D diagrams reveal complete differences in the nature and strength of (Sn/Ni-O) bonding in apical and equatorial positions across all Ni compositions. The skewness of oxygen ions is more prominent in apical bonding than in equatorial bonding, and it reaches its peak at the 7.5% Ni doping composition, indicating a highly covalent nature. This skewness may be due to the anharmonic thermal vibration of the oxygen ions. Both Sn and O ions show the anisotropy of the electron density distribution. Because electrons are not

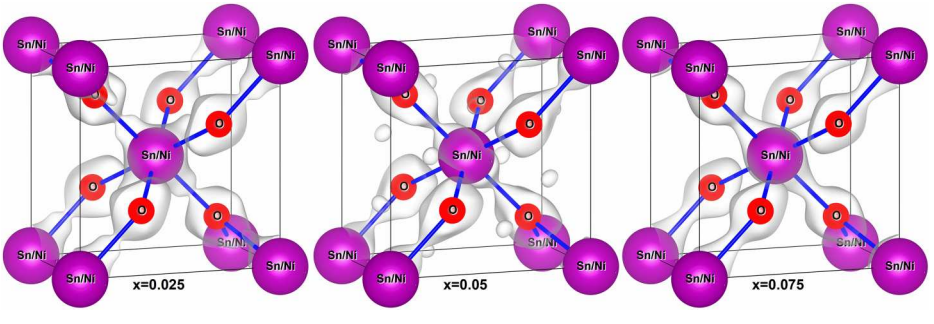

Figure 9. 3D MEM electron density distribution with different Ni doping with the iso surface level 1.05 e/Å^3, showing the distinct apical and equatorial bond density, residual charges at the interstitial positions, other than regular Sn lattice dopant site.

distributed evenly, the electronic polarisation effects are different for O-Sn/Ni-O ions at the apex and equatorial points. Furthermore, the 5% Ni composition clearly shows the interstitial charge accumulation. Figures 10 and 11 (a–c) show the 2D MEM electron density visualisation along the (001) and (110) lattice planes with contour levels (0–1.2 e/Å^3) and intervals of 0.05 e/Å^3. The 1D radial electron density profile in Figure 12 (a–d) shows the Sn/Ni-O apical, (b) Sn/Ni-O equatorial, (c) O-O, and (d) Sn/Ni-Sn/Ni critical bond density regions of different Ni compositions. The combined discussion of both 2D and 1D numerical electron densities between interaction ions will yield fruitful results. The 2D electron density in the (001) plane shows O-O interaction. The O-O bond critical point (BCP) electron density will be maximum for the composition 2.5%, minimum for the composition 5%, and 7.5% for Ni doping. Additionally, the total energy density (shown in the table inside Figure 12(c)) is highest for the 7.5% Ni mixture and moderately low for the 2.5% Ni mixture. It is higher for the 5% sample. Both the results confirm the maximum and moderate polar covalency in the 7.5% and 2.5% samples, respectively, as well as the highly ionic-bonded nature in the 5% sample. The dominant tongue-like electron density for the 5% composition confirms the maximum non-regular interstitial charge accumulation, which is the minimum for other compositions.

The apical and equatorial (Sn/Ni-O) bonding can be seen in Figure 11 (a–c), which shows the 2D visualisation of electron density along with 1D numerical values embedded across the (1 1 0) plane. All samples exhibit a dominant and gradual increase in the apical (Sn/Ni-O) covalent nature, reaching its maximum covalency at 7.5% Ni doping. 7.5% Ni doping. The total energy density values at BCP from the table embedded in Figure 12 (a) back up the above argument, with a value as low as – 7.5% Ni showing the highest level of covalency. Another value that fits with the maximum oxygen atomic displacement shown in Table 3 is 1.001 Å, which is a relatively lower value for the 5% Ni composition. It's clear that the equatorial (Sn/Ni-O) bonding has a moderate

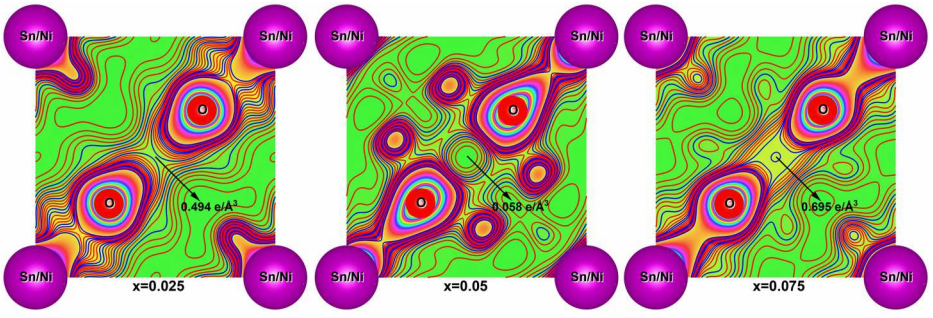

Figure 10. Distribution of 2D MEM electron density along the (001) plane with contour level (0–1.2 e/Å^3) and interval 0.05 e/Å^3. Embedded are the numerical O-O mid-bond electron density values. The accumulation of interstitial charge is observed for the composition $x = 0.05$.

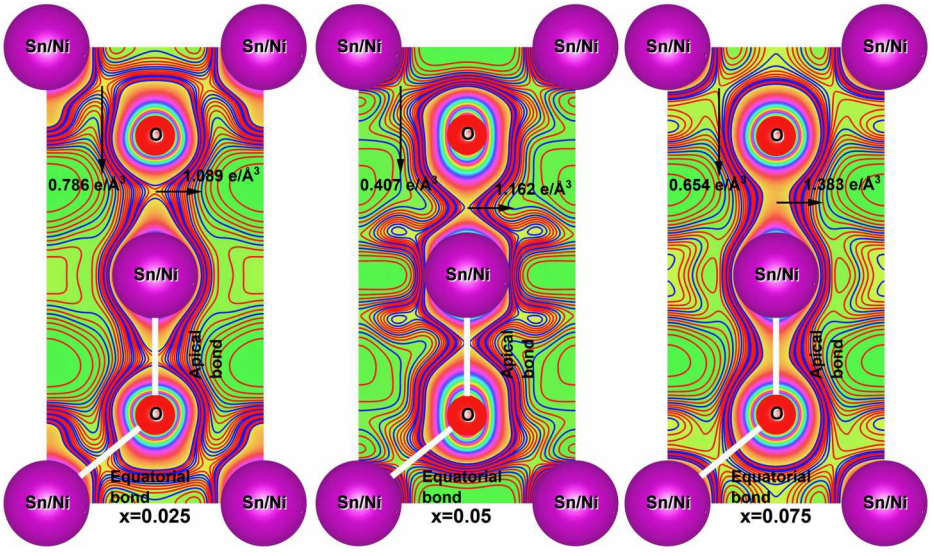

Figure 11. The 2D MEM electron density distribution for the (110) plane of $Ni_xSn_{1-x}O_2$ ($x = 0.025, 0.05, 0.075$) reveals the apical and equatorial Sn/Ni – O bonding, as well as a shift in the bond critical point. Bonding visualisations demonstrate maximal apical covalent bonding in the $x = 0.075$ sample.

covalent nature because it has the highest negative total energy density at the BCP value (−14.072 eV/Å^3) and the highest electron density value (0.786 e/Å^3). The electron density is the lowest (0.407 e/Å^3) and the total positive energy density is the highest (7.415 eV/Å^3) at BCP for the 5% Ni composition. This shows that the electrons are grouped together, which leads to pure ionic bonding. The dominant interstitial charge accumulation for the 5% Ni composition is also visible in the (110) plane. The (Sn/Ni – Sn/Ni) BCP electron density for all compositions is very small (nearly 0.05 e/Å3), and the total energy density is a small positive value (nearly 1.3 eV/Å^3) and almost similar for all compositions. Due to the extension of spatial charges between the ions, 2.5% Ni doping in SnO_2 (Sn/Ni-O) displays polar covalent bonding. While incorporating Ni in the SnO_2 system, for 2.5%, the Ni occupancy is found to be higher on the regular lattice Sn sites, revealing a good dilution level of Ni in SnO_2. When the doping level is increased to 5% of Ni, there is a complete change in the electronic structure due to the interstitial occupancy of much of the Ni/Sn ions, leading to defect chemistry by introducing defect like oxygen vacancy, oxygen and tin interstitial, oxygen and nickel interstitial, substitutional Ni ions with oxygen hole and pair of Ni ions with peroxide ion. Thus, higher number of oxygen vacancies will be introduced due to increased doping. If two Sn^{4+} ions are replaced by two Ni^{2+} ions together with O^{2-} vacancy, the two oxygen vacancies associated with 3d dopants would be expected to trap the electrons. This defect chemistry is responsible for increase

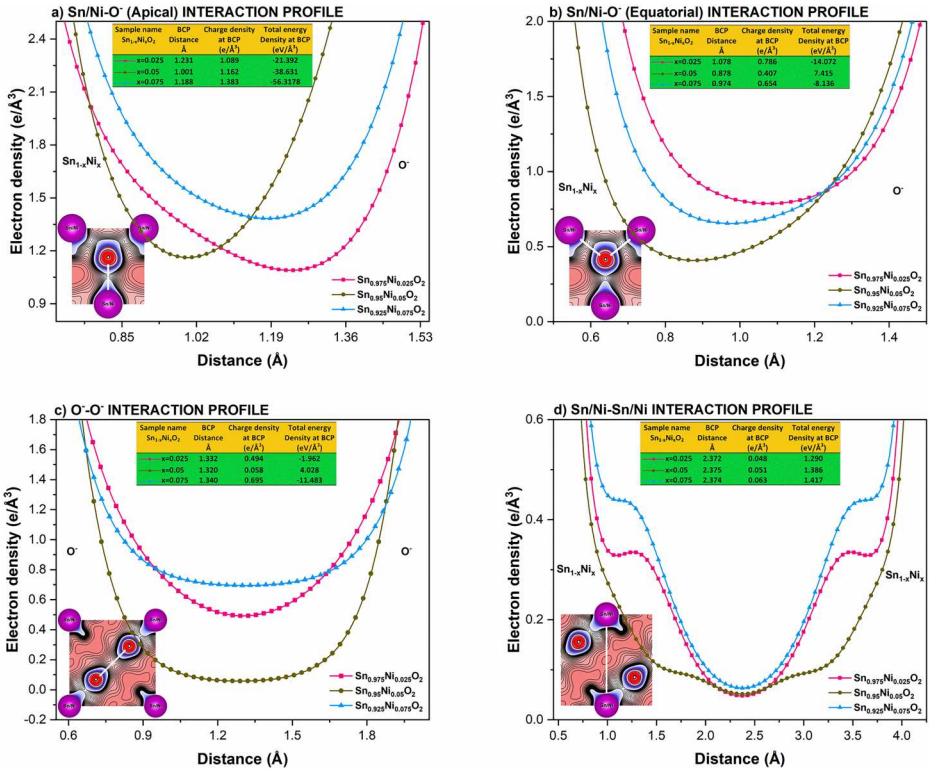

Figure 12. (a–d) 1D MEM electron density distribution of $Ni_xSn_{1-x}O_2$ with $x = 0.025$, 0.05, and 0.075, along with an inset table displaying bond critical point (BCP) distance, electron density, and total energy density at BCP. (a) The Sn/Ni-O apical interaction profile has electron density at BCP favourable of covalent bonding; (b) The Sn/Ni-O equatorial interaction profile has a decreasing electron density trend with Ni doping showing covalent to ionic transformation; (c) O-O and (d) Sn/Fe-Sn/Fe interaction profiles showing ionic interactions.

in electrical conductivity behaviour and diminishing magnetic properties as the defects due to more doping are likely to be electronic in nature rather than interstitial/vacancies.

3.4.3. Pair distribution function study

The pair distribution function (PDF) can be used to look at the local structure with XRD data in real space. It does this by using total scattering data that includes both Bragg peaks and diffuse scattering [46]. It provides useful parameters in a doped system, such as the nearest neighbour distance (first, second, third, etc.), number density, and average crystallite size. The software PdfgetX converts the experimental X-ray intensity data into a pair distribution function, while PDFgui performs the observed and calculated profile fitting. Figure 13(a–c) illustrates the Pair distribution function analysis (PDF) using experimental XRD data. The PDF profile that was fitted and observed is shown in Figure 13 (a, b). The y-axis is G(r), and the *x*-axis is the radial distance

from a reference atom r(Å). The bond length distribution of the SnO_2 system is also shown. Figure 13 (c) displays the long-range order profile fitting, revealing crystallite sizes of 15, 9, and 17 nm for 2.5%, 5%, and 7.5% Ni-doped systems, respectively.

The observed crystallite sizes are comparable to those estimated by the Scherrer method. The weighted reliability index R_w is 13.25%, 18.65%, and 10.88% for $Ni_xSn_{1-x}O_2$ ($x = 0.025$, 0.05, 0.075), respectively, with a Q maximum of 6.94 $Å^{-1}$. The first nearest neighbour distance turns out to be 1.965, 1.942, and 1.946 Å, respectively, for 2.5%, 5%, and 7.5% Ni doping compositions. The different Ni doping concentrations at the observed nearest neighbour distances result in a small SnO_6 octahedron distortion. For the 2.5% Ni-doped sample, the PDF bond search analysis shows only the crystallographic structural bonds corresponding to rutile tetragonal SnO_2. The other two samples have some additional bonds besides the structure leading to interstitial charge accumulation, as discussed by the Rietveld and MEM methods.

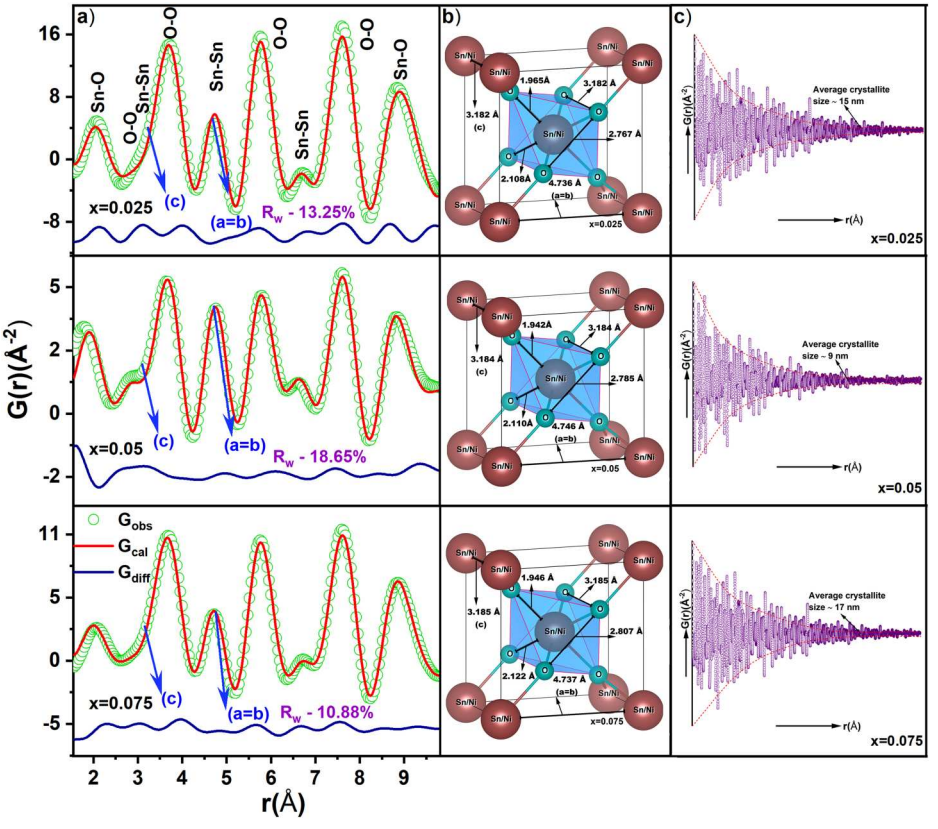

Figure 13. (a–c) Pair distribution function analysis using experimental XRD data; (a) Fitted observed and calculated PDF for $Ni_xSn_{1-x}O_2$ ($x = 0.025.0.05$, 0.075); (b) The calculated bonding length from PDF; (c) Crystallite size from observed peaks.

The cell parameters show a slight increase in the unit cell's volume, indicating Ni doping-induced unit cell expansion.

4. Conclusion

A straightforward, one-step chemical precipitation method was used to synthesise diluted compositions of Ni^{2+}-doped SnO_2 magnetic semiconductors with a rutile tetragonal structure. Electron spin resonance (ESR) investigations confirmed the presence of Ni^{2+} in all synthesised compositions. The absence of a peak shift implies complete Ni^{2+} doping, possibly in the host or interstitial lattice sites. Unlike previous findings, the optical analysis reveals that an increase in Ni doping leads to a widening of the energy band gap from 3.51 eV to 4.09 eV and a decrease in the optical absorbance. In photoluminescence studies, the introduction of Ni^{2+} results in the generation of excess oxygen, leading to the emission of red light. A magnetic study at room temperature reveals a transition from diamagnetism to soft ferromagnetism, characterised by a magnetisation of 0.5 emu/g and a coercivity of 150 Oe as a result of the introduction of 2.5% Ni doping in pure SnO_2. The introduction of more Ni doping leads to a decrease in magnetisation and paramagnetism. Both Rietveld and MEM techniques reveal that 2.5% doping causes the Sn^{4+} host site to experience the most dilution of Ni^{2+} ions. Additional doping causes interstitial charge buildup, defect appearance, and reduced magnetisation. It establishes an empirical relationship between magnetism and the electronic structure of MEM. The key findings for achieving saturation magnetisation are the proper dilution of Ni^{2+} ions in the Sn^{4+} host lattice without interstitial charge buildup, and the strong covalency of Sn/Fe-O bonds in both apical and equatorial positions. In SnO_2 semiconductors, dilute Ni-doping will enhance soft ferromagnetism and optical band tuning.

5. Data transparency

The authors declare that all data supporting the findings of this study will be made available under request.

Acknowledgments

The researchers thank the Nanotechnology Research Centre (NRC), SRMIST, for VSM analysis, Heber Analytical Instrumentation Facility, Bishop Heber College, Trichy, for providing the research facilities for UV-Visible and photoluminescence spectrophotometry studies, SAIF, Indian Institute of Technology Madras, for ESR analysis, and STIC, Cochin for powder XRD and the Instrumental Facilities, CIC, Madurai Kamaraj University, for TEM.

Disclosure statement

No potential conflict of interest was reported by the author(s).

Funding

This research did not receive any specific grant from funding agencies in the public, commercial, or not-for-profit sectors.

Author contributions

K. KaviyaPandimeena: Investigation, writing the original draft, executing graphical techniques **M. Charles Robert**: Supervision, Conceptualisation, Methodology, **N. Pavithra**: Data Curation, formal analysis, **Y. B. Kannan** for electronic artwork and editing and **P. Christuraj** for Resources.

ORCID

K. KaviyaPandimeena http://orcid.org/0009-0003-3642-9191
M. Charles Robert http://orcid.org/0000-0001-9339-1933

References

[1] D.J. Heinzen, R.H. Wynar, P.D. Kheruntsyan, P.D. Drummond, T. Dietl, H. Ohno, F. Matsukura, J. Cibert, and D. Ferrand, *Zener model description of ferromagnetism in zinc-blende magnetic semiconductors downloaded from*. Chem. Phys. Lett 269 (1995), pp. 2657. doi:10.1126/science.287.5455.1019.

[2] Y. Matsumoto, M. Murakami, T. Shono, T. Hasegawa, T. Fukumura, M. Kawasaki, P. Ahmet, T. Chikyow, S.Y. Koshihara, and H. Koinuma, *Room-temperature ferromagnetism in transparent transition metal-doped titanium dioxide*. Science 291 (2001), pp. 854–856. doi:10.1126/science.1056186.

[3] C.B. Fitzgerald, M. Venkatesan, A.P. Douvalis, S. Huber, J.M.D. Coey, T. Bakas, *SnO 2 doped with Mn, Fe or Co : room temperature dilute magnetic semiconductors*. J. Appl. Phys. 95 (2011), pp. 7390–7392. doi:10.1063/1.1676026.

[4] Y.M. Hao, S.Y. Lou, S.M. Zhou, R.J. Yuan, G.Y. Zhu, and N. Li, *Structural, optical, and magnetic studies of manganese-doped zinc oxide hierarchical microspheres by self-assembly of nanoparticles*. Nanoscale Res. Lett 7 (2012), pp. 19–21. doi:10.1186/1556-276X-7-100.

[5] N.H. Hong, *Ferromagnetism in transition-metal-doped semiconducting oxide thin films*. J. Magn. Magn. Mater 303 (2006), pp. 338–343. doi:10.1016/j.jmmm.2006.01.067.

[6] B.N. Suresh, B.S.V. Reddy, R.G. Gloridoss, and A.S. Rajendiran, *Production performance of layer chicken fed diets containing sugarcane press residue*. Anim. Nutr. Feed Technol 12 (2012), pp. 257–263. doi:10.5829/idosi.ijee.2013.04.01.

[7] W. Prellier, A. Fouchet, and B. Mercey, *Oxide-diluted magnetic semiconductors: a review of the experimental status*. J. Phys. Condens. Matter 15 (2003), pp. 1583. doi:10.1088/0953-8984/15/37/R01.

[8] Y. Gao, Q. Hou, and Q. Liu, *First-principles study on the electronic structures and magneto-optical properties of Fe2+/3+ doped SnO2*. Solid State Commun. 305 (2020), pp. 113764. doi:10.1016/j.ssc.2019.113764.

[9] A. Hirohata, K. Yamada, Y. Nakatani, L. Prejbeanu, B. Diény, P. Pirro, and B. Hillebrands, *Review on spintronics: principles and device applications*. J. Magn. Magn. Mater 509 (2020), pp. 166711. doi:10.1016/j.jmmm.2020.166711.

[10] X.L. Wang, Z.X. Dai, and Z. Zeng, *Search for ferromagnetism in SnO 2 doped with transition metals (V, Mn, Fe, and Co)*. J. Phys.: Condens. Matter 20 (2008), pp. 045214. doi:10.1088/0953-8984/20/04/045214.

[11] P.P. Dorneanu, A. Airinei, M. Grigoras, N. Fifere, L. Sacarescu, N. Lupu, and L. Stoleriu, *Structural, optical and magnetic properties of Ni doped SnO2 nanoparticles*. J. Alloys Compd 668 (2016), pp. 65–72. doi:10.1016/j.jallcom.2016.01.183.

[12] S. Rani, S.C. Roy, N. Karar, and M.C. Bhatnagar, *Structure, microstructure and photoluminescence properties of Fe doped SnO2 thin films*. Solid State Commun. 141 (2007), pp. 214–218. doi:10.1016/j.ssc.2006.10.036.

[13] P.V. Jithin, K. Sudheendran, K.J. Sankaran, and J. Kurian, *Influence of Fe-doping on the structural and photoluminescence properties and on the band-gap narrowing of SnO2 nanoparticles*. Opt. Mater. (Amst) 120 (2021), pp. 111367. doi:10.1016/j.optmat.2021.111367.

[14] S. Kumar, *Exploration of structural, morphological and magnetic properties of transition metal doped SnO2 films grown using pulsed laser deposition*. Vacuum 182 (2020), pp. 109725. doi:10.1016/j.vacuum.2020.109725.

[15] J. Divya, A. Pramothkumar, S. Joshua Gnanamuthu, D.C. Bernice Victoria, and P.C. Jobe prabakar, *Structural, optical, electrical and magnetic properties of Cu and Ni doped SnO2 nanoparticles prepared via Co-precipitation approach*. Phys. B Condens. Matter 588 (2020), pp. 412169. doi:10.1016/j.physb.2020.412169.

[16] S. Asaithambi, P. Sakthivel, M. Karuppaiah, G.U. Sankar, and K. Balamurugan, *Investigation of electrochemical properties of various transition metals doped SnO 2 spherical nanostructures for supercapacitor applications*. J. Energy Storage 31 (2020), pp. 101530. doi:10.1016/j.est.2020.101530.

[17] V. Agrahari, M.C. Mathpal, M. Kumar, and A. Agarwal, *Investigations of optoelectronic properties in DMS SnO2 nanoparticles*. J. Alloys Compd 622 (2015), pp. 48–53. doi:10.1016/j.jallcom.2014.10.009.

[18] C. Van Komen, A. Thurber, K.M. Reddy, J. Hays, and A. Punnoose, *Structure-magnetic property relationship in transition metal (M = V,Cr,Mn,Fe,Co,Ni) doped SnO2 nanoparticles*. J. Appl. Phys 103 (2008), pp. 2006–2009. doi:10.1063/1.2836797.

[19] R. Thamiz Selvi, M. Nallaiyan, S. Nisha, S. Sagadevan, F. Mohammad, K. Sadaiyandi, K. Pradeev Raj, L. Ashokkumar, M.B. Latha, and J.A. Lett, *Comparative studies on structural, optical, and biological properties of SnO2 and Ni-doped SnO2 nanocrystals*. Mater. Res. Express 6 (2019), pp. 101530. doi:10.1088/2053-1591/ab5fa3.

[20] M. Venkatesan, R.D. Gunning, P. Stamenov, and J.M.D. Coey, *Room temperature ferromagnetism in Mn- and Fe-doped indium tin oxide thin films*. J. Appl. Phys 103 (2008), pp. 1–4. doi:10.1063/1.2835476.

[21] Z.M. Tian, S.L. Yuan, J.H. He, P. Li, S.Q. Zhang, C.H. Wang, Y.Q. Wang, S.Y. Yin, and L. Liu, *Structure and magnetic properties in Mn doped SnO2 nanoparticles synthesized by chemical co-precipitation method*. J. Alloys Compd 466 (2008), pp. 26–30. doi:10.1016/j.jallcom.2007.11.054.

[22] A.S. Ahmed, M. Shafeeq, M.L. Singla, S. Tabassum, A.H. Naqvi, and A. Azam, *Band gap narrowing and fluorescence properties of nickel doped SnO 2 nanoparticles*. J. Lumin 131 (2011), pp. 1–6. doi:10.1016/j.jlumin.2010.07.017.

[23] K.K. Pandimeena, M.C. Robert, and S. Saravanakumar, *Energy gap tuning, ferromagnetic switching, visualization of electron density and bonding in dilute magnetic semiconductor Fe-doped SnO2*. Optik (Stuttg) 287 (2023), pp. 171091. doi:10.1016/j.ijleo.2023.171091.

[24] H.M. Rietveld, *A profile refinement method for nuclear and magnetic structures*. J. Appl. Crystallogr 2 (1969), pp. 65–71. doi:10.1107/S0021889869006558.

[25] S. Saravanakumar, M.J. Priya, and R. Saravanan, *Synthesis and electron density analysis of SnO2 nano particles*. Mater. Sci. Forum 671 (2011), pp. 121–129. doi:10.4028/www.scientific.net/MSF.671.121.

[26] K. Momma, T. Ikeda, A.A. Belik, and F. Izumi, *Dysnomia, a computer program for maximum-entropy method (MEM) analysis and its performance in the MEM-based pattern fitting*. Powder Diffr. 28 (2013), pp. 184–193. doi:10.1017/S088571561300002X.

[27] K. Momma and F. Izumi, *VESTA: a three-dimensional visualization system for electronic and structural analysis*. Urn:Issn:0021-8898 41 (2008), pp. 653–658. doi:10.1107/S0021889808012016.

[28] S. Brühne, E. Uhrig, K.D. Luther, W. Assmus, M. Brunelli, A.S. Masadeh, and S.J.L. Billinge, *PDF from X-ray powder diffraction for nanometer-scale atomic structure analysis of quasicrystalline alloys*. Zeitschrift Fur Krist 220 (2005), pp. 962–967. doi:10.1524/zkri.2005.220.11_2005.962.

[29] C.L. Farrow, P. Juhas, J.W. Liu, D. Bryndin, E.S. Boin, J. Bloch, T. Proffen, and S.J.L. Billinge, *PDFfit2 and PDFgui: Computer programs for studying nanostructure in crystals*. J. Phys. Condens. Matter 19 (2007), pp. 335219. doi:10.1088/0953-8984/19/33/335219.

[30] M.H. Carvalho, E.C. Pereira, and A.J.A. De Oliveira, *Orthorhombic SnO2 phase observed composite (Sn1-: XCex)O2 synthesized by sol-gel route*. RSC Adv. 8 (2018), pp. 3958–3963. doi:10.1039/c7ra12727 h.

[31] H. Search, C. Journals, A. Contact, M. Iopscience, and I.P. Address, *On the determination of lattice parameters by the debye-scherrer method*. Proceed Phys Soc 126 (1945).

[32] D. Nath, F. Singh, and R. Das, *X-ray diffraction analysis by Williamson-Hall, Halder-Wagner and size-strain plot methods of CdSe nanoparticles- a comparative study*. Mater. Chem. Phys 239 (2020), pp. 122021. doi:10.1016/j.matchemphys.2019.122021.

[33] I.N. Bhatti, *Effect of annealing and time of crystallization on structural and optical properties of PVDF thin film using acetone as solvent*. IOSR J. Appl. Phys 4 (2013), pp. 42–47. doi:10.9790/4861-0444247.

[34] F. Jiang, L. Peng, and T. Liu, *Ni-Doped SnO2 dilute magnetic semiconductors: morphological characteristics and optical and magnetic properties*. J. Supercond. Nov. Magn 33 (2020), pp. 3051–3058. doi:10.1007/s10948-020-05533-y.

[35] R.F. Pierret, *Semiconductor Device Fundamental*, ADDISON-WESLEY PUBLISHING COMPANY, Boston, United States of America, 1996.

[36] K. Vanheusden, W.L. Warren, C.H. Seager, D.R. Tallant, J.A. Voigt, and B.E. Gnade, *Mechanisms behind green photoluminescence in ZnO phosphor powders*. J. Appl. Phys 79 (1996), pp. 7983–7990. doi:10.1063/1.362349.

[37] V. Guarino, V. Iannotti, G. Ausanio, L. Ambrosio, and L. Lanotte, *Elastomagnetic nanofiber wires by magnetic field assisted electrospinning*. Express Polym. Lett 13 (2019), pp. 419–428. doi:10.3144/expresspolymlett.2019.35.

[38] R. Nakata, *ESR study of SnO2 doped with nikel ions*. J. Phys. Soc. Japan 66 (1974), pp. 694–700. doi:10.1143/JPSJ.37.694.

[39] S.K. Misra, S.I. Andronenko, M.H. Engelhard, A. Thurber, K.M. Reddy, and A. Punnoose, *Role of dopant incorporation on the magnetic properties of Ce 1-xNixO2 nanoparticles: an electron paramagnetic resonance study*. J. Appl. Phys 103 (2008), pp. 1–4. doi:10.1063/1.2833291.

[40] T. Yamanaka, R. Kurashima, and J. Mimaki, *X-ray diffraction study of bond character of rutile-type SiO2, GeO2 and SnO2*. Zeitschrift Fur Krist 215 (2000), pp. 424–428. doi:10.1524/zkri.2000.215.7.424.

[41] R. Saravanan, Y. Ono, M. Isshiki, K. Ohno, and T. Kajitani, *Electron density distribution in GaAs using MEM*. J. Phys. Chem. Solids 64 (2003), pp. 51–58. doi:10.1016/S0022-3697(02)00209-3.

[42] M. Thavarani, M.C. Robert, S.B. Prasath, N. Pavithra, R. Saravanan, and S. Saravanakumar, *Room temperature magnetism and experimental electron density analysis of Co2+ Doped ZnFe2O4 spinel nanoferrites*. J. Electron. Mater 51 (2022), pp. 3078–3091. doi:10.1007/s11664-022-09553-3.

[43] M. Thavarani, M.C. Robert, N. Pavithra, S.B. Prasath, Y.B. Kannan, and A.A. Ahamed, *An experimental analysis of the correlation between electronic structure and room temperature magnetism in Cu-doped CoFe2O4 spinel ferrite*. Appl. Phys. A Mater. Sci. Process 128 (2022), pp. 659. doi:10.1007/s00339-022-05808-2.

[44] R. Saravanan, T.K. Thirumalaisamy, and T. Kajitani, *Local structure determination of the nonlinear optical material LiNbO 3 using XRD, Phys*. Status Solidi Appl. Mater. Sci 208 (2011), pp. 2643–2650. doi:10.1002/pssa.201127184.

[45] S. Sasikumar, R. Saravanan, S. Saravanakumar, and M.C. Robert, *Preparation, electronic structure, and chemical bonding of lead-free (1 − x)(K0.5Bi0.5)TiO3-xBaTiO3 solid solution*. Appl. Phys. A Mater. Sci. Process 124 (2018), pp. 31. doi:10.1007/s00339-017-1444-x.

[46] R. Saravanan and M.C. Robert, *Local structure of the thermoelectric material Mg2Si using XRD*. J. Alloys Compd 479 (2009), pp. 26–31. doi:10.1016/j.jallcom.2008.12.117.

Philosophical Magazine

ISSN: 1478-6435 (Print) 1478-6443 (Online) Journal homepage: www.tandfonline.com/journals/tphm20

Study of the boundary migration of recrystallized grains under inhomogeneous deformation field by crystal plasticity – phase field simulation

Qinghe Wei, Lin Yuan, Debin Shan & Bin Guo

To cite this article: Qinghe Wei, Lin Yuan, Debin Shan & Bin Guo (2025) Study of the boundary migration of recrystallized grains under inhomogeneous deformation field by crystal plasticity – phase field simulation, Philosophical Magazine, 105:13, 665-683, DOI: 10.1080/14786435.2025.2449817

To link to this article: https://doi.org/10.1080/14786435.2025.2449817

PHILOSOPHICAL MAGAZINE
2025, VOL. 105, NO. 13, 665–683
https://doi.org/10.1080/14786435.2025.2449817

Taylor & Francis
Taylor & Francis Group

Study of the boundary migration of recrystallized grains under inhomogeneous deformation field by crystal plasticity – phase field simulation

Qinghe Wei[a,b], Lin Yuan[a,b], Debin Shan[a,b] and Bin Guo[a,b]

[a]National Key Laboratory for Precision Hot Processing of Metals, Harbin, People's Republic of China; [b]School of Materials Science and Engineering, Harbin Institute of Technology, Harbin, People's Republic of China

ABSTRACT

In this study, a grain boundary (GB) migration model based on crystal plasticity (CP) and phase field (PF) was constructed for recrystallization of magnesium alloys. The model introduced the stored energy field obtained by CP into the PF simulations, aiming to analyze the effect of the inhomogeneous stored energy generated under the plastic deformation on the GB migration. It was found that the curvature plays a more significant role in the inhomogeneous stored energy field than in the uniform deformation field. Although grains with hard orientation have a lower deformation storage energy, they are still partially swallowed due to mutual influence between GBs near the triple junction. The high energies in the original GBs increase the migration rate at the triple junctions locally for a short period of time, but it is not enough to make a significant difference over extended periods at mesoscopic scales. The simulation results in this study are helpful in explaining the previous experimental observations.

ARTICLE HISTORY
Received 27 March 2024
Accepted 30 December 2024

KEYWORDS
Grain growth; computer simulation; mesoscopic systems; grain boundary engineering; triple junctions; recrystallization

1. Introduction

Grain growth largely dominates the microstructural evolution of polycrystalline metals [1], influencing their service properties through interactions with dislocations at grain boundaries (GBs) [2,3]. The migration behaviour of GB is currently one of the important topics in the design of polycrystalline metallic materials [4–6].

In recent years, computer simulations have played an important role in investigating grain growth across various scales. At the atomic level, there are molecular dynamics (MD) simulations based on methods such as mean-curvature flow model [7] and disconnection model [4,8]. At the mesoscopic scale, there are vertex or front-tracking model [9,10], Monte Carlo models

CONTACT Lin Yuan yuanlin@hit.edu.cn P.O. Box 435, No.92 West Dazhi Street, Harbin 150001, Heilongjiang, People's Republic of China

[11,12], level set models [13], and phase-field models (PF). The PF is a typical method for simulating the microstructural evolution of complex morphologies, including phase transitions and recrystallization [14]. Due to its capability to naturally and accurately describe the curvature effects at interfaces, it has been demonstrated and made significant progress in grain growth simulations. The multi-order model proposed by Chen and Yang lays the groundwork for analyzing multigrain systems [15]. It has been adapted for normal grain growth by Fan and Chen [16] and Krill and Chen [17], and extended for anisotropic systematic grain growth by Kazaryan et al. [18]. Moelans et al. has systematically analyzed the quantitative relationships between the parameters of the PF model and the GB energies and mobilities, providing uniform stability and accuracy conditions for the numerical solution [19].

In recent studies, the PF simulations have primarily concentrated on the evolution of GBs in the absence of deformation [5,20]. However, it was demonstrated that local irregularities exist in the deformation microstructure and the motion of the recrystallization boundaries [14,21]. Incorporating such irregularities into simulations helps to match the PF method with the plastic deformation process. Yadav et al. analyzed the boundary migration during recrystallization in a periodic stored energy field [22]. To approach the behaviour of GBs under real deformation fields more accurately, it is effective to introduce a crystal plasticity (CP) model, which can predict the spatial evolution of dislocations within deformed polycrystalline microstructures [23]. It has been reported to be feasible to link the mechanical properties of inhomogeneous materials to static recrystallized grain evolution by combining PF and CP [24,25].

In this paper, the plastic deformation field of polycrystalline magnesium at room temperature was obtained by CP simulation. The boundaries of recrystallized grains were constructed in the vicinity of specific original GBs, and the migration of boundaries near triple junction was simulated using PF. The influences of the original GBs and the inhomogeneous deformation field obtained by plastic loading were mainly investigated. Additionally, the evolution and impact of triple junctions in the stored energy field at mesoscopic scales were analyzed.

2. Method

2.1. Crystal plasticity model

In the absence of thermal expansion, the deformation gradient F on a continuous scale can be represented by elastic and plastic components, and given as:

$$F = F_e F_p \tag{1}$$

where F_e denotes elastic deformation and lattice rotation, and F_p denotes the plastic deformation in unrotated and undeformed crystal lattice.

Their corresponding velocity gradient L can be expressed as:

$$\mathrm{L} = \dot{\mathrm{F}}\mathrm{F}^{-1} = \mathrm{L_e} + \mathrm{L_p} \tag{2}$$

where $\mathrm{L_e}$ and $\mathrm{L_p}$ are the elastic and plastic velocity gradient, respectively.

Based on Rice [26], $\mathrm{L_p}$ is expressed as the sum of the shear contributions:

$$L_p = \sum\nolimits_{a=1}^{N_s} \dot{\gamma}^{\alpha} m^{\alpha} \otimes n^{\alpha} + \sum\nolimits_{\beta=1}^{N_{tw}} \dot{\gamma}^{\beta} m^{\beta} \otimes n^{\beta} \tag{3}$$

where superscript α and β are the slip and twin modes respectively; $\mathrm{m}^{\alpha}(\mathrm{m}^{\beta})$ is the unit vectors describing the slip or twin direction; $\mathrm{n}^{\alpha}(\mathrm{n}^{\beta})$ is the respective plane normal; $\dot{\gamma}$ is the shear rate; $N_s(N_{tw})$ is the total number of the slip or twin systems.

The resolved shear stress τ of the slip or twin systems is expressed as:

$$\tau = F_e^T F_e S \cdot (m \otimes n) \tag{4}$$

where S is the material state variable.

The generalised Hooke's law is used in the elastic deformation, while the plasticity law is adopted from the phenomenological crystal plasticity model [27], which applies to the slip and twinning of all crystal structures. The models used are summarised here for the completeness of the research methodology. The Düsseldorf Advanced Material Simulation Kit (DAMASK) [23] is used to implement the crystal plasticity simulations.

The resistance evolution on slip and twin systems is given as:

$$\dot{\xi}^{\alpha} = h_0^{s-s}(1 + c_1(f_{tw}^{tot})^{c_2}(1 + h_{int}^{\alpha}) \times \sum_{\alpha'=1}^{N_s} |\dot{\gamma}^{\alpha'}| \left| 1 - \frac{\xi^{\alpha'}}{\xi_{\infty}^{\alpha'}} \right|^{\alpha} sgn\left(1 - \frac{\xi^{\alpha'}}{\xi_{\infty}^{\alpha'}}\right) h^{\alpha\alpha'} + \sum_{\beta'=1}^{N_{tw}} \dot{\gamma}^{\beta'} h^{\alpha\beta'} \tag{5}$$

$$\dot{\xi}^{\beta} = h_0^{tw-s}\left(\sum_{\alpha=1}^{N_s} |\gamma^{\alpha}|\right)^{c_3} \sum_{\alpha'=1}^{N_s} |\dot{\gamma}^{\alpha'}| h^{\beta\alpha'} + h_0^{tw-tw}(f_{tw}^{tot})^{c_4} \sum_{\beta'=1}^{N_{tw}} \dot{\gamma}^{\beta'} h^{\beta\beta'} \tag{6}$$

where h is the slip-slip and slip-twin interaction matrix, the $\mathrm{h_0^{s-s}}$, $\mathrm{h_0^{tw-s}}$, $\mathrm{h_0^{tw-tw}}$, $\mathrm{h_{int}}$, $\mathrm{c_1}$, $\mathrm{c_2}$, $\mathrm{c_3}$ and $\mathrm{c_4}$ are model fitting parameters, ξ_{∞} is bounding the resistance evolution, and $\mathrm{f_{tw}^{tot}}$ is the total twin volume fraction, denoted as:

$$\mathrm{f_{tw}^{tot}} = \max\left(\sum_{\beta=1}^{\mathrm{N_{tw}}} \gamma^{\beta}/\gamma_{\mathrm{char}}^{\beta},\ 1.0\right) \tag{7}$$

where $\gamma_{\mathrm{char}}^{\beta}$ is the characteristic shear of the twin system β.

The shear rates for slip and twin systems are calculated as follows:

$$\dot{\gamma}^{\alpha} = (1 - f_{tw}^{tot})\dot{\gamma}_0^{\alpha}\left|\frac{\tau^{\alpha}}{\xi^{\alpha}}\right|^{n} \mathrm{Sgn}(\tau^{\alpha}) \tag{8}$$

$$\dot{\gamma}^{\beta} = (1 - f_{tw}^{tot})\dot{\gamma}_0^{\beta}\left|\frac{\tau^{\beta}}{\xi^{\beta}}\right|^{n} \mathrm{H}(\tau^{\beta}) \tag{9}$$

where $\dot{\gamma}_0$ represents the reference shear rate, n is the stress exponent, and Sgn and H stand for Symbolic and Heaviside functions, respectively.

2.2. Phase field model

Based on the Ginzburg-Landau equation, the grain structure can be represented by a series of independent phase fields $\eta_1(r, t)$, $\eta_2(r, t)$, $\cdots$, $\eta_p(r, t)$. For the tricrystal model, three PF variables η_{rex}, η_{def1}, η_{def2} are introduced, as given in Equations (10). In the recrystallized grain, deformed grain #1 and deformed grain #2, the corresponding PF variable is 1, and 0 in the other two variables.

$$\frac{\partial \eta_i(r, t)}{\partial t} = -L(\theta, \phi)\frac{\delta F(\eta_{rex}, \eta_{def1}, \eta_{def2})}{\delta \eta_i(r, t)} \tag{10}$$

The free energy equation F is provided by the grain boundary energy F_0 and the deformation stored energy F_s:

$$F = F_0 + F_s \tag{11}$$

With shear deformation obtained from crystal plasticity simulations, the method of Arsenlis and Parks [28] is introduced to calculate the dislocation density, and given as:

$$\rho_{GN(e)}^{\alpha} b = -\nabla\gamma^{\alpha} \cdot m^{\alpha} = -\gamma_{,k}^{\alpha} s_k^{\alpha} \tag{12}$$

$$\rho_{GN(s)}^{\alpha} b = \nabla\gamma^{\alpha} \cdot n^{\alpha} = \gamma_{,k}^{\alpha} n_k^{\alpha} \tag{13}$$

where $\rho_{GN(e)}^{\alpha}$ and $\rho_{GN(s)}^{\alpha}$ are positive geometrically necessary edge dislocations and screw dislocations on the slip system α, respectively, b is the corresponding burgers vector, s^{α} is the unit vector of the slip direction, n^{α} is the unit vector of the slip plane, and $m^{\alpha} = s^{\alpha} \times n^{\alpha}$.

Introducing the plastic free energy $P = 1/2\rho\mu b^2$ (μ is the shear modulus, and ρ is the sum of $\rho_{GN(e)}^{\alpha}$ and $\rho_{GN(s)}^{\alpha}$) [25], the deformation stored energy is expressed as:

$$F_s = P\left(1 - \frac{\eta_{rex}^2}{\eta_{rex}^2 + \eta_{def1}^2 + \eta_{def2}^2}\right) \tag{14}$$

The free energy equation F_0 is used to characterise the grain boundary energies

as described by Moelans [29]:

$$F_0 = \int_V \left[mf_0(\eta_1,\ \eta_2,\ \cdots,\ \eta_p) + \frac{k}{2}\sum_{i=1}^{p}(\nabla\eta_i)^2 \right] dV \tag{15}$$

$$f_0(\eta_1,\ \eta_2,\ \cdots,\ \eta_p) = \sum_{i=1}^{p}\left(\frac{\eta_i^4}{4} - \frac{\eta_i^2}{2}\right) + \sum_{i=1}^{p}\sum_{j>i}^{p}\gamma\eta_i^2\eta_j^2 + \frac{1}{4} \tag{16}$$

Combining Equations (10)–(11) and Equations (14)–(16), the governing equation can give as:

$$\frac{\partial\eta_{rex}}{\partial t} = -L\left\{ m[\eta_{rex}^3 - \eta_{rex} + 2\gamma\eta_{rex}(\eta_{def1}^2 + \eta_{def2}^2)] - k\nabla^2\eta_{rex} - \frac{2\eta_{rex}(\eta_{def1}^2 + \eta_{def2}^2)}{(\eta_{rex}^2 + \eta_{def1}^2 + \eta_{def2}^2)^2}P \right\} \tag{17}$$

$$\frac{\partial\eta_{def1}}{\partial t} = -L\left\{ \begin{array}{l} m[\eta_{def1}^3 - \eta_{def1} + 2\gamma\eta_{def1}(\eta_{rex}^2 + \eta_{def2}^2)] - k\nabla^2\eta_{def1} \\ + \dfrac{2\eta_{def1}\eta_{rex}^2}{(\eta_{rex}^2 + \eta_{def1}^2 + \eta_{def2}^2)^2}P \end{array} \right\} \tag{18}$$

$$\frac{\partial\eta_{def2}}{\partial t} = -L\left\{ \begin{array}{l} m[\eta_{def2}^3 - \eta_{def2} + 2\gamma\eta_{def2}(\eta_{rex}^2 + \eta_{def1}^2)] \\ -k\nabla^2\eta_{def2} + \dfrac{2\eta_{def2}\eta_{rex}^2}{(\eta_{rex}^2 + \eta_{def1}^2 + \eta_{def2}^2)^2}P \end{array} \right\} \tag{19}$$

2.3. Simulation process and model parameters

A modified Voronoi model was utilised to establish the 3-D microstructure containing GBs with specific tilting angles. Based on the GB energies obtained from the molecular dynamics simulations, five representative GBs were set up, namely, 15°, 46.91°, and 61.91° symmetric tilt GBs for [1–210] [30], and 15° and 72.88° symmetric tilt GBs for [0–1–10] [31], as shown in Table 1. These GBs can be captured in sections of the model in x-y direction, as shown in Figure 1. The initial model comprises 8 grains, with dimensions of 10^{-4}m × 10^{-4}m × 10^{-4}m and a grid count of 10^6.

Table 1. Parameters of the set symmetric tilt GBs.

GB number	Rotation axis	Rotation angle	GB energy (mJ/m^2)
GbI	[1–210]	15°	367
GbII	[1–210]	46.91°	334
GbIII	[1–210]	62.06°	105
GbIV	[0–1–10]	15°	393
GbV	[0–1–10]	72.88°	71

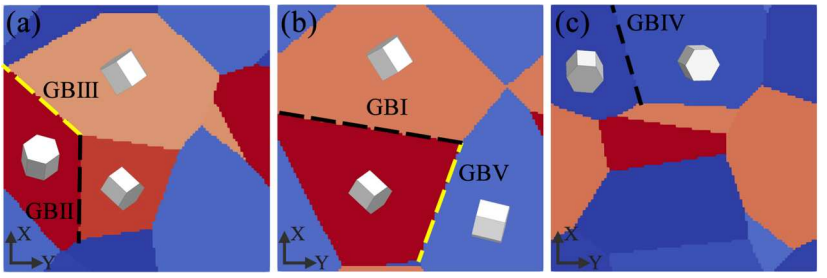

Figure 1. The GBs set in the microstructure.

Uniaxial compression simulations of magnesium were carried out using the established CP model. The elastic deformation parameters were adopted from single-crystal elastic constants calculated by Slutsky [32], while the plastic deformation parameters were adopted from Wang's values of phenomenological crystal plasticity [33], as shown in Table 2. The model was subjected to uniaxial compression, as shown in Figure 2.

The regions near the set GBs at 1/4, 1/2 and 3/4 sections were selected for PF simulation. Flat and 120° GBs were constructed near the original GBs as shown schematically in Figure 3. The recrystallized grain and the original grains constitute a triple junction. The boundaries of the recrystallized grains are set as symmetric tilt GBs for [1–210], using the average energy of this type of GBs, 234.0 mJ/m² [30]. To enhance the precision of the simulation computations, the grid was re-subdivided via Lagrangian interpolation by rows.

The local misorientation in the simulation can be characterised by the distribution of the PF variables. Neglecting inclination dependence, the model constants can be calculated as Equations (20). The values of constants between different grains were obtained by calculations with the algorithm provided by Moelans [19]. Mixed boundary conditions were employed. Symmetric boundary conditions are applied to the model boundaries that are not connected to the GBs. For the model boundaries that are connected to the GBs, the PF variables and the stored energy field are made symmetric along the normal direction of the GBs. The model parameters were set as follows: $l_{gb} = 6 \times 10^{-7}$

Table 2. Constants of CP simulation for Mg.

Property	Value	Property	Value	Property	Value
C_{11}	59.50e + 9	$S_{0,basal}$	10×10^6	$S_{0,pyr(c+a)}$	60×10^6
C_{33}	61.72e + 9	$S_{\infty,basal}$	40×10^6	$S_{\infty,pyr(c+a)}$	150×10^6
C_{44}	16.46e + 9	$S_{0,prism}$	55×10^6	$h_{0,sl-sl}$	500×10^6
C_{12}	25.62e + 9	$S_{\infty,prism}$	135×10^6	$s_{0,T1}$	40×10^6
C_{13}	21.46e + 9	$S_{0,pyr(a)}$	60×10^6	$h_{0,t-t}$	50×10^6
–	–	$S_{\infty,pyr(a)}$	150×10^6	$h_{0,t-sl}$	150×10^6

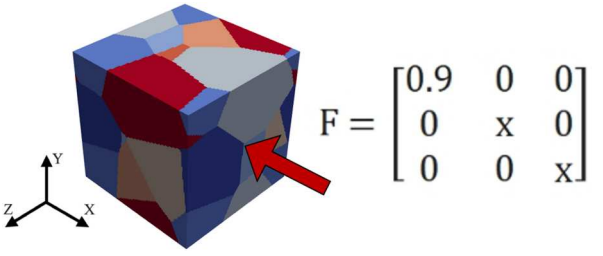

Figure 2. Schematic diagram of the uniaxial compression.

m, dx = 1×10^{-7} m, and a time step of dt = 0.005 s.

$$\begin{cases} L(\theta,\ \phi) = \dfrac{\sum_{i=1}^{p}\sum_{j>i}^{p} L_{i,j}\eta_i^2\eta_j^2}{\sum_{i=1}^{p}\sum_{j>i}^{p}\eta_i^2\eta_j^2} \\ \gamma(\theta,\ \phi) = \dfrac{\sum_{i=1}^{p}\sum_{j>i}^{p} \gamma_{i,j}\eta_i^2\eta_j^2}{\sum_{i=1}^{p}\sum_{j>i}^{p}\eta_i^2\eta_j^2} \\ k(\theta,\ \phi) = \dfrac{\sum_{i=1}^{p}\sum_{j>i}^{p} k_{i,j}\eta_i^2\eta_j^2}{\sum_{i=1}^{p}\sum_{j>i}^{p}\eta_i^2\eta_j^2} \end{cases} \tag{20}$$

3. Results

3.1. Migration of flat boundaries during recrystallization

In the PF simulation, the points of $\eta_{rex} = 0.5$ are extracted as the location of the boundaries of recrystallized grains. Figure 4 illustrates the migration of flat boundaries in the stored energy field generated by plastic deformation. The cloud diagram represents the distribution of the stored energy field near the GBs obtained by CP simulation. The grey areas indicate the constructed recrystallized grains. The boundaries of recrystallized grains at 3×10^4, 6×10^4, 9×10^4, and 12×10^4 time steps are marked by lines of different colours. Boundaries exhibit a faster migration rate in regions of high stored energy. When the stored energies are comparable, the boundaries of the recrystallized grains near triple

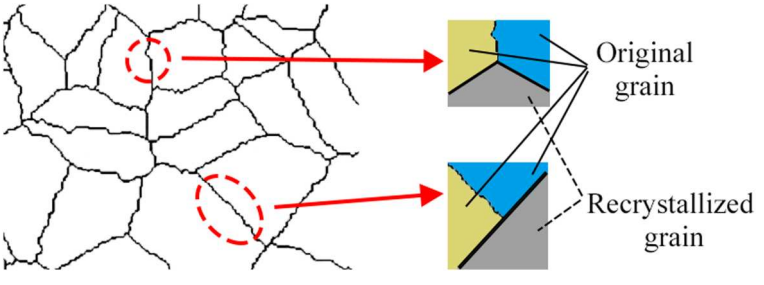

Figure 3. Schematic diagram of the PF simulation for recrystallization.

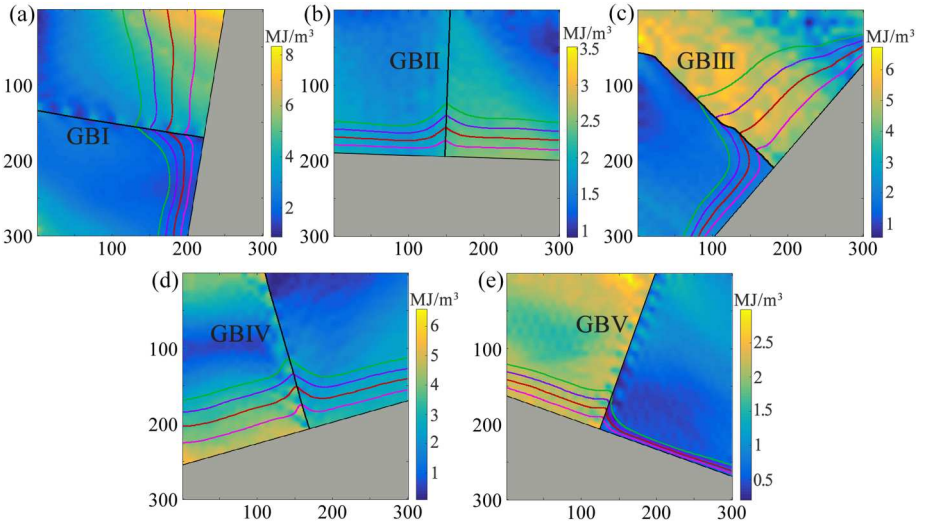

Figure 4. Migration of the flat GBs near (a) GBI; (b) GBII; (c) GBIII; (d) GBIV; (e) GBV.

junctions migrate farther than the other regions, which results in a change in the grain boundary shape within a certain range.

For each point along the GB on the reference configuration, the average migration velocities over specific time intervals are calculated and denoted as V_{GB}. Figure 5 illustrates the distribution of V_{GB} centred on the triple junction. In each simulation, G.A and G.B represent the two original grains. Within the area of each original grain, the overall average migration velocity of all points along the boundary of the recrystallized grain is denoted as $V_{GB,\,tol}$. In contrast to the GB migration behaviour under a uniform deformation field [34], there is

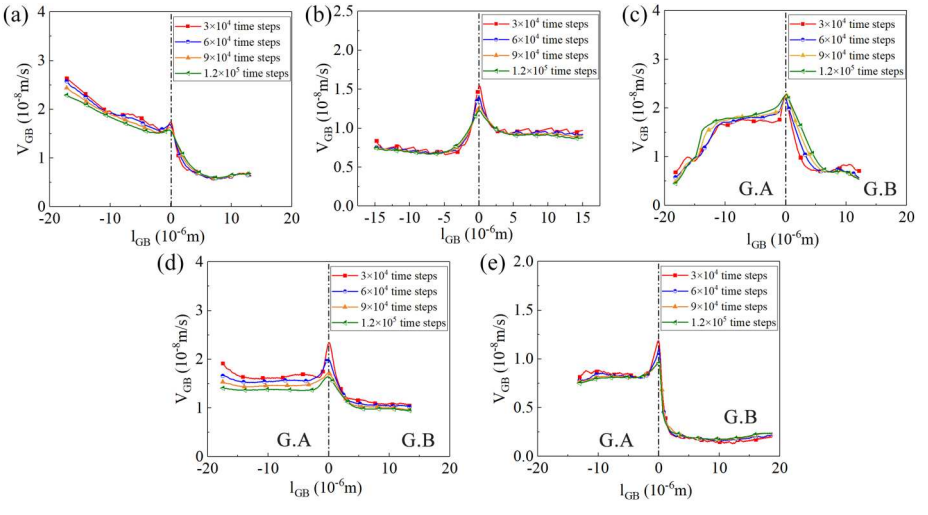

Figure 5. The VGB distribution of flat GBs near (a) GBI; (b) GBII; (c) GBIII; (d) GBIV; (e) GBV.

a notable discrepancy in $V_{GB,\ tol}$ within the different original grains. The GB shape at the triple junction is formed during the initial stages of migration. During the first 3×10^4 s of the simulation, the V_{GB} near the triple junction is significantly larger than that in the other regions. As time proceeds, the average migration rate in the region near the triple junction decreases. In contrast, the change in V_{GB} over time is less in regions outside the triple junction.

By integrating the curves on each side of the triple junction in Figure 5, the total average migration velocities within the G.A and G.B are calculated, as shown in Table 3. In the inhomogeneous plastic stored energy field, recrystallized grains exhibit distinct velocities in each original grains. There are significant variations in stored energy on both sides of GbI, GbIII, and GbV, and there are also large differences in the migration rates of their corresponding GBs. On both sides of GbV, where variations in stored energy are most significant, the value of $V_{GB,\ tol}$ within high stored energy grains is 3.8–4.4 times that of low stored energy grains. Near the remaining four GBs, the ratios of the $V_{GB,\ tol}$ values are 2.7–3.2, 1.2–1.3, 1.5–1.6, and 1.3–1.4, respectively. Among them, the migration speeds on both sides of GbII are comparable. There is no significant difference in $V_{GB,\ tol}$ across different time steps. The gradient of migration velocity within grains is much smaller than that between grains.

3.2. Migration of boundaries with 120° triple junctions during recrystallization

Figure 6 shows the evolution of 120° triple junctions constructed in the same region. The shape of the GBs is maintained and an overall migration occurs when the stored energy field changes slightly. In regions such as Figure 6(c), it can be observed that V_{GB} is significantly higher in the high stored energy region compared to the low stored energy region, causing localised bulging of the GBs.

Quantification of the migration rate on the GBs is shown in Figure 7. Due to the differences in the angles and positions of the set GBs, the 120° GBs are not subjected to precisely the same stored energy field as the flat GBs. The distribution of V_{GB} is close to but slightly different from that depicted in Figure 5. In addition, the V_{GB} near the triple junction is significantly smaller than that

Table 3. The total average migration velocities of the flat GBs.

Time steps	Region	GbI (10^{-8} m/s)	GbII (10^{-8} m/s)	GbIII (10^{-8} m/s)	GbIV (10^{-8} m/s)	GbV (10^{-8} m/s)
3×10^4	G.A	1.98	0.77	1.49	1.68	0.93
	G.B	0.74	1	0.92	1.24	0.21
6×10^4	G.A	1.94	0.76	1.51	1.59	0.89
	G.B	0.74	0.97	0.96	1.16	0.22
9×10^4	G.A	1.88	0.75	1.56	1.48	0.88
	G.B	0.77	0.96	1.02	1.1	0.23
1.2×10^5	G.A	1.81	0.8	1.6	1.39	0.87
	G.B	0.78	0.94	1.08	1.07	0.23

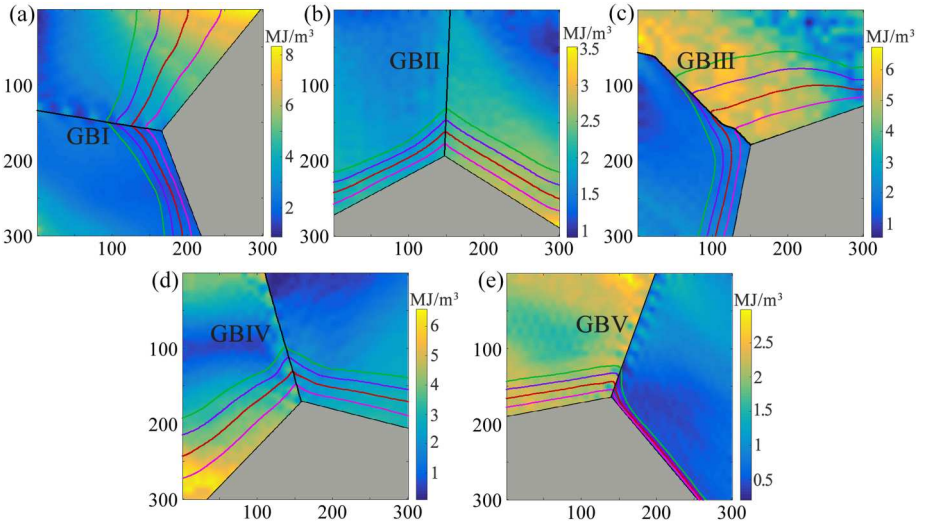

Figure 6. Migration of the 120° triple junction near (a) GBI; (b) GBII; (c) GBIII; (d) GBIV; (e) GBV.

of the flat GB. At the simulation scale, when the stored energy fields are similar, the boundaries of the recrystallized grains largely maintain their original shape.

The total average migration velocities of 120° boundaries within G.A and G.B are shown in Table 4. Across the five simulations, the ratios of $V_{GB,\ tol}$ for high stored energy grains to low stored energy grains are 2.1~2.6, 1.2~1.3, 1.6~1.9, 1.3~1.7, and 3.8~4.0, respectively. Similar to the characteristics of the flat GBs, the migration rate is close on both sides of GbII, while the ratio of $V_{GB,\ tol}$ is the largest on both sides of GbV. In addition, due to

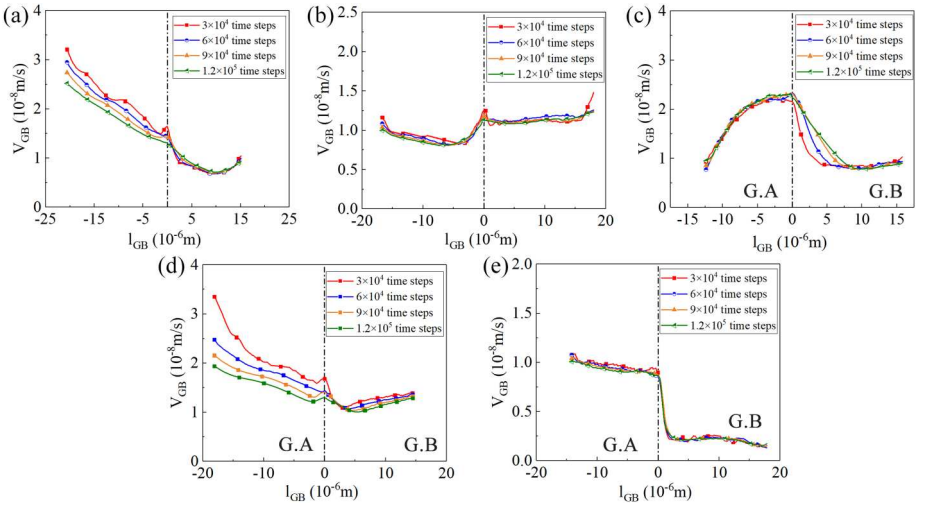

Figure 7. The VGB distribution of 120° triple junction near (a) GBI; (b) GBII; (c) GBIII; (d) GBIV; (e) GBV.

Table 4. The total average migration velocities near the 120° triple junction.

Time steps	Region	GbI (10^{-8} m/s)	GbII (10^{-8} m/s)	GbIII (10^{-8} m/s)	GbIV (10^{-8} m/s)	GbV (10^{-8} m/s)
3×10^4	G.A	2.22	0.94	1.84	2.13	0.97
	G.B	0.86	1.14	0.99	1.28	0.24
6×10^4	G.A	2.08	0.92	1.86	1.85	0.95
	G.B	0.86	1.16	1.08	1.22	0.24
9×10^4	G.A	1.95	0.9	1.89	1.67	0.94
	G.B	0.88	1.14	1.14	1.19	0.25
1.2×10^5	G.A	1.84	0.9	1.89	1.53	0.93
	G.B	0.89	1.12	1.18	1.15	0.24

the inhomogeneous deformation within the grain under plastic loading, the regions swept by the 120° boundaries in the simulations of GbI and GbIII have a larger stored energy field than that of the flat GBs, and the results show that the $V_{GB,\ tol}$ is also slightly larger.

4. Discussion

4.1. Effect of the orientation of original grains

The PF simulation in this study involves six original grains with distinct grain orientations. By computing the average value of all V_{GB} of these six grains, the relationship between the Schmid factors (SFs) of the original grains and the migration velocity at the GB can be explored, as shown in Figure 8. In polycrystalline systems, the coordination among grains leads to deformation inhomogeneities. Basal slip serves as the primary plastic deformation mechanism during room temperature loading. Grains with low SFs (less than 0.3) exhibit limited activation of basal slip, prompting neighbouring grains to accommodate more dislocations for generating strain gradients, which provide a stored energy driver for GB motion. The overall trend illustrated in Figure 8

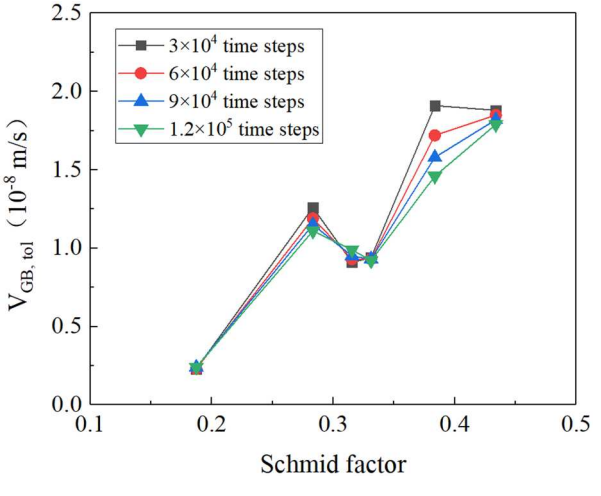

Figure 8. The relationship between the SFs of original grains and VGB.

shows that there is an indirect relationship between SFs and grain boundary migration rate. However, the total number of grains in the simulation is relatively small, and the coordinated deformation effect among grains is limited. Dislocations may still be activated in grains with hard orientation due to large stresses. The SFs and plastic deformation stored energy cannot strictly correspond to each other, as exemplified by the simulation of GBIV. Moreover, as plastic deformation increases, considering the activation of other deformation mechanisms such as grain rotation and grain boundary sliding, the relationship might be less clear.

Differences in stored energy among original grains have a profound impact on the shape of GBs. The GBs connected at the triple junction influence the migration of each other. In Figure 9, the evolution of GBs near the 120° triple junction is analyzed using GBII and GBIII as examples. Although the triple junctions maintain equilibrium during movement, the GBs curve in response to deformation energy. The GBs rapidly advance in regions of high strain, while in grains with low strain, the V_{GB} is lower. The displacement difference between these two grains leads to relatively large curvature changes. The GBs adjacent to grains with high stored energy fields move in the opposite direction of the curvature radius. The movement is hindered as the system attempts to minimise energy as quickly as possible. In grains with low stored energy fields, the curvature radius is in the same direction as the GB movement, which promotes the movement of the GBs.

A larger difference in the migration distance of the boundaries results in a greater mutual influence between the connected GBs. For exploring the contribution of GB curvature on the mesoscopic scale, additional simulations focusing on the pure curvature effect were conducted based on the original results, as shown in Figure 10. The black line in the figure represents the migration of the 120° GBs in the GBIII region in the previous section, when the GBs were subjected to a combination of deformation stored energy and GB free energy (denoted as S + G). The deformation field was then removed and the simulation was performed for another 5.4×10^5 time steps (denoted as G). Datas are recorded every 3×10^4 for the initial 9×10^4 time steps, marked with coloured

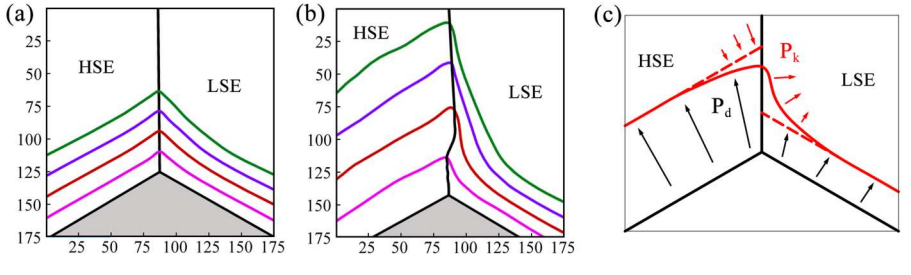

Figure 9. The GB evolution near the 120° triple junction (a) near GBII; (b) near GBIII; (c) The energy minimisation process.

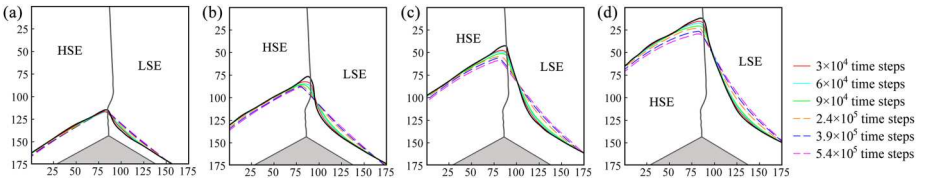

Figure 10. Migration without deformation field after the (S + G) simulation for (a) 3×10^4 time steps; (b) 6×10^4 time steps; (c) 9×10^4 time steps; (d) 1.2×10^5 time steps.

solid lines. Subsequent dates are captured at 1.5×10^5 intervals and are marked with coloured dashed lines. The results show that curvature plays a more significant role in the dynamic process of GB migration within the plastic deformation field. Compared to 3×10^4(S + G) + 6×10^4(G), the mutual influence of the connected GBs is more severe at 9×10^4(S + G). Further simulation for 6×10^4(G) does not lead to significant changes in GBs. The GB cusps generated by inhomogeneous deformation fields cause a sharp rise in the instantaneous curvature effect, increasing the contribution of GB curvature in the recrystallization process. In contrast, in the absence of deformation fields, the evolution of GBs proceeds slowly. In addition, when the simulation time is long enough, the motion of the original GBs can no longer be ignored. The GBs between the three grains will migrate in a coordinated manner. This process will continue until the entire system reaches a steady state.

4.2. Effects of original grain boundaries

The growth process of a recrystallized grain involves both the boundaries of recrystallized grains and the original GB that it sweeps through. In this study, to compare the evolution of GBs under different plasticity stored energy fields, the boundaries of recrystallized grains were chosen to have homogeneous GB energies and migration rates. However, it is anticipated that differences in the GB energies of recrystallized grains will directly affect the migration process of the GBs. In regions far from the triple junction, the constants in Equations (17)–(19) can be calculated by the GB mobility (Mgb) and σgb approximately [29]: $L = 4/3 \cdot M_{gb}/l_{gb}$, $K = 3/4 \cdot \sigma_{gb} \cdot l_{gb}$, and $m = 6 \cdot \sigma_{gb}/l_{gb}$ (M_{gb} is grain boundary mobility, and l_{gb} is diffuse interface width).

When the inclination-dependence of the GB energy is neglected, the equilibrium dihedral angle can be calculated using Young's law [35]:

$$\frac{\gamma_1}{\sin(\beta_1)} = \frac{\gamma_2}{\sin(\beta_2)} = \frac{\gamma_3}{\sin(\beta_3)} \tag{21}$$

where γ_i is the GB energy, and β_i is the dihedral angles.

To validate the dihedral angle of the phase field model, the non-equilibrium tricrystal structures were used for the simulation. Except for removing the

deformation field, the model parameters were the same as those used in the CP-PF simulation. After the system had reached stability, the triple junction angle was measured and denoted as β_i'. Table 5 shows that the phase field model conforms to Young's law near the triple junction.

At the initial stage of the flat boundaries simulation, the macroscopic angles between the GBs are significantly larger than the equilibrium dihedral angle. In all simulations, regardless of how the stored energy field is distributed, the triple junction always exhibits a higher migration rate, leading to a change in the shape of the grain boundary. The PF model used in this study cannot reflect whether the migration speed is uniform at smaller scales. In Equations (17)–(19), the third term of the stored energy directly affects the migration rate, which results in uneven migration velocities under an inhomogeneous deformation field at this scale. Meanwhile, the macroscopic grain boundary shape also deviates considerably from the equilibrium angle at the triple junction, as seen in the simulation of the 120° triple junction in GBIII. Only when the stored energy gradient is small will the triple junction obtain a relatively uniform migration velocity, as shown in Figure 6(b).

Apart from constituting triple junctions, the energy of the original GBs also contributes to the local GB migration. Table 6 shows the migration rates of triple junctions for five groups of flat GBs at the early stage of simulation. Within the first 1×10^4 time steps, the original GB energy, stored energy, and GB curvature collectively drive the triple junctions forward. As time proceeds, the migration rate at the triple junction decreases rapidly, approaching the value observed in regions distant from the triple junction.

In Equation (20), the simulation constants at the diffuse interface near the triple junction are calculated based on the PF variables. Higher original GB energies and mobilities would theoretically lead to triple junctions moving forward more significantly. To validate the point, we added multiple sets of simulations. The five sets of simulation constant values described in the previous section were interchanged, and then the same boundaries of recrystallized grains were set. The results show that the migration rates at the GBs fronts differ by less than 1%. Even if a higher migration rate is provided by the original GBs, it is counteracted by the effect of the curvature. The energy of the original GBs is not sufficient to cause significant impact on mesoscopic scale.

Table 5. The triple junction dihedral angles under different GB energies. β_i is the theoretically expected angle, while β_i' is the angle measured from the simulation.

	β1	β1′	β2	β2′	β3	β3′
GbI	141.6°	139.9°	109.2°	110.1°	109.2°	110.1°
GbII	135.5°	137.5°	112.2°	111.3°	112.2°	111.3°
GbIII	103.0°	101.6°	128.5°	129.2°	128.5°	129.2°
GbIV	147.1°	146.5°	106.4°	106.8°	106.4°	106.8°
GbV	98.7°	97.4°	130.6°	131.3°	130.6°	131.3°

Table 6. The migration rates of triple junctions at the early stage of simulation.

Time steps ($\times 10^3$)	GbI (10^{-8} m/s)	GbII (10^{-8} m/s)	GbIII (10^{-8} m/s)	GbIV (10^{-8} m/s)	GbV (10^{-8} m/s)
0–5	2.40	2.26	2.83	3.13	1.73
5–10	2.00	1.85	2.49	2.56	1.42
10–20	1.57	1.29	2.17	2.18	1.01
20–30	1.44	1.29	2.01	1.98	1.01

4.3. Comparison with experimental results

GB migration under stored energy fields in this study focuses on the annealing process after deformation. Not limited to room-temperature rolling or uniaxial compression, it is informative for various processes involving static recrystallization. Boundary evolution over 6.6×10^5 time steps was demonstrated in the simulations, corresponding to a high temperature annealing for 55 minutes. The deformed grains can not be completely replaced by the recrystallized grains within a short period of time, when the residual deformation field still influences the migration of the boundaries of recrystallized grains.

In CP-PF simulations, it is predicted that grains with high SFs are more susceptible to high stored energy fields and high migration velocities of the boundaries of recrystallized grains. Moreover, the triple junctions coordinate boundary motions near original GBs by curvature. The tendency is consistent with what has been observed in static recrystallization experiments of Mg, where the recrystallized grain prefers to swallow grains with severe deformation when surrounded by multiple grains [36]. Yin demonstrates the influence of SFs and the effect of triple junctions on GB migration in annealed high-purity aluminum after cold rolling [37]. This is particularly important in the study of bimodal microstructures. In some of the current studies the annealing process was used to design the bimodal grain structure [38–40]. During incomplete dynamic recrystallization, the growth of recrystallized grains has a distinctly preferential direction. In hot rolling of Mg-Al alloys, Jin [41] found that grains with c-axis parallel to ND are in a hard orientation, and limited by the stored energy, are not easily swallowed by the surrounding grains via DRX. Although the effect on GB migration is multifactorial in polycrystals, a relatively large number of hardly oriented grains still remain, which can lead to an increase in the intensity of the basal texture in annealed samples [38]. The observation is well explained by CP-PF simulations.

In this study, a 2-D PF simulation is used considering the efficiency of computer simulation. However, in order to obtain a more accurate stored energy field, the CP model is built in a 3-D system. The deformation field on the cross-section ignores the gradient in the z-direction. The inhomogeneity in the z-direction also leads to differences in the mobility and acts on the cross-section through the curvature, which is a limitation in 2-D simulations. In addition, the programme cannot automatically determine the grain boundary migration direction based on phase field values or stored energy. In current

simulations, recrystallized and deformed grains must be manually differentiated. The stored energy term is negative in recrystallized grains and positive in deformed grains, guiding the boundary movement. This approach inevitably ignores the stored energy gradient between deformed grains.

Within the scale of the tricrystal model, the model boundaries can significantly influence the simulation results. The mixed boundary conditions used in this study effectively reduce the interference from these boundaries. At the model boundaries, the GBs exhibit a smooth transition. There are no significant boundary effects in Figure 4 and Figure 6. The differences in V_{GB} at the model boundaries in some simulation results (Figure 4(c) and Figure 6(c)) are attributed to the inhomogeneous stored energy field. Furthermore, it has been shown that the orientation relationship between the growing grains and the matrix can play a greater role in migration [42]. Though the gradient of the stored energy field is larger in this paper, this is still an issue worth considering. This research had to set up a homogeneous orientation relation in order to compare the effect of the stored energy field. When compared to experimental results, the model has higher accuracy at lower temperatures due to the greater influence of the stored energy field [43]. The respective contributions of GB energy and stored energy require larger computational models to compare.

5. Conclusions

In this paper, a CP-PF model for the boundary migration of recrystallized grains in the deformation field is developed. The migration of flat GBs and 120° GBs under the stored energy field obtained by plastic deformation is analyzed using the material parameters of magnesium. The main results are as follows:

(1) Curvature has a more significant effect under inhomogeneous stored energy fields. The gradient in local migration distance generated by the stored energy field increases the nearby curvature. Otherwise, in the no-deformation simulation, the migration velocity of GBs with small curvature is slight.
(2) The orientation of the original grains affects the magnitude of the stored energy. Grains with soft orientation are more easily swallowed by the recrystallized grains during the annealing process after deformation. However, between original grains with large difference in the stored energy field, the migration of connected GBs will mutually influence each other, which causes the grains with hard orientation to be partially swallowed.
(3) When the angles at the triple junctions significantly deviate from equilibrium, the effect of GB energy on GB migration will exceed the deformation energy. The triple junctions of flat GBs exhibit a faster migration

rate compared to 120° GBs. The migration rate of triple junctions decreases as the simulation proceeds until it reaches stability.

(4) When the original grains are swallowed by the recrystallized grains, the energy difference of the original GBs has a small effect on migration velocity, which is not enough to create a obvious phenomenon at the mesoscopic scale.

(5) The results of CP-PF simulation are consistent with the experiments, and the observations in experiments can be explained quantitatively by CP-PF simulation. This method has the potential for engineering applications in predicting the evolution of recrystallized microstructure under deformation and heat treatment processes.

Disclosure statement

No potential conflict of interest was reported by the author(s).

Funding

This work was supported by the National Natural Science Foundation of China (NSFC52475334) and the Fundamental Research Funds for the Central Universities (2022FRFK060003).

Data availability statement

The raw/processed data required to reproduce these findings cannot be shared at this time as the data also forms part of an ongoing study.

References

[1] A. Alpers, M. Fiedler, P. Gritzmann, and F. Klemm, *Dynamic grain models via fast heuristics for diagram representations*. Philos. Mag. 103 (2023), pp. 948–968.

[2] M.Y. Jiang, X.Z. Zhang, H. Mei, S. Xu, and L.S. Liu, *The coupled effects of grain boundary strengthening and Orowan strengthening examined by dislocation dynamics simulations*. Comput. Mater. Sci. 231 (2024), pp. 112602.

[3] J.J. Li and A.K. Soh, *Synergy of grain boundary sliding and shear-coupled migration process in nanocrystalline materials*. Acta Mater. 61 (2013), pp. 5449–5457.

[4] A.P. Hua and J.H. Zhao, *A unified disconnection model of stress-driven grain boundary migration in nanocrystalline metals*. J. Mech. Phys. Solids 183 (2024), pp. 105515.

[5] N. Moelans, *New phase-field model for polycrystalline systems with anisotropic grain boundary properties*. Mater. Des. 217 (2022), pp. 110592.

[6] J.K. Wei, B. Feng, R. Ishikawa, T. Yokoi, K. Matsunaga, N. Shibata, and Y. Ikuhara, *Direct imaging of atomistic grain boundary migration*. Nat. Mater. 20 (2021), pp. 951–955.

[7] E.N. Borodin and A.P. Jivkov, *Evolution of triple junctions' network during severe plastic deformation of copper alloys - a discrete stochastic modelling*. Philos. Mag. 100 (2020), pp. 467–485.

[8] Q. Huang, W. Yang, and H. Zhou, *Migration of grain boundary triple junctions in nanocrystalline metals initiated by accumulated dislocations*. Int. J. Plast. 173 (2024), pp. 103872.
[9] D. Weygand, Y. Bréchet, J. Lépinoux, and W. Gust, *Three-dimensional grain growth:: a vertex dynamics simulation*. Philos. Mag. B 79 (1999), pp. 703–716.
[10] J.K. Becker, P.D. Bons, and M.W. Jessell, *A new front-tracking method to model anisotropic grain and phase boundary motion in rocks*. Comput. Geosci. 34 (2008), pp. 201–212.
[11] E.A. Holm, M.A. Miodownik, and A.D. Rollett, *On abnormal subgrain growth and the origin of recrystallization nuclei*. Acta Mater. 51 (2003), pp. 2701–2716.
[12] J. Gruber, H.M. Miller, T.D. Hoffmann, G.S. Rohrer, and A.D. Rollett, *Misorientation texture development during grain growth. Part I: simulation and experiment*. Acta Mater. 57 (2009), pp. 6102–6112.
[13] H. Hallberg and P.A.T. Olsson, *Investigation of microstructure evolution during self-annealing in thin Cu films by combining mesoscale level set and modeling*. J. Mech. Phys. Solids 90 (2016), pp. 160–178.
[14] M.A. Martorano, H.R.Z. Sandim, M.A. Fortes, and A.F. Padilha, *Observations of grain boundary protrusions in static recrystallization of high-purity bcc metals*. Scr. Mater. 56 (2007), pp. 903–906.
[15] L.Q. Chen and W. Yang, *Computer-Simulation of the domain dynamics of a quenched system with a large number of nonconserved order parameters - the grain-growth kinetics*. Phys. Rev. B 50 (1994), pp. 15752–15756.
[16] D. Fan and L.Q. Chen, *Computer simulation of grain growth using a continuum field model*. Acta Mater. 45 (1997), pp. 611–622.
[17] C.E. Krill and L.Q. Chen, *Computer simulation of 3-D grain growth using a phase-field model*. Acta Mater. 50 (2002), pp. 3057–3073.
[18] A. Kazaryan, Y. Wang, S.A. Dregia, and B.R. Patton, *Grain growth in anisotropic systems: comparison of effects of energy and mobility*. Acta Mater. 50 (2002), pp. 2491–2502.
[19] N. Moelans, B. Blanpain, and P. Wollants, *Quantitative analysis of grain boundary properties in a generalized phase field model for grain growth in anisotropic systems*. Phys. Rev. B 78 (2008), pp. 024113.
[20] Y.M. Zhang and L.L. Liu, *Grain growth behavior of ferroelectric ceramics under anisotropic grain boundary energy conditions simulated by the phase field method*. Ceram. Int. 48 (2022), pp. 23767–23776.
[21] Y.B. Zhang, J.D. Budai, J.Z. Tischler, W. Liu, R. Xu, E.R. Homer, A. Godfrey, and D.J. Jensen, *Boundary migration in a 3D deformed microstructure inside an opaque sample*. Sci. Rep. 7 (2017), pp. 4423.
[22] V. Yadav, N. Moelans, Y.B. Zhang, and D.J. Jensen, *Effects of dislocation boundary spacings and stored energy on boundary migration during recrystallization: A phase-field analysis*. Acta Mater. 221 (2021), pp. 117377.
[23] F. Roters, M. Diehl, P. Shanthraj, P. Eisenlohr, C. Reuber, S.L. Wong, T. Maiti, A. Ebrahimi, T. Hochrainer, H.O. Fabritius, S. Nikolov, M. Friák, N. Fujita, N. Grilli, K.G.F. Janssens, N. Jia, P.J.J. Kok, D. Ma, F. Meier, E. Werner, M. Stricker, D. Weygand, and D. Raabe, *DAMASK - The Dusseldorf advanced material simulation kit for modeling multi-physics crystal plasticity, thermal, and damage phenomena from the single crystal up to the component scale*. Comput. Mater. Sci. 158 (2019), pp. 420–478.
[24] M. Salvini, N. Grilli, E. Demir, S.Q. He, T. Martin, P. Flewitt, M. Mostafavi, C. Truman, and D. Knowles, *Effect of grain boundary misorientation and carbide precipitation on damage initiation: A coupled crystal plasticity and phase field damage study*. Int. J. Plast. 172 (2024), pp. 103854.

[25] J.R. Rice, *Inelastic constitutive relations for solids: An internal-variable theory and its application to metal plasticity*. J. Mech. Phys. Solids 19 (1971), pp. 433–455.
[26] S.R. Kalidindi, *Incorporation of deformation twinning in crystal plasticity models*. J. Mech. Phys. Solids 46 (1998), pp. 267–271.
[27] A. Arsenlis and D.M. Parks, *Crystallographic aspects of geometrically-necessary and statistically-stored dislocation density*. Acta Mater. 47 (1999), pp. 1597–1611.
[28] M. Jafari, M. Jamshidian, S. Ziaei-Rad, D. Raabe, and F. Roters, *Constitutive modeling of strain induced grain boundary migration via coupling crystal plasticity and phase-field methods*. Int. J. Plast. 99 (2017), pp. 19–42.
[29] N. Moelans, A. Godfrey, Y.B. Zhang, and D.J. Jensen, *Phase-field simulation study of the migration of recrystallization boundaries*. Phys. Rev. B 88 (2013), pp. 054103.
[30] J. Wang and I.J. Beyerlein, *Atomic structures of symmetric tilt grain boundaries in hexagonal close packed (hcp) crystals*. Modell. Simul. Mater. Sci. Eng. 20 (2012), pp. 024002.
[31] J. Wang and I.J. Beyerlein, *Atomic structures of [0–110] symmetric tilt grain boundaries in hexagonal close-packed (hcp) crystals*. Metallurgical and Materials Transactions A 43 (2012), pp. 3556–3569.
[32] L.J. Slutsky and C.W. Garland, *Elastic constants of magnesium from 4.2°K to 300°K*. Phys. Rev. 107 (1957), pp. 972–976.
[33] F. Wang, S. Sandlöbes, M. Diehl, L. Sharma, F. Roters, and D. Raabe, *In situ observation of collective grain-scale mechanics in Mg and Mg-rare earth alloys*. Acta Mater. 80 (2014), pp. 77–93.
[34] V.M. Kindrachuk and R.D. Kamachali, *Mean-field modeling and phase-field simulation of grain growth under directional driving forces*. Materialia 33 (2024), pp. 101989.
[35] P. Staublin, A. Mukherjee, J.A. Warren, and P.W. Voorhees, *Phase-field model for anisotropic grain growth*. Acta Mater. 237 (2022), pp. 118169.
[36] X. Ye, Z. Suo, Z. Heng, B. Chen, Q. Wei, J. Umeda, K. Kondoh, and J. Shen, *An in-situ study of static recrystallization in Mg using high temperature EBSD*. Journal of Magnesium and Alloys 12 (2024), pp. 1419–1430.
[37] W.H. Yin, W.G. Wang, X.Y. Fang, C.X. Qin, and X.G. Xing, *Migration of grain boundaries and triple junctions in high-purity aluminum during annealing after slight cold rolling*. Mater. Charact. 107 (2015), pp. 134–138.
[38] B.J. Wang, D.K. Xu, L.Y. Sheng, E.H. Han, and J. Sun, *Deformation and fracture mechanisms of an annealing-tailored "bimodal" grain-structured Mg alloy*. J. Mater. Sci. Technol. 35 (2019), pp. 2423–2429.
[39] M.A. Mostafaei and M. Kazeminezhad, *Bimodal grain size and mechanical properties enhancement in low carbon steel by ultra-rapid annealing*. J. Mater. Res. Technol. 18 (2022), pp. 2363–2367.
[40] A. Salandari-Rabori, A. Zarei-Hanzaki, S. Asqardoust, H.R. Abedi, T. Krajnák, P. Minarik, and J. Vesely, *Novel RE-texture component and bimodal microstructure formation during post-annealing of an accumulative back extruded WE43 alloy*. Mater. Lett. 337 (2023), pp. 134006.
[41] Q.L. Jin, S.Y. Shim, and S.G. Lim, *Correlation of microstructural evolution and formation of basal texture in a coarse grained Mg-Al alloy during hot rolling*. Scr. Mater. 55 (2006), pp. 843–846.
[42] C.S. Hong, Y.B. Zhang, A. Lindkvist, W.J. Liu, J. Tischler, R.Q. Xu, and D.J. Jensen, *Recrystallization boundary migration in the 3D heterogeneous microstructure near a hardness indent*. Scr. Mater. 205 (2021), pp. 114187.
[43] X. Wang, T. Liu, R. Zhang, H. Jin, X. Zhao, W. Wu, and J. Cheng, *Texture evolution related to static recrystallization during annealing of TA15 alloy tube formed by flow forming*. J. Mater. Res. Technol. 24 (2023), pp. 5769–5781.

Philosophical Magazine

ISSN: 1478-6435 (Print) 1478-6443 (Online) Journal homepage: www.tandfonline.com/journals/tphm20

Investigating particle-particle interaction during the initial crystal growth: insights from phase field model approach

Nan Liu, Ming-Wen Chen, Mingli Zhang & Zidong Wang

To cite this article: Nan Liu, Ming-Wen Chen, Mingli Zhang & Zidong Wang (2025) Investigating particle-particle interaction during the initial crystal growth: insights from phase field model approach, Philosophical Magazine, 105:14, 777-793, DOI: 10.1080/14786435.2025.2451728

To link to this article: https://doi.org/10.1080/14786435.2025.2451728

PHILOSOPHICAL MAGAZINE
2025, VOL. 105, NO. 14, 777–793
https://doi.org/10.1080/14786435.2025.2451728

Taylor & Francis
Taylor & Francis Group

Investigating particle-particle interaction during the initial crystal growth: insights from phase field model approach

Nan Liu [a], Ming-Wen Chen[a], Mingli Zhang[a] and Zidong Wang[b]

[a]School of Mathematics and Physics, University of Science and Technology Beijing, Beijing, People's Republic of China; [b]School of Materials Science and Engineering, University of Science and Technology Beijing, Beijing, People's Republic of China

ABSTRACT

By utilising the two-dimensional phase field model with the phenomenological anti-trapping current, the morphological pattern formation of particles within the alloy melt during the initial crystal growth is studied. The results of the numerical simulations elucidate that the two particles progressively converge and interact, ultimately coalescing into a microstructure, and subsequently, the microstructure interface undergoes deformation growth. To be specific, differential growth orientation across various parts of the microstructure interface prompts deformation during the initial crystal growth. The concentration and temperature evolutions of the different parts of the microstructure at different time points during the initial crystal growth are analysed. These findings enhance the comprehension of the fundamental mechanisms underlying the evolution of the microstructure during crystal growth.

ARTICLE HISTORY
Received 26 March 2024
Accepted 11 November 2024

KEYWORDS
Anti-trapping current; initial crystal growth; phase field model; morphological pattern; microstructure

1. Introduction

The formation of morphological patterns during crystal growth is a complicated phase transition question characterised by both multiscale and multiphysics [1–5]. This physical phenomenon has an essential impact within the realm of material science [6–10]. Nucleated particles undergo a transforming development throughout crystal growth[11,12]. They begin with a simple morphological pattern and mature into complex morphologies such as dendritic, columnar, and cellular crystals in the late stage [13]. Numerous experimental investigations into the pattern formation during initial crystal growth have been carried out. Martinez and Flemings [14] conducted a pivotal study on the crystal morphology in the process of crystal growth. The findings showed

CONTACT Ming-Wen Chen chenmw@ustb.edu.cn School of Mathematics and Physics, University of Science and Technology Beijing, Beijing 100083, People's Republic of China; Zidong Wang wangzd@mater.ustb.edu.cn School of Materials Science and Engineering, University of Science and Technology Beijing, Beijing 100083, People's Republic of China

that crystalline particles exhibit an initial spherical morphology, which persists as they continue to grow. Li et al. [15] explored the pattern evolution during initial crystal growth, uncovering the formation of crystalline particles with distinct globular characteristics. Reisi and Niroumand [16] studied the pattern evolution of succinonitrile particles. Their results indicated that under specific conditions, the pattern evolution of the particle initially adheres to a spherical morphology. Chen et al. [17] utilised transmission electron microscopy to research the particle shape evolution during initial crystal growth. They observed the progression in particle shape from spherical to cuboidal, then to petal-like forms, culminating in a division into eight sub-nanoparticles. Research efforts are not only focussed on experimental studies, but the significant advancements have also been made in the theoretical domain. Chen et al. [18,19] explored the growth dynamics of particles within undercooled and alloy melts, respectively, during initial crystal growth, employing matched asymptotic expansion method. Their studies illuminated the phenomenon of local inward and outward growth in a particle, a mechanism instrumental in engendering a petal-like morphology.

Many researchers have conducted extensive research on the interactions between particles and the morphological pattern evolution of the interfaces of the formed microstructures [20–25]. Chang et al. [26] introduced a modified level set method to effectively model the interaction between particles and a solidifying interface. Their approach facilitated the interpretation of experimental results derived from directional solidification studies. Gong et al. [27] studied the interaction between two particles by using phase field model. Glicksman et al. [28,29] studied the microstructural pattern formation of the periodic grain boundary grooves under the influence of capillary field.

However, current theoretical research on this topic is limited, particularly in the fundamental understanding of particle-particle interaction in the initial stage of crystal growth. Here, particle-particle interaction during the initial crystal growth is analysed in depth using a thermodynamic phase field model including an anti-trapping current. The evolution of concentration and temperature in different parts of the microstructure at various time points during the initial stage of crystal growth is analysed.

2. Phase field model

Phase field simulations offer significant advantages in simulating the microstructure evolution [30–44], as they facilitate the simulation of the multi-physics evolution, balancing detail and computational efficiency. This study's numerical simulation is based on the premise that the solute's diffusion within the solid phase is not considered in the computation and that the liquid and solid phases' thermal diffusion coefficients are equal. The introduction of the order parameter, denoted as ϕ, constitutes a foundational concept

that discerns the phase characteristics in terms of both temporal and spatial dimensions. In this model, the variable ϕ is assigned the value of 1 to denote the solid phase, whereas it is assigned the value of -1 to signify the liquid phase. In the transition region between the solid and liquid phases, phase field ϕ undergoes a continuous and smooth variation, seamlessly traversing the entire range from -1 to 1.

The total free energy, $\mathcal{F}$, of the system is expressed as follows:

$$\mathcal{F} = \int_V \left[f(\phi, c, T) + \frac{1}{2}\varpi^2 (\nabla\phi)^2 \right] \mathrm{d}V, \tag{1}$$

where $f(\phi, c, T)$ is the local free energy density, the concentration is c, $\varpi = \varpi_0 A(\boldsymbol{n})$ is the gradient energy, ϖ_0 represents the characteristic interface thickness, and the temperature is T. In the case of two-dimension, the anisotropy function $A(\boldsymbol{n})$, with $\boldsymbol{n}$ as the unit vector in the normal direction of the phase, is defined as follows:

$$A(\boldsymbol{n}) = 1 + \beta \frac{\phi_x^4 - 2\phi_x^2\phi_y^2 + \phi_y^4}{\left|\nabla\phi\right|^4}, \tag{2}$$

where β represents the strength of anisotropy, $\phi_x = \partial\phi/\partial x$ and $\phi_y = \partial\phi/\partial y$ represent the partial derivatives of ϕ with respect to x and y, respectively. Equation (2) is expressed in its canonical form to characterise the anisotropy, as follows:

$$A(\boldsymbol{n}) = 1 + \beta\cos(4\theta),$$

where the angle $\theta = \arctan(\phi_y/\phi_x)$ represents the angle subtended by the vector $\boldsymbol{n}$ with respect to the x-axis.

The phase field model is

$$\Xi_\phi \frac{\partial\phi(\boldsymbol{x}, t)}{\partial t} = -\frac{\delta F(\phi, c, T)}{\delta\phi(\boldsymbol{x}, t)}, \tag{3}$$

$$\frac{\partial c(\boldsymbol{x}, t)}{\partial t} = \nabla\cdot\left(\Xi_c\nabla\frac{\delta F(\phi, c, T)}{\delta c(\boldsymbol{x}, t)} - \boldsymbol{j}_{at}\right), \tag{4}$$

$$\frac{\partial T(\boldsymbol{x}, t)}{\partial t} = \alpha\nabla^2 T(\boldsymbol{x}, t) + \frac{L}{2c_p}\frac{\partial\phi(\boldsymbol{x}, t)}{\partial t}, \tag{5}$$

where L denotes the latent heat, R represents the gas constant, T_M represents the melting point, v_0 denotes the molar volume, α denotes the thermal diffusivity, Ξ_ϕ represents the kinetic mobility, D denotes the solutal diffusivity of the liquid, $\Xi_c = \frac{v_0}{RT_M}Dq(\phi)c$, the function $q(\phi)$ dictates the solute diffusivity behaviour across the diffuse interface and c_p denotes the specific heat. In Equation (5), the solute flux comprises two components: the first term, $-\Xi_c\nabla\frac{\delta F}{\delta c}$, applies Fick's law of diffusion within the liquid phase [45]. The second term, the

phenomenological anti-trapping current, $\frac{\varpi_0}{\sqrt{2}}[1+(1-k)c]\frac{\partial\phi}{\partial t}\frac{\nabla\phi}{|\nabla\phi|}$, as proposed by [46], is designed to counteract spurious solute trapping and suppress unwanted thin-interface effects. This current flows directly from the solid phase into the liquid phase perpendicular to the interface, with a magnitude proportional to both the interface thickness and velocity $\frac{\partial\phi}{\partial t}$ (directed along $-\boldsymbol{n}$). While other terms in the model are derived variationally from a corresponding free energy functional, the anti-trapping current is introduced on a phenomenological basis.

The local free energy density of the alloy, $f(\phi, c, T)$, which exhibits local minima corresponding to the two coexisting phases, is mathematically expressed as the sum of the free energy of the pure material, f_p, and the additional contribution from the presence of solute, f_{AB}. The expression for $f(\phi, c, T)$ is given in the following form

$$\begin{aligned} f(\phi, c, T) &= f_p + f_{AB} \\ &= f(\phi, T_M) + f_T(\phi)\Delta T + T_M\frac{R(c\ln c - c)}{\nu_0} + \overline{\epsilon}c + \Delta\epsilon\frac{c\bar{g}(\phi)}{2}, \end{aligned} \tag{6}$$

where

$$\begin{aligned} f(\phi, T_M) &= \frac{1}{4}H\left(\phi^4 - 2\phi^2\right), \\ f_T(\phi) &= \left.\frac{\partial f(\phi, T)}{\partial T}\right|_{T=T_M} = \frac{RT_M}{\nu_0 m}e^{\left[\frac{1+\bar{g}(\phi)}{2}\ln k\right]}, \end{aligned}$$

where $\Delta T = T - T_M$, $\bar{g}(\phi)$ is an interpolation function with $\bar{g}(\pm 1) = \pm 1$, H is a barrier height and

$$\overline{\epsilon} = \frac{\epsilon_s + \epsilon_l}{2}, \quad \Delta\epsilon = \epsilon_s - \epsilon_l.$$

Equations (4) and (5) are substituted into Equation (1), yielding the following result

$$\begin{aligned} \frac{1}{H\Xi_\phi}\frac{\partial\phi}{\partial t} = \phi - \phi^3 - \frac{R\ln(k)}{2H\nu_0}T_M\bar{g}'(\phi)\left[c - \frac{e^{\left[\frac{1+\bar{g}(\phi)}{2}\ln k\right]}}{m}\Delta T\right] \\ + \varpi_0^2\nabla\cdot\left(A^2\nabla\phi\right) - \varpi_0^2\left[AA'\phi_y\right]_x + \varpi_0^2\left[AA'\phi_x\right]_y, \end{aligned} \tag{7}$$

$$\frac{\partial c}{\partial t} = \nabla\cdot\left(q(\phi)Dc\nabla\left[\ln(c) - \frac{\bar{g}(\phi)}{2}\ln(k)\right] - \boldsymbol{j}_{at}\right), \tag{8}$$

where

$$\bar{g}'(\phi)=\frac{\partial}{\partial\phi}\bar{g}(\phi),\quad A'=\frac{\partial}{\partial\theta}A,\quad q(\phi)=\frac{1}{1+k-(1-k)\phi}(1-\phi),$$
$$\left[AA'\phi_y\right]_x=\frac{\partial}{\partial x}\left(AA'\phi_y\right),\quad \left[AA'\phi_x\right]_y=\frac{\partial}{\partial y}\left(AA'\phi_x\right).$$

$U=\ln\left(\frac{c}{c_\infty}\right)-\frac{1+\bar{g}(\phi)}{2}\ln k$, where c_∞ denotes the concentration far from the interface, corresponding to the solute's original concentration. The expression $e^{\left[\frac{1+\bar{g}(\phi)}{2}\ln k\right]}=\frac{1+k-(1-k)\tilde{g}(\phi)}{2}$ can be employed to derive the limiting condition $\tilde{g}(\pm 1)=\pm 1$, which parallels $\bar{g}(\phi)$. Consequently, Equations (8) and (9) can be reformulated as follows

$$\begin{aligned}\frac{1}{H\Xi_\phi}\frac{\partial\phi}{\partial t}=&\phi-\phi^3-\frac{R(1-k)}{2Hv_0}T_Mc_\infty\tilde{g}'(\phi)\left[e^u-\frac{1}{mc_\infty}\Delta T\right]\\&+\varpi_0^2\nabla\cdot\left(A^2\nabla\phi\right)-\varpi_0^2\left[AA'\phi_y\right]_x+\varpi_0^2\left[AA'\phi_x\right]_y,\end{aligned}\tag{9}$$

$$\frac{\partial c}{\partial t}=\nabla\cdot\left(q(\phi)Dc\nabla u-\boldsymbol{j}_{at}\right),\tag{10}$$

where m is the liquidus slope.

To simplify the model and perform numerical calculations, we utilise dimensionless variables

$$\tilde{c}=\frac{1}{1-k}(e^u-1),\quad \tilde{T}=\frac{1}{L/c_p}(\Delta T-mc_\infty),\quad \tilde{t}=\frac{1}{\kappa_0}t,$$
$$\tilde{x}=\frac{1}{l}x,\quad \tilde{y}=\frac{1}{l}y.$$

Therefore, the following presents the dimensionless model:

$$\begin{aligned}\zeta_\phi\frac{\partial\phi}{\partial t}=&\phi-\phi^3-\lambda\left(1-\phi^2\right)^2(Mc_\infty c+T)\\&+\omega^2\nabla\cdot\left(A^2\nabla\phi\right)-\omega^2\left[AA'\phi_y\right]_x+\omega^2\left[AA'\phi_x\right]_y,\end{aligned}\tag{11}$$

$$\begin{aligned}(1+k)\frac{\partial c}{\partial t}=&\nabla\cdot\left\{(1-\phi)D^*\nabla c+\frac{\omega}{\sqrt{2}}[1+(1-k)c]\frac{\partial\phi}{\partial t}\frac{\nabla\phi}{|\nabla\phi|}\right\}\\&+\frac{\partial}{\partial t}\{\phi[1+(1-k)c]\},\end{aligned}\tag{12}$$

$$\frac{\partial T}{\partial t}=\alpha^*\nabla^2T+\frac{1}{2}\frac{\partial\phi}{\partial t},\tag{13}$$

where

$$\omega = \frac{\varpi_0}{l}, \quad D^* = \frac{D\kappa_0}{l^2}, \quad \alpha^* = \frac{\alpha\kappa_0}{l^2},$$
$$\zeta_\phi = A^2 \times \left\{\frac{1}{Le} + Mc_\infty[1 + (1-k)c]\right\},$$

where λ is a coupling constant, $M = -\frac{mc_p(1-k)}{L}$, ζ_0 is the relaxation time and the Lewis number $Le = \frac{\alpha}{D}$. In Equation (14), the last component on the right-hand side represents the source term connected to the release of latent heat during the crystal formation process. In Equation (12), the term of $(Mc_\infty c + T)$ within the equations signifies the heat-solute driving force inherent in the crystal growth process, and

$$\begin{aligned}
&\omega_0^2 \nabla \cdot \left(A^2 \nabla \phi\right) \\
&\quad = 2\omega_0^2 A \frac{\phi_{xy}(\phi_x^2 - \phi_y^2) - \phi_x \phi_y (\phi_{xx} - \phi_{yy})}{\phi_x^2 + \phi_y^2} \\
&\qquad + \omega_0^2 A^2 \nabla^2 \phi,
\end{aligned} \tag{14}$$

$$\begin{aligned}
\omega_0^2 \left[AA'\phi_y\right]_x = &\frac{16\beta\omega_0^2\phi_y}{\left(\phi_x^2 + \phi_y^2\right)^5} \\
&\times \left\{\beta\phi_x^8\phi_{\mathrm{xx}}\phi_y - 28\beta\phi_x^6\phi_{\mathrm{xx}}\phi_y^3 + 70\beta\phi_x^4\phi_{\mathrm{xx}}\phi_y^5 - 28\beta\phi_x^2\phi_{\mathrm{xx}}\phi_y^7\right. \\
&+ \phi_x^8\phi_{\mathrm{xx}}\phi_y - 4\phi_x^6\phi_{\mathrm{xx}}\phi_y^3 - 10\phi_x^4\phi_{\mathrm{xx}}\phi_y^5 - 4\phi_x^2\phi_{\mathrm{xx}}\phi_y^7 \\
&- 2\beta\phi_x^9\phi_{\mathrm{xy}} + 34\beta\phi_x^7\phi_{\mathrm{xy}}\phi_y^2 - 70\beta\phi_x^5\phi_{\mathrm{xy}}\phi_y^4 + 22\beta\phi_x^3\phi_{\mathrm{xy}}\phi_y^6 \\
&+ 2\phi_x^7\phi_{\mathrm{xy}}\phi_y^2 + 10\phi_x^5\phi_{\mathrm{xy}}\phi_y^4 + 6\phi_x^3\phi_{\mathrm{xy}}\phi_y^6 - 2\phi_x^9\phi_{\mathrm{xy}} \\
&\left.+\beta\phi_{\mathrm{xx}}\phi_y^9 + \phi_{\mathrm{xx}}\phi_y^9\right\},
\end{aligned} \tag{15}$$

$$\begin{aligned}
\omega_0^2 \left[AA'\phi_x\right]_y = &-\frac{16\beta\omega_0^2\phi_x}{\left(\phi_x^2 + \phi_y^2\right)^5} \\
&\times \left\{22\beta\phi_x^6\phi_{\mathrm{xy}}\phi_y^3 - 70\beta\phi_x^4\phi_{\mathrm{xy}}\phi_y^5 + 34\beta\phi_x^2\phi_{\mathrm{xy}}\phi_y^7 + 6\phi_x^6\phi_{\mathrm{xy}}\phi_y^3\right. \\
&+ 10\phi_x^4\phi_{\mathrm{xy}}\phi_y^5 + 2\phi_x^2\phi_{\mathrm{xy}}\phi_y^7 - 28\beta\phi_x^7\phi_y^2\phi_{\mathrm{yy}} + 70\beta\phi_x^5\phi_y^4\phi_{\mathrm{yy}} \\
&- 28\beta\phi_x^3\phi_y^6\phi_{\mathrm{yy}} + \beta\phi_x\phi_y^8\phi_{\mathrm{yy}} - 4\phi_x^7\phi_y^2\phi_{\mathrm{yy}} - 10\phi_x^5\phi_y^4\phi_{\mathrm{yy}} \\
&- 4\phi_x^3\phi_y^6\phi_{\mathrm{yy}} + \phi_x\phi_y^8\phi_{\mathrm{yy}} + \beta\phi_x^9\phi_{\mathrm{yy}} + \phi_x^9\phi_{\mathrm{yy}} - 2\beta\phi_{\mathrm{xy}}\phi_y^9 \\
&\left.- 2\phi_{\mathrm{xy}}\phi_y^9\right\}.
\end{aligned} \tag{16}$$

3. Simulation results and discussion

The Cartesian lattices that constitute the basis for the spatial discretization of Equations (12), (13), and (14) have the same spatial step $\Delta x = 0.01$ in both the x and y directions. An explicit Eulerian strategy with a time step of $\Delta t = \tau_0 = 10^{-5}$ is used to advance the phase field model within the temporal domain. For calculations involving multiple particles, Neumann boundary conditions are employed at the boundaries surrounding the variables ϕ, c, and T to ensure no diffusion across these boundaries. Nuclei with a radius of R are initially positioned close to the computational domain's centre in the model that is being presented. This initial configuration does not consider the nucleation process. Thus, the initial conditions are established to

$$\begin{aligned} (x-x_0)^2+(y-y_0)^2 \le R^2, \quad \phi = 1,\ T = \Delta,\ c = c_\infty, \\ (x-x_0)^2+(y-y_0)^2 > R^2, \quad \phi = -1,\ T = \Delta,\ c = c_\infty. \end{aligned} \tag{17}$$

Table 1 summarises the thermodynamic parameters of Cu-Ni alloy referred to literatures [47–49]. The latent heat, L, the thermal diffusivity, α, and the specific heat capacity, c_p, of Cu-Ni alloy can be calculated via the relations

$$\begin{aligned} L &= c_\infty L_{Ni} + (1-c_\infty)L_{Cu}, \\ \alpha &= c_\infty \alpha_{Ni} + (1-c_\infty)\alpha_{Cu}, \\ c_p &= c_\infty c_p^{Ni} + (1-c_\infty)c_p^{Cu}. \end{aligned} \tag{18}$$

The intricate situations that arise during the evolution process of a system featuring two crystal particles during the initial crystal growth are studied. Figure 1 shows the interaction of two particles at the position shown in the figure during the initial crystal growth. As shown in Figure 1, the two particles progressively converge and interact after nucleation, eventually merging to form a microstructure. The black arrows in the figure indicate the growth direction of the microstructural interface. Upon the formation of the microstructure, parts of the interface of the microstructure exhibit inward growth beyond a critical dimension. In contrast, other parts demonstrate outward growth from the critical dimension. This growing inward leads to rapid deformations near [110], [1$\bar{1}$0], [$\bar{1}$10] and [$\bar{1}\bar{1}$0] in the microstructure, resulting in a

Table 1. Cu-Ni alloy parameters.

Symbol	Meaning	Physical value
T_m^{Cu} (K)	Melting temperature of Cu	1358
T_m^{Ni} (K)	Melting temperature of Ni	1728
L_{Cu} (J · m^{-3})	Latent heat of Cu	1.728×10^9
L_{Ni} (J · m^{-3})	Latent heat of Ni	2.35×10^9
c_p^{Cu} (J · m^{-3} · K^{-1})	Specific heat capacity of Cu	3.96×10^6
c_p^{Ni} (J · m^{-3} · K^{-1})	Specific heat capacity of Ni	5.42×10^6
k	Equilibrium partition coefficient	0.3
α_{Cu} (m^2 · s^{-1})	Thermal diffusivity of Cu	4.2×10^{-5}
α_{Ni} (m^2 · s^{-1})	Thermal diffusivity of Ni	1.55×10^{-5}
D (m^2 · s^{-1})	Diffusivity coefficient	1×10^{-9}

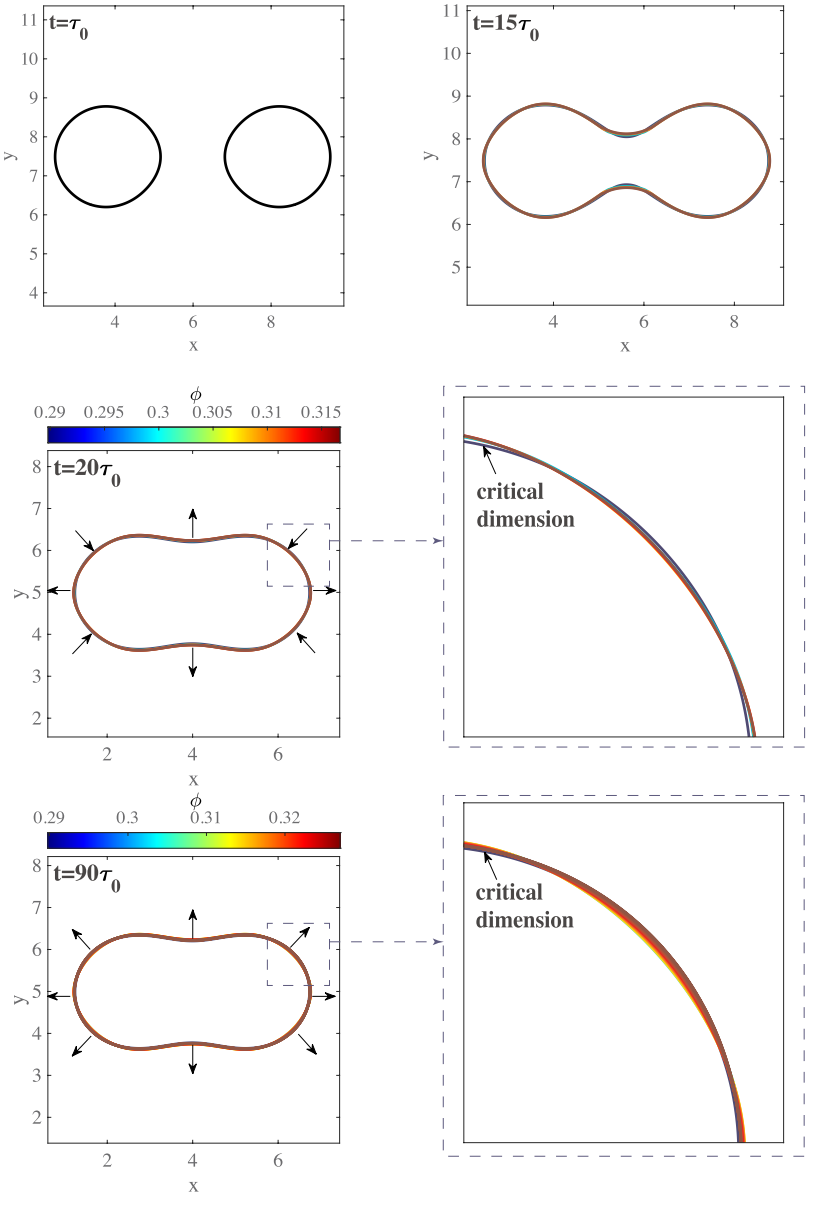

Figure 1. (Color online) The temporal evolution of interaction of two particles during the initial crystal growth.

deforming shape formation, until the growth rate reaches zero. After the inward growth, the microstructure overall exhibits outward growth.

The growth characteristic of the microstructure in this stage is illustrated by the kinetic trajectories at different times, as shown in Figure 2. Initially, the microstructure contracts inward from the boundary of the critical dimension. This inward growth proceeds until reaching a critical point, beyond which the growth direction reverses outward. Following this transition, the microstructure exhibits steady growth without any notable abrupt transformations.

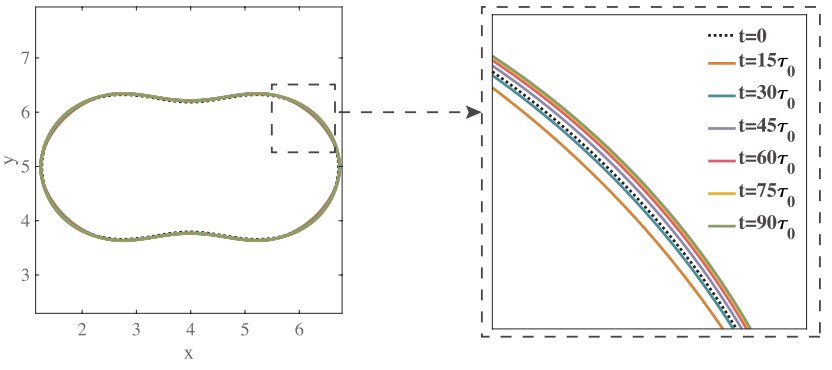

Figure 2. (Color online) The temporal evolution of microstructural deformation during the initial crystal growth.

Figure 3 portrays the variation of concentration along the different parts of the microstructure interface at different times. It is seen that during the initial crystal growth, the concentration along the microstructure interface increases with time and the concentration difference exists between the deformation growth part along the [110] direction at the microstructure interface and the constantly outward growth part along the [010] direction. This phenomenon is further illuminated in Figure 4, which illustrates the concentration variation along the microstructure during the initial crystal growth. This concentration difference between the deformation growth part along the [110] direction at the microstructure interface and the constantly outward growth part along the [010] direction decreases with time until it culminates within a specific time span, denoted as $10\tau_0 < t < 15\tau_0$. As can be seen from Figure 4, after

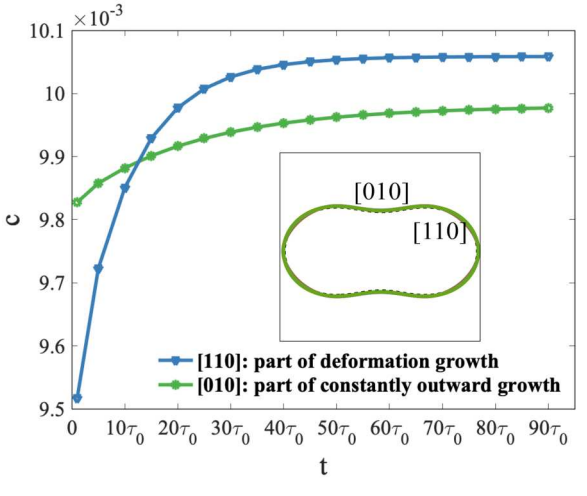

Figure 3. (Color online) The concentration variation of the different parts along the microstructure during the initial crystal growth.

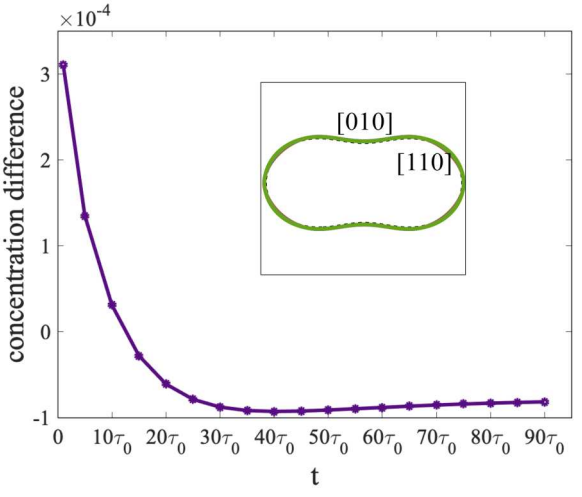

Figure 4. (Color online) The concentration difference between the deformation growth part and part of constantly outward growth along the microstructure during the initial crystal growth.

the concentration difference reaches the minimum, the rates of concentration increase along the different parts of the microstructure interface undergo a gradual decline with time, but the speed size is significantly different. This leads to an increasing concentration difference. It implies that during the initial crystal growth, the concentration along the microstructure interface undergoes complex variation with time, and the rates of concentration increase across distinct parts variate with time.

The temperature variation of the different parts of the microstructure interface at different time points is shown in Figure 5. It can be seen that the temperature along the microstructure interface increases with time and the temperature difference exists between the deformation growth part along the [110] direction at the microstructure interface and the constantly outward growth part along the [010] direction. Furthermore, the temperature difference reaches its maximum value at $t = 15\tau_0$. Before $t = 15\tau_0$, initially, the temperature of the deformation growth part along the [110] direction at the microstructure interface is higher than the constantly outward growth part along the [010] direction. The phenomenon is further illuminated in Figure 6, which illustrates the temperature difference variation along the microstructure interface during the initial crystal growth. In $\tau_0 < t < 15\tau_0$, this temperature difference between the deformation growth part along the [110] direction at the microstructure interface and the constantly outward growth part along the [010] direction increases with time until it culminates at $t = 15\tau_0$. Following the maximum at $t = 15\tau_0$, the temperature difference decreases with time until it approaches zero, culminating in the equilibration of temperatures after $t = 90\tau_0$. It implies that during the initial crystal growth, in $\tau_0 < t < 15\tau_0$, the deformation growth

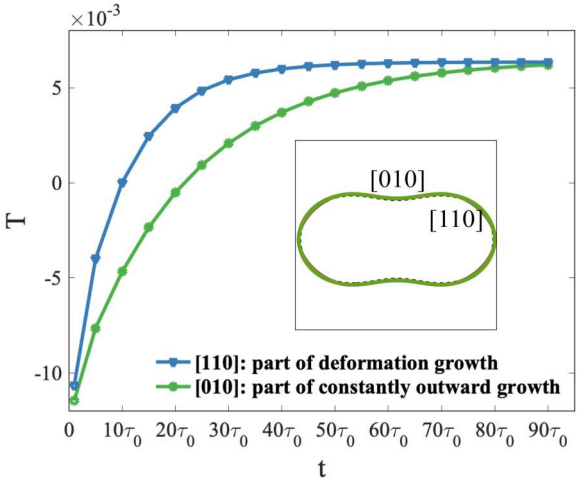

Figure 5. (Color online) The variation of temperature along the different parts of the microstructure interface during the initial crystal growth.

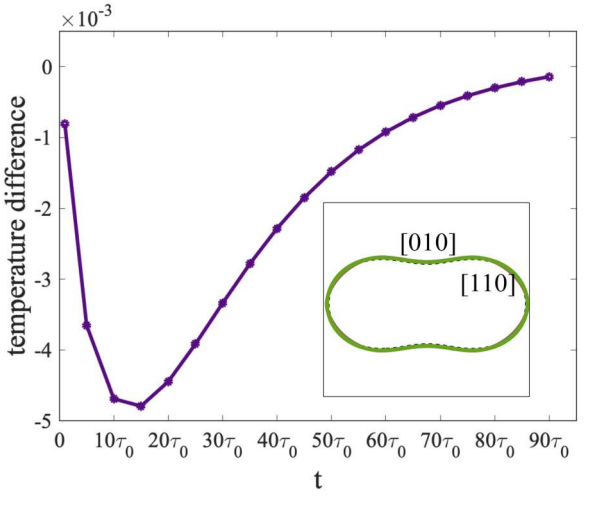

Figure 6. (Color online) The temperature difference between the deformation growth part and part of constantly outward growth along the microstructure during the crystal growth.

part along the [110] direction at the microstructure interface exhibits higher temperatures compared to the constantly outward growth part along the [010] direction. The temperature difference between the deformation growth part along the [110] direction at the microstructure interface and the constantly outward growth part along the [010] direction during the initial crystal growth follows a nuanced pattern: before $t = 15\tau_0$, it increases; after $t = 15\tau_0$, it decreases. Following $t = 15\tau_0$, the deformation growth part along the [110] direction at the microstructure interface display lower rate of temperature

increasing compared to the constantly outward growth part along the [010] direction, leading to a decreased temperature difference.

The intricate situations that arise during the evolution process of a system featuring two crystal particles during the initial crystal growth are studied. Figure 7 shows the interaction of two particles at the position shown in the

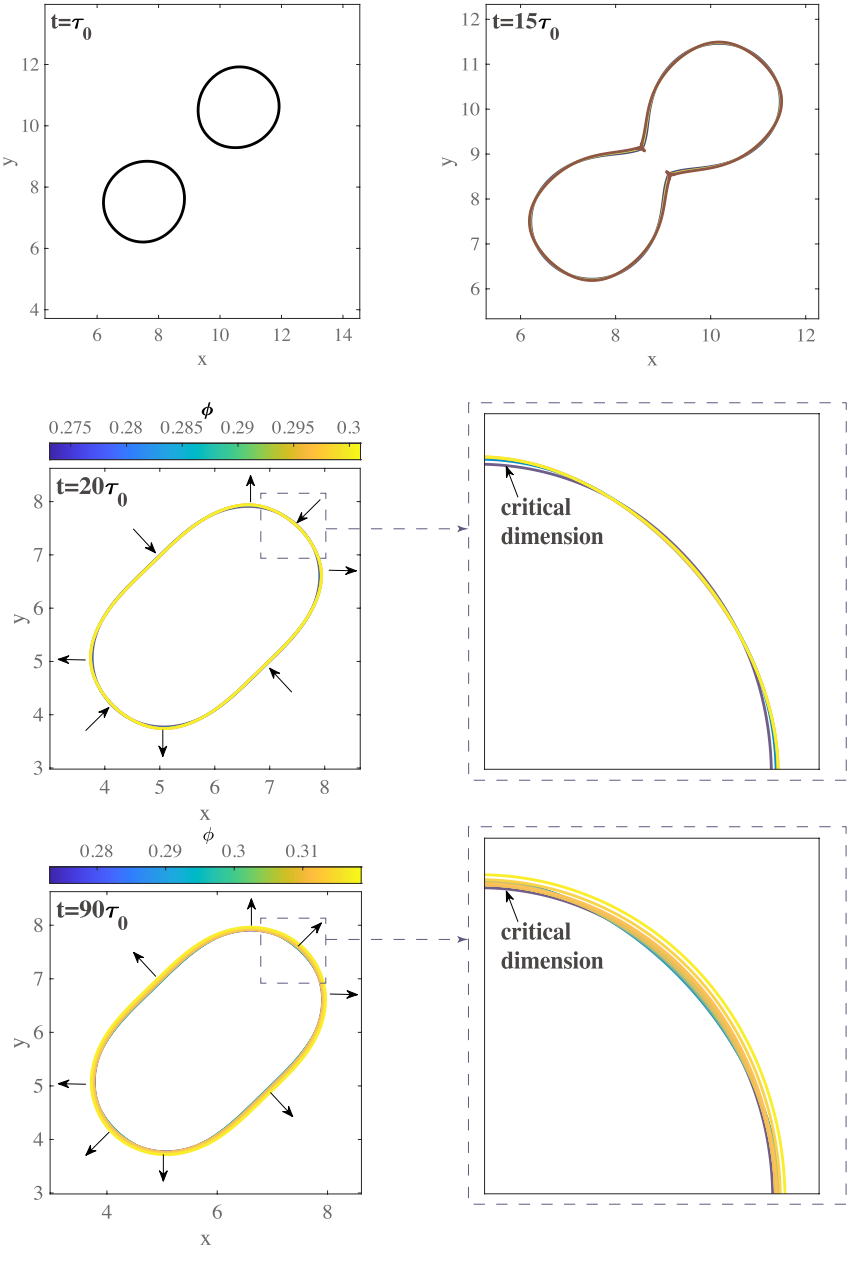

Figure 7. (Color online) The temporal evolution of interaction of two particles during the initial crystal growth.

figure during the initial crystal growth. As shown in Figure 7, the two particles progressively converge and interact after nucleation, eventually merging to form a microstructure. The black arrows in the figure indicate the growth direction of the microstructural interface. Upon the formation of the microstructure, parts of the interface of the microstructure exhibit inward growth beyond a critical dimension. In contrast, other parts demonstrate outward growth from the critical dimension. This growing inward leads to rapid deformations near [110], [1$\bar{1}$0], [$\bar{1}$10] and [$\bar{1}\bar{1}$0] in the microstructure, resulting in a deforming shape formation, until the growth rate reaches zero. After the inward growth, the microstructure overall exhibits outward growth.

The growth characteristic of the microstructure in this stage is illustrated by the kinetic trajectories at different times, as shown in Figure 8. Initially, the microstructure contracts inward from the boundary of the critical dimension. This inward growth proceeds until reaching a critical point, beyond which the growth direction reverses outward. Following this transition, the microstructure exhibits steady growth without any notable abrupt transformations.

Figure 9 illustrates the concentration distribution during the initial crystal growth. The figure demonstrates that there is a concentration difference between the interior and exterior of the microstructure during the initial crystal growth. The microstructure formed during the initial crystal growth is surrounded by a melt of higher concentration.

Figure 10 illustrates the temperature distribution during the initial crystal growth. The figure demonstrates that there is a temperature difference between the interior and exterior of the microstructure during the initial crystal growth. The microstructure formed during the initial crystal growth is surrounded by a melt of higher temperature.

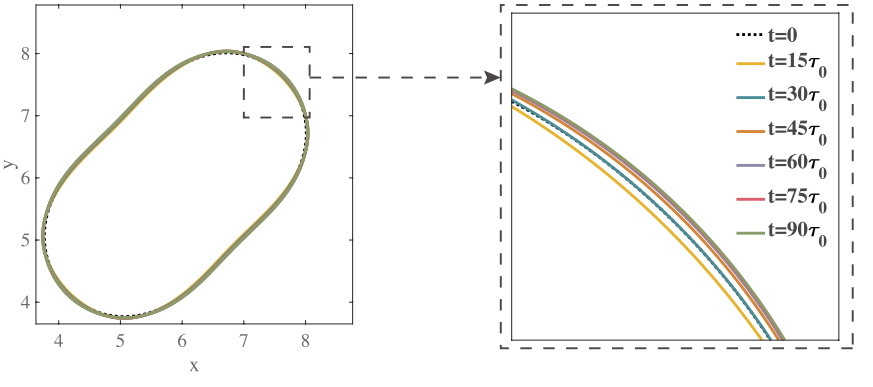

Figure 8. (Color online) The temporal evolution of microstructural deformation during the initial crystal growth.

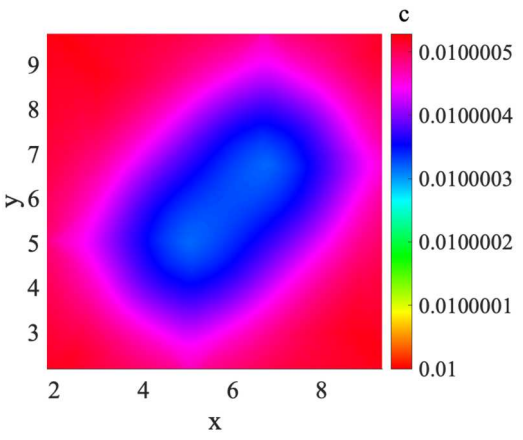

Figure 9. (Color online) The concentration distribution of the microstructure during the initial crystal growth.

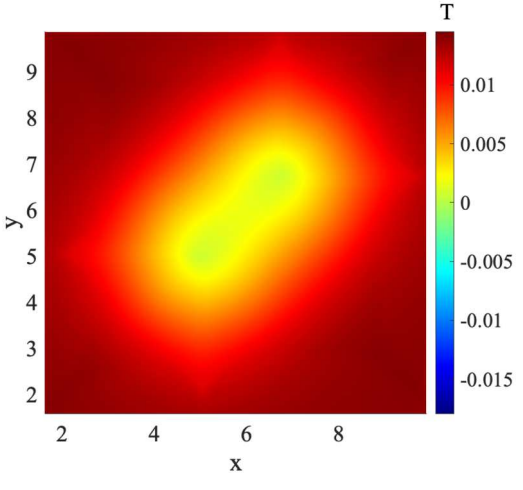

Figure 10. (Color online) The temperature distribution of the microstructure during the initial crystal growth.

4. Conclusions

The particle-particle interaction in an alloy melt during the initial crystal growth are studied using a two-dimensional thermodynamically consistent phase field model with an anti-trapping current. The results of the simulations show that the two particles progressively converge and interact after nucleation, eventually merging to form a microstructure, and then the microstructure interface undergoes deformation growth. Through the analysis of concentration and temperature variations along the microstructure interface at specific time intervals, this study reveals that, during the initial crystal growth, both concentration and temperature exhibit complex fluctuations.

These results will enhance our understanding of the fundamental mechanisms governing the initial crystal growth.

Disclosure statement

No potential conflict of interest was reported by the author(s).

Funding

This research is supported by the National Natural Science Foundation of China (Grant No. 51971031).

ORCID

Nan Liu http://orcid.org/0000-0002-4669-6547

References

[1] H. Kim, S. Ran, E. Mun, H. Hodovanets, M. Tanatar, R. Prozorov, S. Bud'ko, and P. Canfield, *Crystal growth and annealing study of fragile, non-bulk superconductivity in YFe_2Ge_2*, Philos. Mag. 95 (2015), pp. 804–818.

[2] H. Jiang, M.W. Chen, G.D. Shi, T. Wang, and Z.D. Wang, *Effect of anisotropy on deep cellular crystal growth in directional solidification*, Mod. Phys. Lett. B 30 (2016), p. 1650205.

[3] J. Juraszek, K. Rola, M. Daszkiewicz, M. Samsel-Czekała, T. Cichorek, and Z. Henkie, *Crystal growth, low-temperature specific heat, and electronic structure of the filled skutterudite compound $ThOs_4As_{12}$*, Philos. Mag. 100 (2020), pp. 1355–1366.

[4] S. Chinnasami, R. Paulraj, and P. Ramasamy, *Investigation on the bulk crystal growth, crystalline perfection, refractive index and piezoelectric properties of borate single crystals for piezoelectric and electro-optic applications*, Chin. J. Phys. 72 (2021), pp. 616–627.

[5] A. Zhang, B. Jiang, Z. Guo, J. Du, Q. Wang, F. Pan, and S. Xiong, *Solution to multiscale and multiphysics problems: A phase-field study of fully coupled thermal-solute-convection dendrite growth*, Adv. Theory Simul. 4 (2021), p. 2000251.

[6] S. Piana, M. Reyhani, and J.D. Gale, *Simulating micrometre-scale crystal growth from solution*, Nature438 (2005), pp. 70–73.

[7] R.E. Rozas, A.L. Korzhenevskii, R. Bausch, and R. Schmitz, *Periodic layer formation in the growth of dilute binary alloys*, Phys. A 413 (2014), pp. 394–399.

[8] Y. Liu, D. Xu, H. Yu, T. Cui, and L. Li, *Single crystal growth and magnetic properties of Co-doped $ZnNb_2O_6$*, Mod. Phys. Lett. B 33 (2019), p. 1950274.

[9] H. Lai, D. Lu, Z. Xu, N. Zheng, Z. Xie, and Y. Liu, *Organic-salt-assisted crystal growth and orientation of quasi-2D Ruddlesden–Popper perovskites for solar cells with efficiency over 19%*, Adv. Mater. 32 (2020), p. 2001470.

[10] M. Chen, Y. Chen, and Z. Wang, *The reversible inward growth of a particle in an alloy melt induced by anisotropic interface kinetics*, Chin. J. Phys. 89 (2024), pp. 748–760.

[11] G. Zheng, M. Chen, C. Yang, and Z. Wang, *Orientation selection of particles growing in an alloy melt*, Chin. J. Phys. 77 (2022), pp. 10–23.

[12] G. Zheng, M. Chen, C. Yang, and N. Liu, *Effect of anisotropic interface kinetics on morphological pattern of a particle in an undercooled melt*, Chin. J. Phys. 78 (2022), pp. 155–168.
[13] N. Liu, M.W. Chen, M. Zhang, C. Yang, and Z. Wang, *Reversible evolution phenomenon of particle during crystal growth: A phase-field study*, Res. Phys. 56 (2024), p. 107278.
[14] R.A. Martinez and M.C. Flemings, *Evolution of particle morphology in semisolid processing*, Metall. Mater. Trans. A 36 (2005), pp. 2205–2210.
[15] T. Li, X. Lin, and W. Huang, *Morphological evolution during solidification under stirring*, Acta Mater.54 (2006), pp. 4815–4824.
[16] M. Reisi and B. Niroumand, *Initial stages of solidification during semisolid processing of a transparent model material*, Mater. Chem. Phys. 135 (2012), pp. 738–748.
[17] K. Chen, P.A. Korzhavyi, G. Demange, H. Zapolsky, R. Patte, J. Boisse, and Z. Wang, *Morphological instability of iron-rich precipitates in Cu-Fe-Co alloys*, Acta Mater. 163 (2019), pp. 55–67.
[18] M. Chen, Z. Wang, and J.J. Xu, *The effect of anisotropic surface tension on the interface evolution of a particle in the undercooled melt*, J. Cryst. Growth 385 (2014), pp. 115–120.
[19] M.W. Chen, L.Y. Li, and H.M. Guo, *The dynamics of nucleation and growth of a particle in the ternary alloy melt with anisotropic surface tension*, J. Chem. Phys. 147 (2017), p. 084707.
[20] M. Liu, K. Wang, D. Xia, and T. Jiang, *Phase field simulation of Al–Si binary dendritic growth and micro-segregation patterns under convection*, J. Alloys Compd. 589 (2014), pp. 431–435.
[21] X. Zhang, J. Kang, Z. Guo, S. Xiong, and Q. Han, *Development of a Para-AMR algorithm for simulating dendrite growth under convection using a phase-field–lattice Boltzmann method*, Comput. Phys. Commun. 223 (2018), pp. 18–27.
[22] Y. Cai, P. Fang, X. Li, and Y. Xu, *Phase field simulation of dendrite growth in gas atomized binary Al–Ni droplets*, Particuology 50 (2020), pp. 43–52.
[23] Y. Yu, Y. Li, F. Lin, and W. Yan, *A multi-grid cellular automaton model for simulating dendrite growth and its application in additive manufacturing*, Addit. Manuf. 47 (2021), p. 102284.
[24] S. Zhang, C. Li, and R. Li, *Cellular automata-lattice Boltzmann simulation of multi-dendrite motion under convection based on dynamic grid technology*, Mater. Today Commun. 31 (2022), p. 103342.
[25] C. Li, J. Wen, L. Wang, G. Lei, and Q. Chen, *Modeling of solid-air multi-dendrite growth evolution driven by coupled thermal-solute using non-isothermal quantitative phase field method*, Int. Commun. Heat Mass Transfer 145 (2023), pp. 106841.
[26] A. Chang, J.A. Dantzig, B.T. Darr, and A. Hubel, *Modeling the interaction of biological cells with a solidifying interface*, J. Comput. Phys. 226 (2007), pp. 1808–1829.
[27] T.Z. Gong, Y. Chen, Y.F. Cao, X.H. Kang, and D.Z. Li, *Fast simulations of a large number of crystals growth in centimeter-scale during alloy solidification via nonlinearly preconditioned quantitative phase-field formula*, Comput. Mater. Sci. 147 (2018), pp. 338–352.
[28] M.E. Glicksman, P. Wu, and K. Ankit, *Surface Laplacian of interfacial thermochemical potential: its role in solid-liquid pattern formation*, npj Microgravity 7 (2021), p. 41.
[29] M.E. Glicksman, P. Wu, and K. Ankit, *Periodic grain boundary grooves: Analytic model, formation energies, and phase-field comparison*, J. Phase Equilib. Diffus. 43 (2022), pp. 718–737.

[30] N. Provatas and K. Elder, Phase-field Methods in Materials Science and Engineering, John Wiley & Sons, Weinheim, 2011.
[31] I. Steinbach, L. Zhang, and M. Plapp, *Phase-field model with finite interface dissipation*, Acta Mater.60 (2012), pp. 2689–2701.
[32] L. Liang and L.Q. Chen, *Nonlinear phase field model for electrodeposition in electrochemical systems*, Appl. Phys. Lett. 105 (2014), p. 263903.
[33] T. Philippe, D. Erdeniz, D. Dunand, and P. Voorhees, *A phase-field study of the aluminizing of nickel*, Philos. Mag. 95 (2015), pp. 935–947.
[34] M. Javanbakht and V.I. Levitas, *Phase field simulations of plastic strain-induced phase transformations under high pressure and large shear*, Phys. Rev. B 94 (2016), p. 214104.
[35] J. Zhang, Z. Chen, C. Cheng, and Y. Wang, *A phase field crystal model simulation of morphology evolution and misfit dislocation generation in nanoheteroepitaxy*, Mod. Phys. Lett. B 31 (2017), p. 1750283.
[36] A. Finel, Y. Le Bouar, B. Dabas, B. Appolaire, Y. Yamada, and T. Mohri, *Sharp phase field method*, Phys. Rev. Lett. 121 (2018), p. 025501.
[37] J.Y. Shao and C. Shu, *Simulation of interfacial waves of two-layer flows through phase field lattice Boltzmann method*, Mod. Phys. Lett. B 32 (2018), p. 1840056.
[38] Q. Wang, G. Zhang, Y. Li, Z. Hong, D. Wang, and S. Shi, *Application of phase-field method in rechargeable batteries*, npj Comput. Mater. 6 (2020), p. 176.
[39] Y. Feng, J. Fan, and J. Li, *Endowing explicit cohesive laws to the phase-field fracture theory*, J. Mech. Phys. Solids 152 (2021), p. 104464.
[40] L. Du, R. Tian, T. Shi, and Y. Cao, *Liquid phase stratification induced by large temperature gradient during spinodal decomposition in Fe–Cr alloys: A phase-field study*, Mod. Phys. Lett. B 35 (2021), p. 2150374.
[41] J. Clayton, R. Leavy, and J. Knap, *Phase field mechanics of residually stressed ceramic composites*, Philos. Mag. 102 (2022), pp. 1891–1944.
[42] D. Liu, J. Wang, H.M. Jafri, X. Wang, X. Shi, D. Liang, C. Yang, X. Cheng, and H. Huang, *Phase-field simulations of vortex chirality manipulation in ferroelectric thin films*, npj Quant. Mater. 7 (2022), p. 34.
[43] C.S. Zhu, Y. Lei, P. Lei, Z.H. Gao, and B.R. Zhao, *Phase field simulation of single bubble behavior under magnetic field*, Chin. J. Phys. 89 (2024), pp. 820–833.
[44] R. Acar, *A topology constrained phase field model*, J. Comput. Phys. 498 (2024), p. 112664.
[45] A. Mullis, J. Rosam, and P. Jimack, *Solute trapping and the effects of anti-trapping currents on phase-field models of coupled thermo-solutal solidification*, J. Cryst. Growth 312 (2010), pp. 1891–1897.
[46] A. Karma, *Phase-field formulation for quantitative modeling of alloy solidification*, Phys. Rev. Lett.87 (2001), p. 115701.
[47] I. Loginova, G. Amberg, and J. Ågren, *Phase-field simulations of non-isothermal binary alloy solidification*, Acta Mater. 49 (2001), pp. 573–581.
[48] W. Kurz and D. Fisher, Fundamentals of Solidification, Trans Tech Publications, Aedermannsdorf, 1992.
[49] A. Mullis and R. Cochrane, *A phase field model for spontaneous grain refinement in deeply undercooled metallic melts*, Acta Mater. 49 (2001), pp. 2205–2214.

Philosophical Magazine

ISSN: 1478-6435 (Print) 1478-6443 (Online) Journal homepage: www.tandfonline.com/journals/tphm20

On the mechanism of shear-coupled grain boundary migration in FCC crystals

Ritu Verma, Dmitri A. Molodov & Andriy Ostapovets

To cite this article: Ritu Verma, Dmitri A. Molodov & Andriy Ostapovets (2026) On the mechanism of shear-coupled grain boundary migration in FCC crystals, Philosophical Magazine, 106:7, 686-698, DOI: 10.1080/14786435.2025.2586373

To link to this article: https://doi.org/10.1080/14786435.2025.2586373

PHILOSOPHICAL MAGAZINE
2026, VOL. 106, NO. 7, 686–698
https://doi.org/10.1080/14786435.2025.2586373

Taylor & Francis
Taylor & Francis Group

On the mechanism of shear-coupled grain boundary migration in FCC crystals

Ritu Verma [a,b,c*], Dmitri A. Molodov [d,e] and Andriy Ostapovets [a]

[a]Department of Experimental Studies and Modelling of Structure, Institute of Physics of Materials, Czech Academy of Sciences, Brno, Czech Republic; [b]Central European Institute of Technology, Brno University of Technology, Brno, Czech Republic; [c]Institute of Physics, Czech Academy of Sciences, Prague, Czech Republic; [d]Institute for Physical Metallurgy and Materials Physics, RWTH Aachen University, Aachen, Germany; [e]Faculty of Advanced Science and Technology, Kumamoto University, Kumamoto, Japan

ABSTRACT

One of the possible mechanisms of metal plasticity is shear-coupled migration of grain boundaries under applied mechanical stress. Several different approaches to the description of shear-coupled migration of grain boundaries and to the prediction of the coupling factor exist in the literature. Some of them are based on the solution of Frank–Bilby equation and consideration of grain boundary (GB) dislocation content; other is based on consideration of disconnection glide along the GB. The first approach describes the boundary as an array of dislocations; the second one considers the glide of disconnection along a dislocation-free boundary. Despite the existence of opinions that these approaches are incompatible, we demonstrate internal interrelation between them by consideration of shear-coupled migration of Σ3(111) boundary in face-centred cubic copper. It is demonstrated that there is no contradiction between approaches and their combination can help to understand the physical mechanisms of shear-coupled boundary migration.

ARTICLE HISTORY
Received 7 April 2025
Accepted 20 October 2025

KEYWORDS
Grain boundary; coupling factor; Cu; migration

Introduction

Shear-coupled grain boundary (GB) migration is an important deformation mechanism in a variety of metallic materials. The Σ3 twin boundary (TB) is a special type of GB in face-centred cubic (FCC) metals. The migration of the Σ3 boundary has attracted substantial interest due to its impact on mechanical properties such as strength, ductility, and fatigue resistance. The Σ3 TB can undergo shear-coupled migration, especially under applied stress. During this process, the boundary migrates by coupling with an applied shear, which allows the material to accommodate plastic deformation.

Recent advancements in computational materials science have provided more in-depth atomic-level knowledge into shear-coupled GB migration, particularly through MD simulations that reveal how partial dislocations drive the migration process [1–8].

CONTACT Andriy Ostapovets ostapov@ipm.cz Department of Experimental Studies and Modelling of Structure, Institute of Physics of Materials, Czech Academy of Sciences, Zizkova 513/22, Brno 61600, Czech Republic
*Present address: Institute of Scientific Computing, TU-Dresden, Dresden, Germany

The response of the GB to the applied stress depends on its dislocation content [9]. There are different approaches available for the description of the migration-shear coupling mechanisms and prediction of the coupling factor. The classical approach describes the boundary as consisting of an array of intrinsic dislocations [10–12].

Dislocation content of such grain boundaries in connection with migration-shear coupling can be predicted by the geometrical model of coupling derived from the Frank–Bilby (F-B) equation and can serve for the calculation of the migration-shear coupling factors as described, for instance, by Molodov and Molodov [13]. Another approach to solving the migration-shear coupling problem can be called as 'disconnection approach'. The disconnection is a crystallographic defect that combines dislocation and interfacial steps. It can be characterised by Burgers vector and step heights [14]. Boundary migration is mediated by glide of the steps on the boundaries in this case. In general, predictions of both approaches are not necessarily the same.

It is commonly accepted that the mentioned models do not have equal physical basis. The F-B approach has value due to its simplicity and geometric transparency, but it is a heuristic model with known limitations. For example, a coherent TB exhibits no elastic distortion in the vicinity of the boundary, suggesting that, strictly speaking, there are no line defects present. The F-B approach forces one to include dislocations to account for the misorientation, even if those dislocations produce no elastic fields. This contradiction is rationalised using the concept of continuous distributions of dislocations that generate no elastic strain. Although this fact can be mathematically defensible, it invokes doubts about the physical realism of the F-B framework for such boundaries. In contrast, the disconnections are real defects: their dislocation character distorts the lattice, and their steps move under applied stress.

It was demonstrated previously that experimentally observed coupling factor cannot be derived in many cases from GB dislocation content obtained from the single solution of the F-B equation [13]. The correct value can be obtained only by mixing different solutions.

The current work provides a theoretical analysis of Σ3 boundary migration in Cu on the basis of atomistic simulations. The coupling factor is calculated by considering the dislocation content of grain boundaries. It is demonstrated that the physical mechanism resulting in the mixing of several F-B equation solutions is the gliding of the disconnection step along the boundary. It is worth noting that such mixing was considered in previous literature, however, as more or less purely a mathematical trick, and its physical mechanism was unclear. Present studies shed light on the physical mechanism and provide the link between the disconnection approach and other approaches for the predictions of the shear-migration coupling factor.

Methodology

Theoretical framework shear-coupled TB migration

Normal GB motion is often coupled with tangential grain translation, leading to shear deformation, and conversely, applied shear stress can induce GB motion. The effectiveness of the shear stress is given in terms of coupling factor (C.F.) β, which is the ratio of

shear s (lateral displacement of grains) to the normal displacement d of the GB

$$\beta = \frac{s}{d} = \frac{v_t}{v_n} \tag{1}$$

where v_t is the tangential velocity of the grains and v_n is the normal velocity of the migrating GB. Cahn et al. theory [12, 15] predicts that the coupling factor depends on the geometry of the GB, commonly described by the rotation axis and the misorientation angle.

GB dislocation content from solution F-B equation: alternative solutions

Frank–Bilby equation is a continuum equation whose solution defines the dislocation content of grain boundaries. It relates the misorientation between two grains to the Burgers vector content of the dislocations in the boundary [16]. The equation is as follows:

$$\boldsymbol{B} = (\boldsymbol{R}_{\boldsymbol{T}}^{-1} - \boldsymbol{I})\boldsymbol{p} \tag{2}$$

where $\boldsymbol{I}$ is the identity matrix, $\boldsymbol{R}_{\boldsymbol{T}}$ is the rotation matrix, $\boldsymbol{p}$ is a unit vector in the GB plane and $\boldsymbol{B}$ is the Burgers vector of a defect called a 'surface dislocation' representing a grain boundary. For symmetric tilt grain boundaries, the equation simplifies the task of identifying the suitable dislocation configuration that meets the geometric limitations dictated by the grain misorientation.

To determine the shear produced by the migrated boundary, Cahn et al. used the idea of surface dislocation in their coupling model. They assumed that the surfaces dislocation with Burgers vector $\boldsymbol{B}$ slips in the direction $\boldsymbol{\eta}_2$ in a plane (K_2) that is invariant to the simple shear caused by the migrating boundary and produces shear in that direction. Therefore, $\boldsymbol{B} = B\hat{\boldsymbol{\eta}}_2$ with $\hat{\boldsymbol{\eta}}_2$ being a unit vector parallel to the slip direction of the surface dislocation. Then, a subsequent rotation around the shear plane normal is needed to smoothly align the lattice of one crystal with another.

In order to calculate the coupling factor, consider the solutions for $\boldsymbol{B}$ that satisfies the condition for simple shear along the boundary plane in $\boldsymbol{\eta}_1$ direction that is perpendicular to the boundary plane normal. The C.F. can be calculated as follows:

$$\beta = \frac{B}{\hat{\boldsymbol{\eta}}_2 . \hat{\boldsymbol{m}}_{\boldsymbol{K}_1}} \tag{3}$$

where $\hat{\boldsymbol{m}}_{\boldsymbol{K}_1}$ is the unit normal of the shear plane K_1. Equation (3) predicts the C.F. for both high and low-angle misorientations.

The coupling factor is determined by the GB crystallography and can take either positive or negative values depending on the mode of migration. In Cahn model, Burgers vector can be parallel to either <001> or <110> directions which corresponds to two distinct coupling modes [15]. The two dominant shear coupling modes are given by $\beta_1 = 2\tan\left(\frac{\theta}{2}\right)$ and $\beta_2 = -2\cot\left(\frac{\theta}{2}\right)$, where θ is the misorientation angle of the GB. These modes correspond to distinct dislocation structures that accommodate shear-coupled migration.

Later, Suzuki and Mishin [17] confirmed the theoretical predictions through molecular dynamics (MD) simulations in metals like Ni, Al and Cu. Their work showed that GB migration is often accompanied by shear, but deviations from the theoretical predictions were also observed [18]. Straightforward application of the expressions for the coupling factor derived based on the geometric model described by Homer et al. [18] failed to reproduce the correct β values known from the literature in many practically important cases, e.g. for the shear produced by migrating twin boundaries in both FCC and hexagonal close packed crystal structures [13]. It was demonstrated previously that the experimentally observed coupling factor cannot be derived from the GB dislocation content obtained from the single solution of the F-B equation. In many cases, the correct value can be obtained only by mixing of two solutions.

Molodov and Molodov [13] proposed a generalised formula for the calculation of the coupling factor for GBs over different crystal structures.

$$\beta_\mu = 2\mu \tan\left(\frac{\theta_c}{2}\right) - 2(1-\mu)\tan\left(\frac{\frac{2\pi}{n} - \theta_c}{2}\right) = \mu\beta_1 + (1-\mu)\beta_2 \tag{4}$$

where θ_c is the smallest tilt angle (the lowest misorientation angle of a pure tilt description of the boundary), μ is the weighting factor that is introduced to constitute the balance between two elementary coupling modes (with values typically limited to simple rational numbers 0, 2/3, 1/2, 3/4, 1), β_1 and β_2 are coupling factors of the elementary modes, n is the order of rotational symmetry of the tilt axis which is associated with tilt angle θ_c. The selection of μ depends on the combination of arrays of dislocations with different Burgers vectors for shear-coupled boundary migration. The μ factor describes the formal balance between arrays of dislocations of different Burgers vectors. Therefore, according to Equation (4), the coupling factor for a given GB or TB is calculated from a combination of two elementary coupling modes. One elementary mode corresponds to the formal description of GB with the tilt angle θ_c, while the other corresponds to the tilt angle $\frac{2\pi}{n} - \theta_c$.

Simulation methods

The Σ3(111) coherent TB in FCC Cu was generated using two Python-based scripts, csl_generator.py and gb_generator.py. [19]. The simulation block has dimensions of 12.38742 nm × 1.2866 nm × 35.58318 nm and contains 24,000 atoms. The orientation of the block is the following: x axis is aligned with [111], y axis with $[1\bar{1}0]$ and the z axis along with$[11\bar{2}]$. OVITO [20] was used for visualisation. Periodic boundary conditions were applied in the y direction; free boundary conditions were applied in z direction and surface atoms in x were fixed to allow application of strain to the simulation block. The initial Σ3 TB structure was relaxed in LAMMPS [21] by using conjugate gradient methods. To initiate the nucleation of twinning disconnections, shear strain was applied in the z-x plane. The strain (ε_{zx}) was increased with value $\varepsilon_{zx} = 0.00007142$. Upon applying the shear, the disconnection moved in a positive z direction. The embedded atom method (EAM) potential for the Cu developed by Mendelev et al. [22] was used to perform simulation in this work.

Burgers circuit formulation

Instead of the solution of the F-B equation, we perform direct measurement of the dislocation content of GB by drawing of Burgers circuit. The application of this method is analogous to the solution of the F-B equation [15]. However, this method can be applied to the straight boundary as well as to the boundary with a step. In contrast, the F-B was derived for a straight boundary. The idea of the Burgers circuit is the following. One can draw a closed circuit in the crystal around the defect and compare it with an identical circuit drawn in the reference crystal without any defects. The circuit in the reference crystal can demonstrate closure failure. This closure failure corresponds to the Burgers vector of the dislocation inside the circuit in the faulted crystal. In general, the circuit can be drawn in different ways. Therefore, one has to choose some convention to be consistent in the definition of the Burgers vector. One of the commonly used conventions is the so-called right-hand/finish-start (RH/FS) convention. In this case, two rules are implied by the Burgers circuit construction. First, when viewing along the dislocation line, which defines the positive line sense or direction of dislocation, the circuit is taken in a clockwise manner. Second, the Burgers vector is taken to run from the end to the start point of the reference circuit in the perfect crystal. The result is also dependent on the selection of reference crystals. This selection can be done in different ways if the dislocation content of the GB is analysed. For instance, the ideal lattice of one of the adjacent grains separated by a boundary can be used as a reference. Besides, a bicrystal can also be considered in this role. The latter case is traditionally used for the characterisation of disconnections. It is important to be consistent in the selection of the reference crystal when characterising the dislocation content of the GB.

There is also another complication in reproducing the Burgers circuit in the reference crystal when the circuit is drawn around the GB segment. The Burgers circuit is drawn inside of two grains with different orientations. However, it should be reproduced in the reference single crystal. One has to assume some orientation relationship between both grains and reference lattice to be able to do this. Due to crystal symmetry, this relationship can be selected in various crystallographically equivalent ways. However, each selection will result in a different description of the dislocation content.

In the present study, we compare the results of such analysis for two symmetrically equivalent descriptions of $\Sigma 3(111)$ boundary. This boundary can be equivalently described as either (a) $109.5°\langle \bar{1}10\rangle$ tilt GB or (b) $70.5°\langle 1\bar{1}0\rangle$ tilt GB. We will refer to these descriptions as Description 1 (D1) and Description 2 (D2), respectively. Besides, we provide comparison with the traditional analysis of Burgers circuit around disconnection with using of dichromatic pattern.

Results and discussion

Dislocation content of $\Sigma 3(111)$ TB

Figure 1(a) shows a closed Burgers circuit constructed in right-hand screw sense around some segment of Σ3 TB with one period length. This circuit is reproduced in the reference lattice in Figure 1(b) for the cases D1 and D2. The closure failure $\overrightarrow{FS}$ corresponds to the Burgers vector contents of the boundary segments inside the Burgers circuit. The

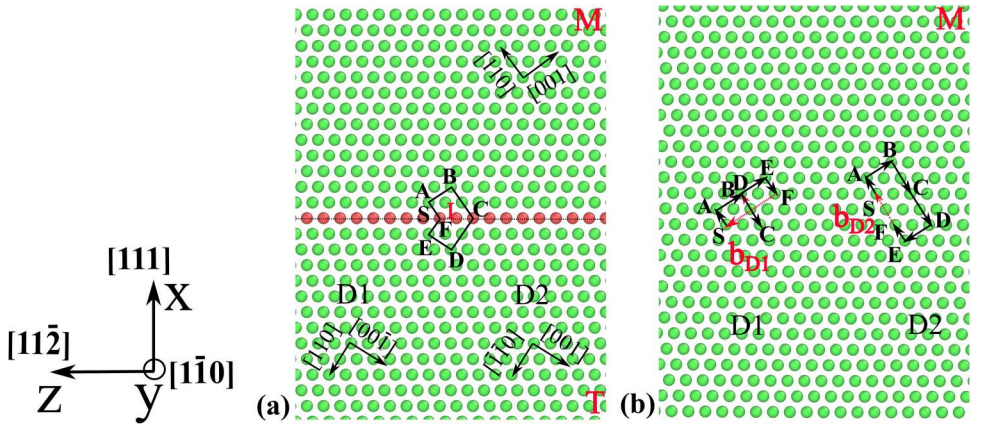

Figure 1. (a) Representation of Burgers circuits for Σ3(111) TB of Cu. The closed circuit ***SABCDEF*** is constructed around segment of the TB. (b) The Burgers circuits shown in (a) reproduced in the reference lattice of the parent crystal (M) for two symmetrically equivalent descriptions of (a) 109.5°⟨$\bar{1}$10⟩ tilt GB, i.e. D1 and (b) 70.5°⟨1$\bar{1}$0⟩ tilt GB, i.e. D2 for Σ3 TB, respectively.

observed closure failure for D1 description with 109.5°⟨$\bar{1}$10⟩ is $\boldsymbol{b}_{D1} = 2[00\bar{1}]$. The Burgers vector content for the periodical CTB segment is equal to $2[00\bar{1}]$. Consequently, the TB can be represented by an array of dislocations with Burger's vector of $2[00\bar{1}]$. On the other hand, the Burgers vector content for the D2, i.e. 70.5°⟨1$\bar{1}$0⟩ misorientation is $\boldsymbol{b}_{D2} = [110]$. Hence, the same CTB can be approximated by an array of dislocation with such Burgers vector.

Dislocation content of Σ3(111) TB with disconnections

The boundary begins to migrate after application of external strain to the simulation block. The migration is mediated by nucleation of mobile steps in the boundary. These steps are disconnections, i.e. interfacial defects with step and dislocation nature. The disconnection produces step with a height equal to one interplanar distance. Such a step can glide along the interfaces under applied stress and mediate interface migration.

The relaxed structure of Σ3(111) TB with disconnections is shown in Figure 2(a). A closed Burgers circuit $S'A'B'C'pD'E'F'$ constructed around the stepped segment of the boundary is shown in Figure 2(a) in order to determine the Burgers vector content of the step. The circuit starts at point S' and ends at point F'.

The circuit in Figure 2(a) is reproduced in the reference crystal lattice for two symmetrically equivalent Descriptions, i.e. D1 and D2 in Figure 2(b). The dislocation content obtained from the flat segment (Figure 1(b) for D1 and D2) and around disconnection (Figure 2(b) for D1 and D2) are summarised in Table 1. The Burgers vector contents shown in Figure 2(b) are denoted as $\boldsymbol{b}^*_{D1}$ and $\boldsymbol{b}^*_{D2}$, for D1 and D2, respectively.

It can be seen that the Burgers vector content of 1 period of perfect Σ3(111) CTB is equal to $2[00\bar{1}]$ and [110] for D1 and D2, respectively. The Burgers vector content around the step is equal to $\left([00\bar{1}] + \frac{1}{2}[110]\right)$ and $\left([001] + \frac{1}{2}[110]\right)$ for D1 and D2, respectively.

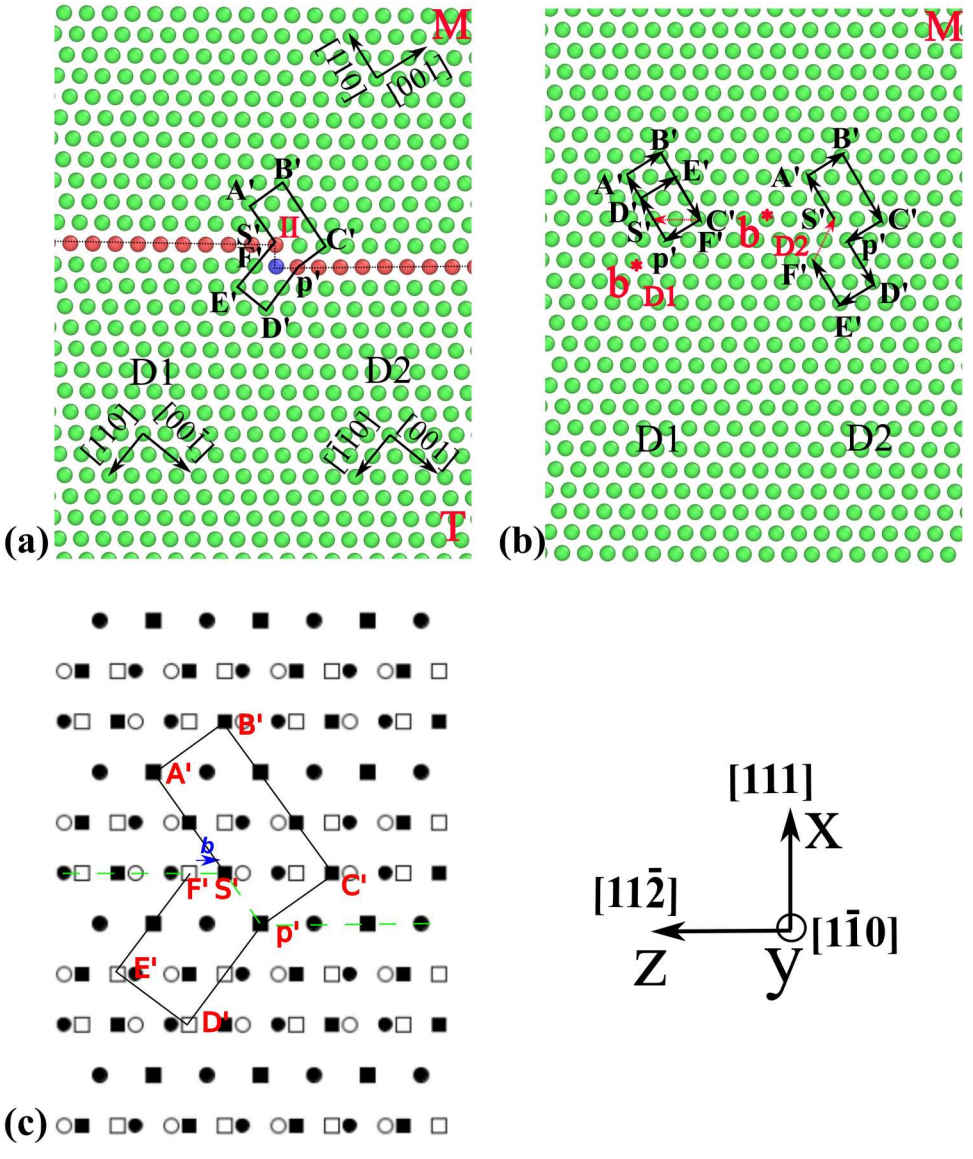

Figure 2. (a) Disconnection in the Σ3(111) TB of Cu obtained from atomistic simulation. Burgers circuit (***S′A′B′C′pD′E′F′***) has been drawn around a one-layer step for Σ3 (111) TB. (b) The Burgers circuits shown in (a) reproduced in the reference lattice of the parent crystal (M) for two symmetrically equivalent descriptions of 109.5°⟨$\bar{1}$10⟩ tilt GB, i.e. D1 and 70.5°⟨1$\bar{1}$0⟩ tilt GB, i.e. D2 for Σ3 TB. (c) The Burgers circuits shown in (a) reproduced in dichromatic pattern. The dichromatic pattern is constructed as a superposition of parent (black symbols) and twin (white symbols) crystal lattices. The dichromatic pattern can be treated as a reference state, where closure failure of the Burgers circuit can be observed.

Therefore, it can be concluded that the Burgers vector content of steps can be described by dislocation contents which correspond to a combination/mixing of dislocations corresponding to the two descriptions of the same boundary. The step length

Table 1. Calculated closure failure for flat Σ3 (111) TB and for disconnection step.

Σ3(111)			
Circuit *SABCDEF*		Circuit *S′A′B′C′pD′E′F′*	
$D1_{\Sigma3(111)}$ $\boldsymbol{b}_{D1} = 2[00\bar{1}]$	$D2_{\Sigma3(111)}$ $\boldsymbol{b}_{D2} = [110]$	$D1_{\Sigma3(111)}$ $\boldsymbol{b}^*_{D1} = [00\bar{1}] + \frac{1}{2}[110]$	$D2_{\Sigma3(111)}$ $\boldsymbol{b}^*_{D2} = [001] + \frac{1}{2}[110]$

along the boundary is equal to one-half of the TB period in the $[\bar{1}\bar{1}2]$ direction. Consequently, for $D1$ and $D2$, the mixing ratio of the dislocations corresponding to the different descriptions is $\frac{1}{2}:\frac{1}{2}$, i.e. there is an equal proportion of dislocations of both types in assembling the disconnection step.

The Burgers vector of disconnection derived from the dichromatic pattern in Figure 2 (c) is $\boldsymbol{b} = \frac{1}{6}[\bar{1}\bar{1}2]$, and the step height is equal to $H = \sqrt{3}a/3$, where a is the lattice parameter.

Operating coupling modes and determining the coupling factors

Let's calculate the possible coupling factors on the basis of the GB dislocation content obtained in the previous chapter. The shear s, which would be produced by migration of disconnection with Burgers vector $\boldsymbol{b}$ shown in Figure 2(c), is obviously

$$s = \frac{\boldsymbol{b}}{H} = \frac{\sqrt{2}}{2} \tag{5}$$

This value agrees with the shear observed in experiment [23]. Equation (5) yields the absolute value of the shear. The sign of the Burgers vector depends on the convention used. Consequently, the sign of shear has to be deduced from its physical meaning. The motion of the step in Figure 2 to the right converts the upper crystal into the lower one. This means that, during such a conversion, the black atoms (Figure 2(c)) are displaced to the left. This corresponds to a negative shear value in the upper crystal, i.e. $\beta = -\sqrt{2}/2$.

The application of the F-B approach and the calculation of the coupling factors corresponding to Description 1 and Description 2 of the Σ3 (111) boundary is more complicated. Equation (3) can be used to calculate the C.F. related to the migration of dislocation arrays. The result is presented in Table 2. Clearly, β for both descriptions do not agree with the experimental value.

Table 2. Coupling factors for different descriptions of flat Σ3(111) boundary.

	D1	D2
$\hat{\boldsymbol{\eta}}_2$	$[00\bar{1}]$	$\frac{1}{\sqrt{2}}[110]$
$\hat{\boldsymbol{m}}_{\boldsymbol{K}_1}$	$\frac{1}{\sqrt{3}}[111]$	$\frac{1}{\sqrt{3}}[111]$
$\lvert\boldsymbol{B}\rvert$	$\frac{2\sqrt{2}}{\sqrt{3}}$	$\frac{2}{\sqrt{3}}$
$\hat{\boldsymbol{\eta}}_2.\hat{\boldsymbol{m}}_{\boldsymbol{K}_1}$	$-\frac{1}{\sqrt{3}}$	$\frac{2}{\sqrt{6}}$
Coupling factor β	$-2\sqrt{2}$	$\sqrt{2}$

$\lvert\boldsymbol{B}\rvert$ – Burgers vector content per unit length of GB.

However, one should consider that the dislocation content of the steps is $[00\bar{1}] + \frac{1}{2}[110]$ and $[001] + \frac{1}{2}[110]$ for D1 and D2, respectively. These contents can be interpreted as the simultaneously acting elementary coupling modes $[00\bar{1}]$ and $[110]$ (corresponding to modes of flat boundary). The produced shear s (coupling factor) is then the averaged coupling factor of these modes, similar to Equation (4), i.e.

$$s'_{\Sigma 3(111)} = \beta_{[00\bar{1}]+\frac{1}{2}[110]} = \frac{1}{2}\beta_{[00\bar{1}]} + \left(1 - \frac{1}{2}\right)\beta_{[110]} = -0.707 \tag{6}$$

and

$$s''_{\Sigma 3(111)} = \beta_{[001]+\frac{1}{2}[110]} = \frac{1}{2}(-\beta_{[00\bar{1}]}) + \left(1 - \frac{1}{2}\right)\beta_{[110]} = 2.121 \tag{7}$$

As can be seen, the weight coefficient $\mu = \frac{1}{2}$ in this case. The shear values of the two modes of Σ3(111) TB in Cu are summarised in Table 3. The value predicted by Equation (6) matches exactly with the twinning shear known from the literature [13, 23].

The prediction of shear, which is coupled with GB migration, depends on the method used and can yield different results. A GB can have a variety of dislocation structures based on the symmetry descriptions, and each structure corresponds to a specific coupling mode. While all modes are theoretically possible, experiments show that only one or a few occur. The results of the above analysis to determine the coupling factor for the Σ3(111) TB, shown in Table 3, illustrate the application of the criterion of the least amount of shear for selecting the active coupling mode.

The disconnection mechanism of the TB movement is well established; however, alternative mechanisms are occasionally considered. The geometrical calculation allows us to describe the boundary migration-shear coupling for the analysed Σ3(111) TB. The findings of this research demonstrated that disconnection steps gliding along the TB are essential to elucidating the 'mixing' of solutions of the F-B equation. The above analysis indicates that such mixing is necessary to obtain accurate coupling factor values.

It is reasonable to suggest that the main difference between the approaches for describing boundary migration-shear coupling lies in the selection of the reference state. The classical disconnection approach typically assumes the bicrystal as its reference state. In this case, the Burgers vector content is associated only with disconnection, and the GB is free of dislocation content. Alternatively, when the F-B equation is applied to describe the dislocation content of the GB, the reference is assumed to be either the crystal lattice on one side of the boundary or an intermediate lattice. This selection leads to dislocation content existing throughout the boundary. Nevertheless, the resulting shear is consistent across approaches.

Table 3. Summary of coupling factor determination for Σ3(111) TB in Cu.

Burgers Vector content at steps		Weighting factor μ				Shear	
		D1		D2		D1	D2
D1	D2	μ_{D1}	$1-\mu_{D1}$	μ_{D2}	$1-\mu_{D2}$	s^{I}	s^{II}
$[00\bar{1}] + \frac{1}{2}[110]$	$[001] + \frac{1}{2}[110]$	$\frac{1}{2}$	$\frac{1}{2}$	$\frac{1}{2}$	$\frac{1}{2}$	**−0.707**	2.121

The coupling factor (produced shear) that agrees the with experiment is indicated in bold.

In previous paragraphs, the F-B and disconnection approaches were applied to a specific disconnection. It is worth noting that the proposed mechanism for mixing of F-B equation solutions by gliding the disconnection step along the boundary must demonstrate general applicability. One can suppose this general applicability because selecting different reference states does not affect the phenomenon of shear-coupled GB migration itself. This can be considered akin to a change of coordinate system.

It is known that multiple disconnections can exist for a given GB. For instance, one can have disconnections with different step heights, each giving rise to a different coupling factor. Consequently, an important question is whether the F-B analysis is capable of predicting these alternative coupling factors. Let us consider the disconnection with a step height twice higher than the disconnection observed in our simulations. Such a disconnection is theoretically possible, and its properties can be analysed. Hypothetical configuration of such disconnection is reproduced in Figure 3. The Burgers vector of disconnection derived from the dichromatic pattern in Figure 3 (a) is $\boldsymbol{b} = \frac{1}{6}[11\bar{2}]$, and the step height is equal to $H = 2\sqrt{3}a/3$, where a is the lattice parameter. The Burgers vector is opposite to the Burgers vector of a one-layer step. The shear s, which would be produced by migration of a two-layer disconnection with Burgers vector shown in Figure 3, is $s = \boldsymbol{b}/\boldsymbol{H} = \sqrt{\boldsymbol{2}}/\boldsymbol{4} = \boldsymbol{0.353}$. This value is half the size of the one observed experimentally. One might expect such a disconnection to be preferable due to lower shear. However, it is worth noting that according to Peierls–Nabarro theory mobility of dislocation is heavily dependent on the dislocation core width. In the case of disconnection, its core is usually localised within the step itself. A high step does not allow the core to spread much. Rather than the spreading of the core along the boundary, a localised nanofacet can form inside the core. This leads to the general trend that disconnections with

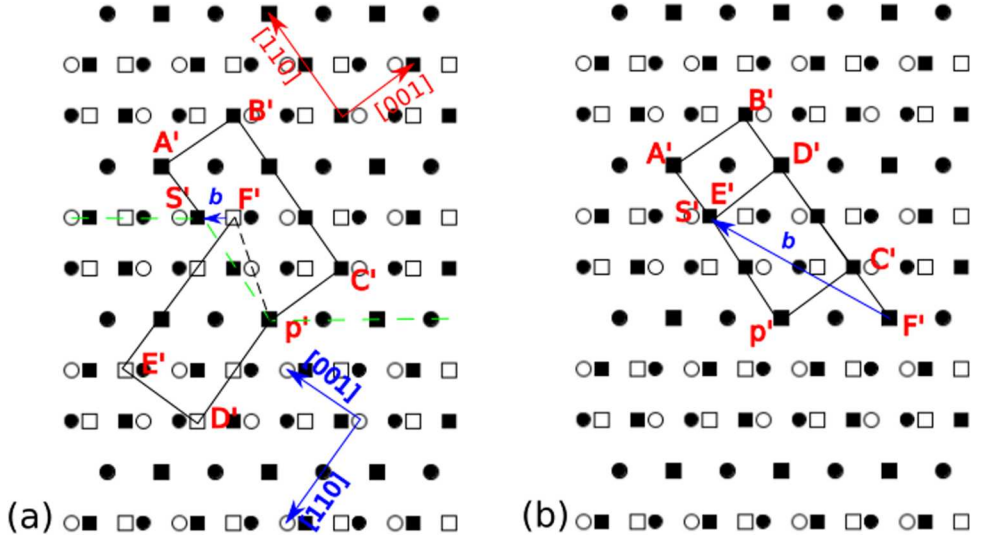

Figure 3. (a) Hypothetical disconnection with step height equal to two (111) interplanar distances reproduced in dichromatic pattern. The grain boundary with step is marked by dashed green line. Burgers vector $\boldsymbol{b}$ of disconnection is marked by blue arrow. In analogy with Figure 2(c) Burgers circuit ($\boldsymbol{S'A'B'C'pD'E'F'}$) can be drawn around disconnection step; (b) Burgers circuit ($\boldsymbol{S'A'B'C'pD'E'F'}$) reproduced in black (parent) crystal according to Description 1 misorientation.

higher steps are less mobile than those with lower steps. Consequently, disconnections with lower step are typically observed in simulations and experiment [24].

Figure 3(b) shows the Burgers circuit from Figure 3(a) reproduced in the parent crystal, assuming D1 misorientation. This circuit allows us to predict the Burgers vector content of the step as $[00\bar{1}] + \frac{3}{2}[100]$.

Taking into account that the projection length of the two-layer step into (111) plane is the same as the projection of the one-layer step, one can conclude that the proportion of dislocation content mixing in this case is 1:3, i.e. coefficient μ in Equation (4) is equal to 1/4. After substitution, one can get the following coupling factor:

$$s'_{\Sigma 3(111)} = \beta_{[00\bar{1}]+\frac{3}{2}[110]} = \frac{1}{4}\beta_{[00\bar{1}]} + \left(1 - \frac{1}{4}\right)\beta_{[110]} = 0.353 \tag{8}$$

This value is the same as that predicted by the disconnection approach, which supports the proposed reconciliation between the two approaches.

Summary and conclusions

The Σ3(111) TB in FCC copper was employed as a model system to compare and interrelate different theoretical approaches describing shear-coupled GB migration. By comparing models, it is shown that direct determination of the GB dislocation content via Burgers circuit construction around both flat and stepped segments enables a quantitative analysis of the coupling behaviour. The dislocation content of the flat boundary alone is insufficient to account for the experimentally observed shear. However, incorporating the dislocation content of the GB step allows for accurate predictions. This approach links the geometric shear coupling model, based on the analysis of solutions of the F-B equation, with the disconnection model. The step dislocation content can be formally interpreted as a mixing of dislocation contents from different representations of a flat boundary. Associating this mixing with step motion along the TB reveals the underlying physical mechanism and enables the prediction of the mixing proportions.

Disclosure statement

No potential conflict of interest was reported by the author(s).

Funding

This work has been supported by the project INTER-COST No. LUC24093 funded by the Ministry of Education, Youth and Sports of the Czech Republic.

ORCID

Ritu Verma http://orcid.org/0000-0003-1775-0724
Dmitri A. Molodov https://orcid.org/0000-0002-8094-9341
Andriy Ostapovets http://orcid.org/0000-0002-3781-4716

References

[1] A. Frøseth, H. Van Swygenhoven, and P.M. Derlet, *The influence of twins on the mechanical properties of nc-Al*. Acta Mater. 52 (2004), pp. 2259–2268. doi:10.1016/j.actamat.2004.01.017.

[2] A.G. Frøseth, P.M. Derlet, and H. Van Swygenhoven, *Grown-in twin boundaries affecting deformation mechanisms in nc-metals*. Appl. Phys. Lett. 85 (2004), pp. 5863–5865. doi:10.1063/1.1835531.

[3] D.E. Spearot, K.I. Jacob, and D.L. McDowell, *Nucleation of dislocations from [001] bicrystal interfaces in aluminum*. Acta Mater. 53 (2005), pp. 3579–3589. doi:10.1016/j.actamat.2005.04.012.

[4] D.E. Spearot, K.I. Jacob, and D.L. McDowell, *Dislocation nucleation from bicrystal interfaces with dissociated structure*. Int. J. Plast. 23 (2007), pp. 143–160. doi:10.1016/j.ijplas.2006.03.008.

[5] D.E. Spearot, M.A. Tschopp, K.I. Jacob, and D.L. McDowell, *Tensile strength of ⟨100⟩ and ⟨110⟩ tilt bicrystal copper interfaces*. Acta Mater. 55 (2007), pp. 705–714. doi:10.1016/j.actamat.2006.08.060.

[6] M.A. Tschopp and D.L. McDowell, *Dislocation nucleation in Σ3 asymmetric tilt grain boundaries*. Int. J. Plast. 24 (2008), pp. 191–217. doi:10.1016/j.ijplas.2007.02.010.

[7] F. Sansoz and J.F. Molinari, *Incidence of atom shuffling on the shear and decohesion behavior of a symmetric tilt grain boundary in copper*. Scr. Mater. 50 (2004), pp. 1283–1288. doi:10.1016/j.scriptamat.2004.02.031.

[8] F. Sansoz and J.F. Molinari, *Mechanical behavior of Σ tilt grain boundaries in nanoscale Cu and Al: A quasicontinuum study*. Acta Mater. 53 (2005), pp. 1931–1944. doi:10.1016/j.actamat.2005.01.007.

[9] E.W. Kelley and W. Hosford, *Plane-strain compression of magnesium and magnesium alloy crystals*. Trans Met Soc AIME 242 (1968), pp. 5–13.

[10] D. Caillard, F. Mompiou, and M. Legros, *Grain-boundary shear-migration coupling. II. Geometrical model for general boundaries*. Acta Mater. 57 (2009), pp. 2390–2402. doi:10.1016/j.actamat.2009.01.023.

[11] R.Z. Valiev, R.K. Islamgaliev, and V. Alexandrov I, *Bulk nanostructured materials from severe plastic deformation*. Prog. Mater. Sci. 45 (2000), pp. 103–189. doi:10.1016/S0079-6425(99)00007-9.

[12] J.W. Cahn, Y. Mishin, and A. Suzuki, *Coupling grain boundary motion to shear deformation*. Acta Mater. 54 (2006), pp. 4953–4975. doi:10.1016/j.actamat.2006.08.004.

[13] K.D. Molodov and D.A. Molodov, *Grain boundary mediated plasticity: On the evaluation of grain boundary migration - shear coupling*. Acta Mater. 153 (2018), pp. 336–353. doi:10.1016/j.actamat.2018.04.057.

[14] J.P. Hirth, *Dislocations, steps and disconnections at interfaces*. J. Phys. Chem. Solids 55 (1994), pp. 985–989. doi:10.1016/0022-3697(94)90118-X.

[15] J.W. Cahn, Y. Mishin, and A. Suzuki, *Duality of dislocation content of grain boundaries*. Philos. Mag. 86 (2006), pp. 3965–3980. doi:10.1080/14786430500536909.

[16] J.P. Hirth, R.C. Pond, R.G. Hoagland, X.-Y. Liu, and J. Wang, *Interface defects, reference spaces and the Frank–Bilby equation*. Prog. Mater. Sci. 58 (2013), pp. 749–823. doi:10.1016/j.pmatsci.2012.10.002.

[17] A. Suzuki and Y.M. Mishin, *Atomic mechanisms of grain boundary motion*. Mater. Sci. Forum 502 (2005), pp. 157–162. doi:10.4028/www.scientific.net/MSF.502.157.

[18] E.R. Homer, S.M. Foiles, E.A. Holm, and D.L. Olmsted, *Phenomenology of shear-coupled grain boundary motion in symmetric tilt and general grain boundaries*. Acta Mater. 61 (2013), pp. 1048–1060. doi:10.1016/j.actamat.2012.10.005.

[19] R. Hadian, B. Grabowski, and J. Neugebauer, *Gb code: A grain boundary generation code*. Journal of Open Source Software 3 (2018), pp. 900. doi:10.21105/joss.00900.

[20] A. Stukowski, *Visualization and analysis of atomistic simulation data with OVITO–the open visualization tool*. Modell. Simul. Mater. Sci. Eng. 18 (2010), pp. 015012. doi:10.1088/0965-0393/18/1/015012.

[21] S. Plimpton, *Fast parallel algorithms for short-range molecular dynamics*. J. Comput. Phys. 117 (1995), pp. 1–19. doi:10.1006/jcph.1995.1039.
[22] M.I. Mendelev, M.J. Kramer, C.A. Becker, and M. Asta, *Analysis of semi-empirical interatomic potentials appropriate for simulation of crystalline and liquid Al and Cu*. Philos. Mag. 88 (2008), pp. 1723–1750. doi:10.1080/14786430802206482.
[23] T.H. Blewitt, R.R. Coltman, and J.K. Redman, *Low-Temperature deformation of copper single crystals*. J. Appl. Phys. 28 (1957), pp. 651–660. doi:10.1063/1.1722824.
[24] Y.B. Wang, M.L. Sui, and E. Ma, *In situ observation of twin boundary migration in copper with nanoscale twins during tensile deformation*. Philos. Mag. Lett. 87(12) (2007), pp. 935–942. doi:10.1080/09500830701591493.

PHILOSOPHICAL MAGAZINE

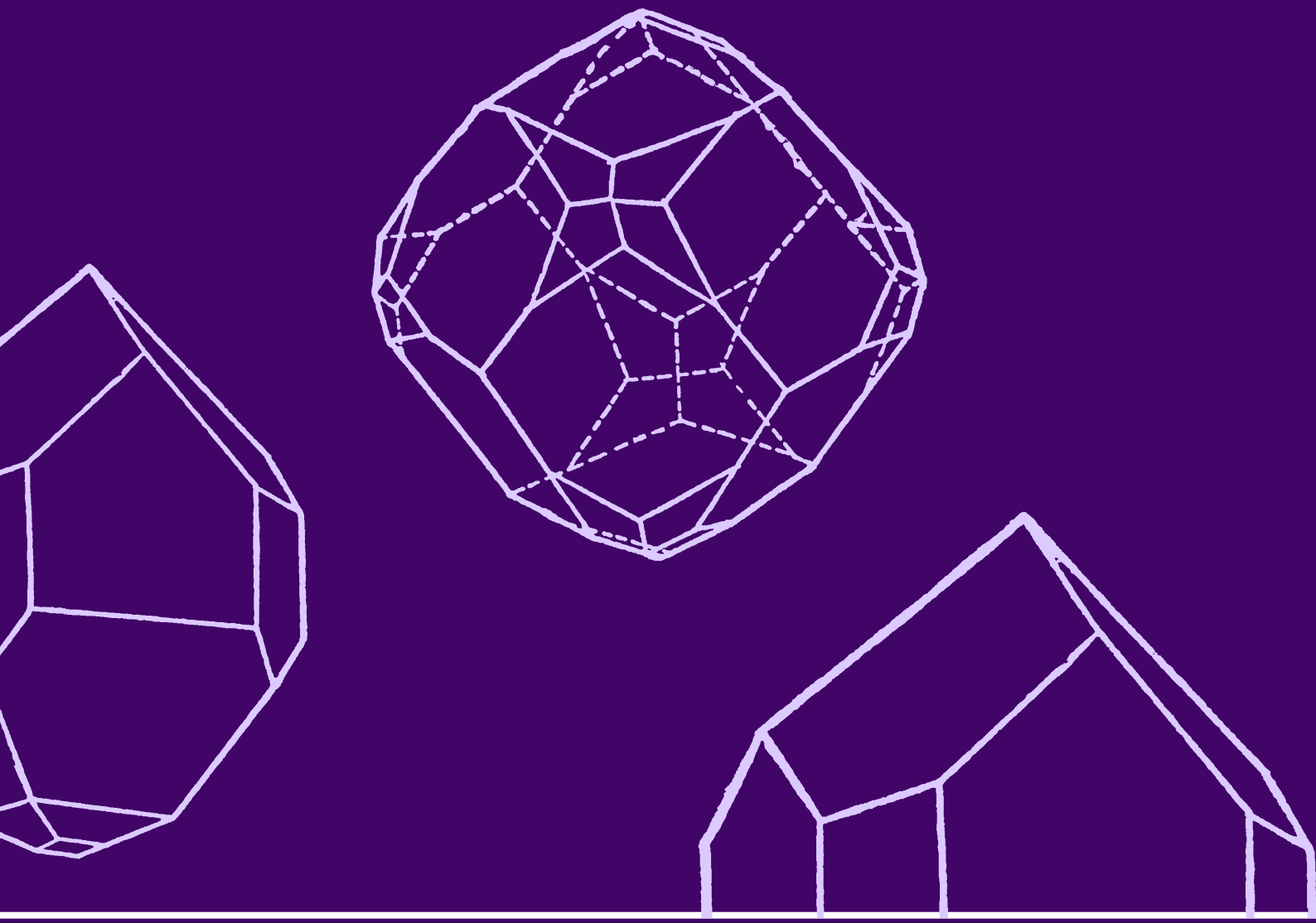

Contact us

Editorial Department | digitaleditor@philosophicalmagazine.com

Taylor & Francis
by informa